Fabrication of Micro/nano-structured Metals and Insulators and Its Applications to Devices Utilizing Optical Near-fields

金属ならびに絶縁体マイクロ･ナノ構造の作製
および近接場光利用デバイスへの応用

Submitted in partial fulfillment
of the requirements for the degree of
Doctor of Engineering

Ken-ichi NOMURA

野村 健一

Major in Electrical Engineering and Bioscience
Graduate School of Advanced Science and Engineering
Waseda University

早稲田大学大学院　先進理工学研究科
電気・情報生命専攻　誘電体材料研究

February 2010

Table of Contents

Chapter 1 Introduction ---------- 1
1.1 Objective ---------- 1
1.2 Near-field Optics ---------- 1
1.2.1 Evanescent Fields Induced by the Total Internal Reflection of Light ---------- 2
1.2.2 Surface Plasmon Resonance ---------- 3
1.2.3 Localized Surface Plasmon Resonance ---------- 8
1.2.4 Applications of Optical Near-fields ---------- 10
1.3 Fabrication of Micro- and Nano-structures ---------- 11
1.3.1 Swift-heavy-ion Beam Lithography ---------- 11
1.3.2 Chemical Synthesis in a Solution ---------- 13
References ---------- 14
Figures ---------- 18

Chapter 2 Structural Changes Induced in TiO_2 by Swift Heavy Ions and Its Applications to Three-dimensional Lithography ---------- 30
Abstract ---------- 30
2.1 Introduction ---------- 30
2.2 Experimental Procedures ---------- 31
2.3 Results ---------- 32
2.4 Discussion ---------- 34
2.5 Conclusions ---------- 36
References ---------- 37
Table ---------- 39
Figures ---------- 40

Chapter 3 Plasmonic Activity on Au Nanoparticles Embedded in Nanopores Formed in a Surface Layer of SiO_2 Glass by Swift-heavy-ion Irradiation ---------- 53
Abstract ---------- 53
3.1 Introduction ---------- 53
3.2 Experimental Procedures ---------- 54
3.2.1 Calculation of the Radius of the Melted Region ---------- 54
3.2.2 Materials ---------- 55
3.3 Results and Discussion ---------- 56
3.4 Conclusions ---------- 60

References---- 61
Figures ---- 63

Chapter 4 Fabrication of Inert Ag Nanoparticles with a Thin SiO_2 Coating ---- 72
Abstract---- 72
4.1 Introduction ---- 72
4.2 Experimental Procedures---- 73
4.3 Results and Discussion ---- 73
4.4 Conclusions ---- 75
References---- 76
Figures ---- 77

Chapter 5 Solution Conductivity as a Key Factor for Thin SiO_2 Coating on Colloidal Ag ------ 80
Abstract---- 80
5.1 Introduction ---- 80
5.2 Experimental Procedures---- 81
5.3 Results and Discussion ---- 81
5.4 Conclusions ---- 84
References---- 85
Figures ---- 86

Chapter 6 Shape-sensitive Reflectance by Nano-structured Metal Attached on an Optical Waveguide-mode Sensor ---- 90
Abstract---- 90
6.1 Introduction ---- 90
6.2 Experimental Procedures---- 90
6.3 Results and Discussion ---- 91
6.4 Conclusions ---- 95
References---- 96
Tables ---- 97
Figures ---- 99

Chapter 7 Summary ---- 105

Acknowledgments ---- 108

List of Papers Published by the Author ---------- 109

–Chapter 1– Introduction

1.1 Objective

As a future photonic technology, a new research field of “near-field optics” has attracted much attention. In the near-field optics, the light localized in a small region that is beyond the diffraction limit is utilized. This light is called “optical near-field” or “near-field light”. This special light is applicable to new optical devices with functions that could not be realized by conventional devices due to the diffraction limit [1–3]. Therefore, its basic and application-oriented researches are being carried out in many fields such as physics, chemistry, and biology. In order to generate the optical near-field, it is necessary to form micro- and nano-structured metals and insulators. Thus, it has been attempted to fabricate these structures using various methods. Furthermore, their optical properties have been investigated to discuss whether the structures can be applied to optical devices such as biomolecular sensors.

This doctoral thesis consists of seven chapters. In the following Section 1.2, the basic theory of the near-field optics will be explained, while that of the micro- or nano-structure formation and its related researches will be described in Section 1.3. From these reviews, advancement of the present developed methods will be revealed. In Chapter 2, structural changes induced by swift-heavy-ion irradiation in insulators will be discussed. Applications of swift-heavy-ion irradiation to three-dimensional lithography will also be described in Chapter 2. In Chapter 3, the research reported in Chapter 2 will be further developed. Namely, the effects induced by swift heavy ions in insulators will be investigated in more detail. Using knowledge obtained from the investigation, nanopores were formed on the surface of the insulator. Furthermore, a new plasmonic structure with a three-dimensional distribution of Au nanoparticles (NPs) was fabricated by embedment of Au NPs into the nanopores. It will be also discussed whether the fabricated structure can be applied to optical devices such as biomolecular sensors. In addition, thin-silica-coated Ag NPs, which are applicable to various optical devices, were fabricated by chemical syntheses, and their optical properties and applicability to devices will be discussed in Chapter 4. In Chapter 5, which is closely related to Chapter 4, effects of a solution conductivity on the formation of the thin-silica-coated Ag NPs will be examined in detail. In Chapter 6, a nondestructive technique that utilizes optical near-fields induced by the total internal reflection of light to estimate, in principle, the shapes of metal nanostructures will be demonstrated. Finally, in Chapter 7, the researches will be summarized, and future prospects in the near-field optics will be addressed.

1.2 Near-field Optics

In this section, the basic theories dealing with various phenomena in near-field optics and their applications are described. First, evanescent fields induced by the total internal reflection of light are

explained in Section 1.2.1. Then, in Section 1.2.2, the principle of the surface plasmon resonance induced in metal films, which is essential to discuss the near-field optics, is mentioned, while that of the localized surface plasmon resonance induced in metal NPs is explained in Section 1.2.3. Lastly, applications of these phenomena are summarized in Section 1.2.4.

1.2.1 Evanescent Fields Induced by the Total Internal Reflection of Light

First, localized light called "evanescent field", which is induced by the total internal reflection of light, is described [4]. As shown in Fig. 1.1, at $z = 0$, material A with a relative permittivity of ε_a' ($z > 0$) is assumed to be on material B with that of ε_b' ($z < 0$). Here, it is assumed to be $\varepsilon_a' < \varepsilon_b'$, while the dielectric loss factors of both materials are assumed to be zero in order to simplify discussion. In this configuration, light with an angular frequency of ω is illuminated from the side of material B at an incident angle of θ_b, and is assumed to be refracted at an angle of θ_a. Here, the incident plane of the light is assumed to be the zx plane. In this case, the electric field of the light propagating in material A, referred to as $\boldsymbol{E}_a$, is expressed as

$$\boldsymbol{E}_a = \boldsymbol{E}_{a0} \exp\{i(k_{ax}x + k_{az}z - \omega t)\}, \tag{1.1}$$

where k_{ax} and k_{az} are the wave numbers of the light in the x and z directions, respectively, and are written as

$$k_{ax} = \frac{\omega}{c}\sqrt{\varepsilon_a'}\sin\theta_a, \tag{1.2}$$

$$k_{az} = \frac{\omega}{c}\sqrt{\varepsilon_a'}\cos\theta_a. \tag{1.3}$$

Furthermore, from Snell's law, the following Eq. (1.4) can be estimated,

$$\sin\theta_a = \sqrt{\frac{\varepsilon_b'}{\varepsilon_a'}}\sin\theta_b. \tag{1.4}$$

If the light is illuminated at an incident angle θ_b, which is larger than the total internal reflection angle obtained by substituting $\theta_a = \pi/2$ into Eq. (1.4), the light is completely reflected at the interface between materials A and B. In this case, Eq. (1.4) can be transformed into

$$\cos\theta_a = \pm i\sqrt{-1 + \frac{\varepsilon_b'}{\varepsilon_a'}\sin^2\theta_b}. \tag{1.5}$$

Thus, in the case that the illuminated light is internally reflected totally, Eq. (1.1) can be written as Eq. (1.6) using Eqs. (1.2), (1.3), and (1.5),

$$\boldsymbol{E}_a = \boldsymbol{E}_{a0} \exp\left\{i\left(\frac{\omega}{c}\sqrt{\varepsilon_a'}\sin\theta_a x - \omega t\right) \mp \frac{\omega}{c}\sqrt{-\varepsilon_a' + \varepsilon_b'\sin^2\theta_b}\, z\right\}. \tag{1.6}$$

If we take the plus sign in Eq. (1.6), the electric field increases exponentially as the distance from the interface becomes large, which never actually happens. Therefore, Eq. (1.6) is expressed as

$$\boldsymbol{E}_a = \boldsymbol{E}_{a0} \exp\left\{ i\left(\frac{\omega}{c}\sqrt{\varepsilon_a'}\sin\theta_a x - \omega t\right) - \frac{\omega}{c}\sqrt{-\varepsilon_a' + \varepsilon_b' \sin^2\theta_b}\, z \right\}. \tag{1.7}$$

From Eq. (1.7), it is found that the electric field intensity decays exponentially with an increase in distance from the interface, which indicates that the light is localized in the vicinity of the interface. This is a feature of an evanescent wave induced by the total internal reflection of light, which is applicable to a waveguide-mode sensor to detect substances such as biomolecules.

In Chapter 6, a nondestructive technique that utilizes optical near-fields induced by the total internal reflection of light to estimate, in principle, the shapes of metal nanostructures will be demonstrated.

1.2.2 Surface Plasmon Resonance

When light with a wavelength longer than a certain critical one is illuminated to metals such as Au and Ag, it is completely reflected by the plasma oscillation. This phenomenon is called "plasma reflection", while the critical wavelength λ_p called "plasma wavelength" is expressed using the equation [1,5–9],

$$\lambda_p = 2\pi c\sqrt{\frac{\varepsilon_0 m}{ne^2}}, \tag{1.8}$$

where c, ε_0, m, n, and e are the speed of light, vacuum permittivity, static electron mass, density of electrons in a metal, and elementary charge. Since λ_p is calculated to be ~140 nm in Au and Ag [1], visible light, with wavelengths longer than λ_p, is completely reflected, showing metallic luster.

However, in the case that P-polarized light with the electric field parallel to its incident plane is illuminated to metals at a certain incident angle, its reflectance may significantly decrease. This phenomenon is called "surface plasmon (SP) resonance", and its principle can be explained as follows [1–3,10,11]. As shown in Fig. 1.2(a), a structure composed of three layers of materials C, D, and E is assumed. Here, at $z = 0$, materials C ($z > 0$) and D ($z < 0$) are in contact with each other, while the relative complex permittivities of materials C, D, and E are given as $\varepsilon_{rc}^{*} = \varepsilon_{rc}' - i\varepsilon_{rc}''$, $\varepsilon_{rd}^{*} = \varepsilon_{rd}' - i\varepsilon_{rd}''$, and $\varepsilon_{re}^{*} = \varepsilon_{re}' - i\varepsilon_{re}''$, respectively. In this configuration, P-polarized light with an angular frequency ω is assumed to be propagating in materials C and D, keeping its electric field parallel to the zx plane. The electric field of the light in material C or at $z > 0$, referred to as $\boldsymbol{E}_c$, is described using the equation,

$$\boldsymbol{E}_c = (E_{cx}\boldsymbol{i} + E_{cz}\boldsymbol{k}) \exp\left\{ i\left(k_{cx}x + k_{cz}z - \omega t\right)\right\}, \tag{1.9}$$

while the one in material D or at $z < 0$, referred to as $\boldsymbol{E}_d$, is expressed as

$$\boldsymbol{E}_d = (E_{dx}\boldsymbol{i} + E_{dz}\boldsymbol{k}) \exp\left\{ i\left(k_{dx}x - k_{dz}z - \omega t\right)\right\}. \tag{1.10}$$

Here, it is assumed that materials C and D are electrically neutral on a macroscopic scale, and have no net true electric charges. Furthermore, it is also assumed that the frequency of the propagating light is too high for conduction current to flow. Moreover, permeabilities of most materials are considered to be completely unity. From these assumptions, the wave equation,

$$\nabla^2 \boldsymbol{E} = \frac{\varepsilon_r^*}{c^2} \frac{\partial^2 \boldsymbol{E}}{\partial t^2}, \tag{1.11}$$

is derived from Maxwell's equations [12]. By substituting Eqs. (1.9) and (1.10) into Eq. (1.11), the following Eqs. (1.12) and (1.13) can be obtained, respectively,

$$-{k_{cx}}^2 - {k_{cz}}^2 = -\frac{\varepsilon_{rc}^*}{c^2}\omega^2, \tag{1.12}$$

$$-{k_{dx}}^2 - {k_{dz}}^2 = -\frac{\varepsilon_{rd}^*}{c^2}\omega^2. \tag{1.13}$$

Furthermore, from Gauss's law,

$$\nabla \cdot (\varepsilon_0 \varepsilon_{rc}^* \boldsymbol{E}_c) = 0, \tag{1.14}$$

$$\nabla \cdot (\varepsilon_0 \varepsilon_{rd}^* \boldsymbol{E}_d) = 0, \tag{1.15}$$

are obtained. By substituting Eqs. (1.9) and (1.10) into Eqs. (1.14) and (1.15), the following Eqs. (1.16) and (1.17) can be obtained, respectively,

$$E_{cx} k_{cx} = -E_{cz} k_{cz}, \tag{1.16}$$

$$E_{dx} k_{dx} = E_{dz} k_{dz}. \tag{1.17}$$

In addition, from Gauss's law, the dielectric flux density in the *z* direction should be the same on both sides of the interface between materials A and B. Therefore, the following Eq. (1.18) can be obtained,

$$\varepsilon_{rc}^* E_{cz} = \varepsilon_{rd}^* E_{dz}. \tag{1.18}$$

Furthermore, from the fact that the electric field in the *x* direction is the same on each side to fulfill the relation, rot$\boldsymbol{E}$ = 0, the following Eq. (1.19) can be estimated,

$$E_{cx} = E_{dx}. \tag{1.19}$$

Moreover, the equation,

$$k_{cx} = k_{dx}, \tag{1.20}$$

can be obtained since the wave number in the *x* direction is also the same on each side. From Eqs.

(1.16) to (1.20), the following Eq. (1.21) can be derived,

$$k_{cz} = -\frac{\varepsilon_{rc}^{*}}{\varepsilon_{rd}^{*}} k_{dz} . \tag{1.21}$$

Furthermore, from Eqs. (1.12), (1.13), (1.20), and (1.21), k_{cx} and k_{dx} can be calculated as

$$k_{cx} = k_{dx} = \pm \frac{\omega}{c} \sqrt{\frac{\varepsilon_{rc}^{*} \varepsilon_{rd}^{*}}{\varepsilon_{rc}^{*} + \varepsilon_{rd}^{*}}} . \tag{1.22}$$

Here, since it is assumed that the light is propagating in the $+x$ direction, Eq. (1.22) can be written as

$$k_{cx} = k_{dx} = \frac{\omega}{c} \sqrt{\frac{\varepsilon_{rc}^{*} \varepsilon_{rd}^{*}}{\varepsilon_{rc}^{*} + \varepsilon_{rd}^{*}}} . \tag{1.23}$$

By substituting Eq. (1.23) into Eq. (1.12), k_{cz} can be calculated as

$$k_{cz} = \pm \frac{\omega}{c} \frac{\varepsilon_{rc}^{*}}{\sqrt{\varepsilon_{rc}^{*} + \varepsilon_{rd}^{*}}}, \tag{1.24}$$

while k_{dz} can be expressed from Eqs. (1.21) and (1.24) as,

$$k_{dz} = \mp \frac{\omega}{c} \frac{\varepsilon_{rd}^{*}}{\sqrt{\varepsilon_{rc}^{*} + \varepsilon_{rd}^{*}}} . \tag{1.25}$$

Here, it is assumed that material C is a transparent dielectric material with no optical loss. Thus, its relative permittivity and relative dielectric loss factor can be assumed as $\varepsilon_{rc}' > 1$ and $\varepsilon_{rc}'' = 0$, respectively, while material D is assumed to be a metal with $\varepsilon_{rd}' < 0$ and $\varepsilon_{rd}'' \neq 0$. However, in order to utilize the effect of SP excitation to optical devices, the dielectric loss factor of the metal should be as small as possible in order to minimize the optical loss. From this viewpoint, noble metals such as Au and Ag with significantly low dielectric loss factors are often used to excite SP. Thus, for further calculations, $\varepsilon_{rd}'' = 0$ is assumed to simplify discussion. Note that the SP occurring in this case is called “Fano mode” [2]. Using these assumptions, Eqs. (1.23) to (1.25) can be transformed into the following Eqs. (1.26) to (1.28), respectively,

$$k_{cx} = k_{dx} = \frac{\omega}{c} \sqrt{\frac{\varepsilon_{rc}' \varepsilon_{rd}'}{\varepsilon_{rc}' + \varepsilon_{rd}'}}, \tag{1.26}$$

$$k_{cz} = \pm \frac{\omega}{c} \frac{\varepsilon_{rc}'}{\sqrt{\varepsilon_{rc}' + \varepsilon_{rd}'}}, \tag{1.27}$$

$$k_{dz} = \mp \frac{\omega}{c} \frac{\varepsilon_{rd}'}{\sqrt{\varepsilon_{rc}' + \varepsilon_{rd}'}}. \tag{1.28}$$

Here, if $\varepsilon_{rc}' + \varepsilon_{rd}' < 0$, k_{cx} and k_{dx} are real, while k_{cz} and k_{dz} are imaginary. In this case, using Eqs. (1.26) to (1.28), Eqs. (1.9) and (1.10) can be transformed into the following Eqs. (1.29) and (1.30), respectively,

$$\boldsymbol{E}_c = (E_{cx}\boldsymbol{i} + E_{cz}\boldsymbol{k}) \exp\left\{ i\left(\frac{\omega}{c} \sqrt{\frac{\varepsilon_{rc}'\varepsilon_{rd}'}{\varepsilon_{rc}' + \varepsilon_{rd}'}} x - \omega t \right) \mp \frac{\omega}{c} \frac{\varepsilon_{rc}'}{\sqrt{-(\varepsilon_{rc}' + \varepsilon_{rd}')}} z \right\}, \tag{1.29}$$

$$\boldsymbol{E}_d = (E_{dx}\boldsymbol{i} + E_{dz}\boldsymbol{k}) \exp\left\{ i\left(\frac{\omega}{c} \sqrt{\frac{\varepsilon_{rc}'\varepsilon_{rd}'}{\varepsilon_{rc}' + \varepsilon_{rd}'}} x - \omega t \right) \mp \frac{\omega}{c} \frac{\varepsilon_{rd}'}{\sqrt{-(\varepsilon_{rc}' + \varepsilon_{rd}')}} z \right\}. \tag{1.30}$$

Here, $\varepsilon_{rc}' > 0$ in dielectric material C where $z > 0$ and $\varepsilon_{rd}' < 0$ in metal D where $z < 0$. Therefore, if we take the plus signs in Eqs. (1.29) and (1.30), the electric field increases exponentially with an increase in distance from the interface in both materials C and D. This never happens. Thus, Eqs. (1.29) and (1.30) can be expressed as the following Eqs. (1.31) and (1.32), respectively,

$$\boldsymbol{E}_c = (E_{cx}\boldsymbol{i} + E_{cz}\boldsymbol{k}) \exp\left\{ i\left(\frac{\omega}{c} \sqrt{\frac{\varepsilon_{rc}'\varepsilon_{rd}'}{\varepsilon_{rc}' + \varepsilon_{rd}'}} x - \omega t \right) - \frac{\omega}{c} \frac{\varepsilon_{rc}'}{\sqrt{-(\varepsilon_{rc}' + \varepsilon_{rd}')}} z \right\}, \tag{1.31}$$

$$\boldsymbol{E}_d = (E_{dx}\boldsymbol{i} + E_{dz}\boldsymbol{k}) \exp\left\{ i\left(\frac{\omega}{c} \sqrt{\frac{\varepsilon_{rc}'\varepsilon_{rd}'}{\varepsilon_{rc}' + \varepsilon_{rd}'}} x - \omega t \right) - \frac{\omega}{c} \frac{\varepsilon_{rd}'}{\sqrt{-(\varepsilon_{rc}' + \varepsilon_{rd}')}} z \right\}. \tag{1.32}$$

Here, as a typical example, the angular frequency of light ω is assumed to be 3×10^{15} (1/s), which corresponds to that of He-Ne laser light, while materials C and D are assumed to be SiO_2 glass ($\varepsilon_{rc}' = 1.5$) and Au ($\varepsilon_{rd}' = -10$), respectively. In this case, $\left| \frac{\omega}{c} \frac{\varepsilon_{rc}'}{\sqrt{-(\varepsilon_{rc}' + \varepsilon_{rd}')}} \right|$ and $\left| \frac{\omega}{c} \frac{\varepsilon_{rd}'}{\sqrt{-(\varepsilon_{rc}' + \varepsilon_{rd}')}} \right|$ are calculated to be ~5.1 (1/μm) and ~34 (1/μm), respectively, which indicates that, on Eqs. (1.31) and (1.32), the light is localized in the z direction in the vicinity of the interface between the dielectric material C and metal D, while it propagates in the x direction. This is a typical feature of SP.

Next, as shown in Fig. 1.2(b), it is assumed that P-polarized light incident on metal D at an incident angle θ from the material E is totally reflected at the interface. Here, material E is assumed to be a dielectric material with $\varepsilon_{re}' > 1$ and $\varepsilon_{re}'' = 0$. In this case, as mentioned in Section 1.2.1, an evanescent wave propagates in the x direction in metal D, while its electric field decays with an increase in distance from the interface between metal D and dielectric material E [4]. The wave

number of this evanescent wave in the x direction, referred to as k_{Ex}, is described using the equation,

$$k_{Ex} = \frac{\omega}{c}\sqrt{\varepsilon_{re}'}\sin\theta . \tag{1.33}$$

If metal D is so thin that the evanescent wave can reach the interface between dielectric material C and metal D and if $k_{Ex} = k_{cx}$ is satisfied, SP is excited at this interface. Thus, from Eqs. (1.26) and (1.33), θ at $k_{Ex} = k_{cx}$, referred to as θ_{sp}, can be expressed by the following Eq. (1.34),

$$\theta_{sp} = \sin^{-1}\left(\sqrt{\frac{\varepsilon_{rc}'}{\varepsilon_{re}'}}\sqrt{\frac{\varepsilon_{rd}'}{\varepsilon_{rc}'+\varepsilon_{rd}'}}\right), \tag{1.34}$$

which represents the incident angle of light coming to the interface between metal D and dielectric material E, at which the SP is excited. Here, as mentioned in relation to Eqs. (1.31) and (1.32), $\varepsilon_{rc}' + \varepsilon_{rd}' < 0$, $\varepsilon_{rc}' > 0$, and $\varepsilon_{rd}' < 0$. Therefore,

$$\sqrt{\frac{\varepsilon_{rd}'}{\varepsilon_{rc}'+\varepsilon_{rd}'}} > 1 . \tag{1.35}$$

Namely, θ_{sp} in Eq. (1.34) can be real, only when ε_{re}' is large enough to satisfy the relation,

$$\sqrt{\frac{\varepsilon_{re}'}{\varepsilon_{rc}'}} > \sqrt{\frac{\varepsilon_{rd}'}{\varepsilon_{rc}'+\varepsilon_{rd}'}} > 1 . \tag{1.36}$$

Thus, substances with high permittivities are frequently employed as material E.

From the above-mentioned discussion, conditions to excite SP are summarized as follows: (i) $\varepsilon_{rc}' + \varepsilon_{rd}' < 0$. (ii) Metal D is thin enough for the evanescent wave induced by the total internal reflection of light at the interface between metal D and dielectric material E to reach the interface. (iii) ε_{re}' is large enough to satisfy the inequality (1.36).

Here, if the angular frequency or wavelength of the incident light as well as the permittivities of metal D and dielectric material E is known, ε_{rc}' is a sole variable in Eq. (1.34). This in turn indicates that ε_{rc}' can be estimated if we measure the incident angle θ_{sp} of light in a system made of known substances D and E. If a certain dielectric material C is attached on the surface of metal D, the incident angle θ_{sp} will be changed. Therefore, by measuring θ_{sp}, the permittivity ε_{rc}' is known. This can be used to detect the attachment of substance C.

Figure 1.3 shows optical reflection spectra of the substrate composed of an SF-10 glass substrate used as dielectric material E, a 45-nm-thick Au film used as metal D, and a 1-nm-thick Cr film used as an adhesive layer between the SF-10 glass and Au [13]. The spectra were obtained before and after block copolymer consisting of poly(ethylene glycol) and poly(propylene sulphide) used as dielectric material C was attached on the surface of the Au film [13]. It is clearly shown that the dip induced by the SP excitation shifts toward a higher incident angle by the attachment of copolymer to

the Au film surface.

1.2.3 Localized Surface Plasmon Resonance

In addition to film-shaped metals described in Section 1.2.2, SP can be excited in NP-like metals. The SP resonance induced in metal NPs is called "localized surface plasmon (LSP) resonance", in distinction from the SP resonance that occurs in a metal film [1–3]. Its principle can be explained as follows. As shown in Fig. 1.4(a), a spherical metal NP, referred to as F, with a radius r is assumed to be present in a dielectric material called G [12]. Here, the relative complex permittivity of metal NP is expressed as $\varepsilon_{rf}^{*} = \varepsilon_{rf}' - i\varepsilon_{rf}''$, while the relative permittivity and relative dielectric loss factor of dielectric material G are given as ε_{rg}' and zero, respectively. An external electric field $\boldsymbol{E}_0$ would be applied uniformly if light with a wavelength much longer than the diameter of metal NP F is illuminated to this system. In this case, free electrons in the metal NP are moved by the electric field $\boldsymbol{E}_0$ to induce a uniform dielectric polarization vector $\boldsymbol{P}$ as shown in Fig. 1.4(a). The electric field outside the metal NP is calculable by assuming a dipole moment $\boldsymbol{M}$,

$$\boldsymbol{M} = \frac{4\pi r^3}{3}\boldsymbol{P}, \tag{1.37}$$

instead of the metal NP F at the original center position of F surrounded by a medium with the relative permittivity of ε_{rg}', as shown in Fig. 1.4(b), and by adding $\boldsymbol{E}_0$ and the electric field induced by $\boldsymbol{M}$.

If we take the origin of coordinates at the center of NP F, the electric field induced by the dipole moment $\boldsymbol{M}$ in the r and θ directions at the point (r,θ), referred to as E_{gr} and $E_{g\theta}$ respectively, can be written as

$$E_{gr} = \frac{M\cos\theta}{2\pi\varepsilon_0\varepsilon_{rg}' r^3}, \tag{1.38}$$

$$E_{g\theta} = \frac{M\sin\theta}{4\pi\varepsilon_0\varepsilon_{rg}' r^3}. \tag{1.39}$$

Thus, the dielectric flux density in a direction normal to the NP surface and the electric field in a direction tangential to the NP surface, referred to as D_{gn} and E_{gt} respectively, can be calculated as

$$D_{gn} = \varepsilon_0\varepsilon_{rg}' E_0\cos\theta + \frac{M\cos\theta}{2\pi r^3}, \tag{1.40}$$

$$E_{gt} = -E_0\sin\theta + \frac{M\sin\theta}{4\pi\varepsilon_0\varepsilon_{rg}' r^3}. \tag{1.41}$$

On the other hand, the electric field $\boldsymbol{E}_i$ in metal NP F becomes uniform as shown in Fig. 1.4(c). Therefore, at the point (r,θ) in the NP, the dielectric flux density in a direction normal to the surface and the electric field in a direction tangential to the surface can be expressed as

$$D_{fn} = \varepsilon_0 \varepsilon_{rf}^{*} E_i \cos\theta \,, \tag{1.42}$$

$$E_{ft} = -E_i \sin\theta \,. \tag{1.43}$$

Moreover, using relations $D_{fn} = D_{gn}$ and $E_{ft} = E_{gt}$, which are derived from div$\boldsymbol{D}$ = 0 and rot$\boldsymbol{E}$ = 0 respectively, the following equation

$$\boldsymbol{E}_i = \frac{3\varepsilon_{rg}'}{\varepsilon_{rf}^{*} + 2\varepsilon_{rg}'} \boldsymbol{E}_0 \,, \tag{1.44}$$

is obtained. Since the dielectric polarization $\boldsymbol{P}$ is expressible as

$$\boldsymbol{P} = \varepsilon_0 (\varepsilon_{rf}^{*} - 1) \boldsymbol{E}_i \,, \tag{1.45}$$

the following Eq. (1.46) can be obtained by substituting Eq. (1.44) into Eq. (1.45),

$$\boldsymbol{P} = \frac{3\varepsilon_0 \varepsilon_{rg}' (\varepsilon_{rf}^{*} - 1)}{\varepsilon_{rf}^{*} + 2\varepsilon_{rg}'} \boldsymbol{E}_0 \,. \tag{1.46}$$

Here, assuming that the dielectric loss factor of metal NP F is zero, namely, $\varepsilon_{rf}^{*} = \varepsilon_{rf}'$, similarly to the assumption in Section 1.2.2, Eq. (1.46) is transformed into

$$\boldsymbol{P} = \frac{3\varepsilon_0 \varepsilon_{rg}' (\varepsilon_{rf}' - 1)}{\varepsilon_{rf}' + 2\varepsilon_{rg}'} \boldsymbol{E}_0 \,, \tag{1.47}$$

which indicates that the dielectric polarization $\boldsymbol{P}$ diverges if $\varepsilon_{rf}' = -2\varepsilon_{rg}'$, and this is a necessary condition to excite LSP. In this case, the incident light is localized in metal NPs and in their vicinities and does not propagate in space, since the electric field is enhanced due to the dielectric polarization of NPs [2,3,14].

In addition, an LSP excitation wavelength can be estimated from the above equations. The relative permittivity ε_{rf}' of metal NP F illuminated by light with a wavelength λ can be calculated as

$$\varepsilon_{rf}' = \varepsilon^{\infty} - \frac{\lambda^2}{\lambda_p^{\,2}} \,, \tag{1.48}$$

from the kinetic equation of a free electron in a metal on the condition that the damping effect is negligible [5]. In Eq. (1.48), ε^{∞} and λ_p are the high frequency permittivity of metal NP F and plasma wavelength given in Section 1.2.2, respectively. Since $\varepsilon_{rf}' = -2\varepsilon_{rg}'$ as mentioned above when LSP is excited, the LSP excitation wavelength λ_L can be obtained from Eq. (1.48) as [8,9]

$$\lambda_L = \lambda_p \sqrt{\varepsilon^{\infty} + 2\varepsilon_{rg}'} \,, \tag{1.49}$$

which indicates that λ_L depends on ε_{rg}'.

In order to estimate LSP excitation wavelengths for Au NPs surrounded by various liquids, Okamoto and co-workers measured light absorption of a cell with monolayered Au nanoparticles on the sidewall, as shown in Fig. 1.5(a), and obtained the spectra shown in Fig. 1.5(b) [15]. The peak wavelength, which corresponds to the LSP excitation wavelength, shifts clearly toward a longer wavelength with an increase in refractive index or permittivity of the surrounding liquid. Namely, using metal NPs, the permittivity change induced by the attachment of a substance to the surfaces of metal NPs can be detected, which is applicable to detecting devices such as biomolecular sensors. Note that the absorbance peak height increases with an increase in refractive index around the Au NPs as shown in Fig. 1.5(b). This is due to the fact that the extinction cross section becomes larger as the refractive index increases [8,9].

1.2.4 Applications of Optical Near-fields

The near-field optical phenomena explained in Sections 1.2.1 to 1.2.3 can be applied to various devices. In this section, several examples are described.

· Sensors

As mentioned in Sections 1.2.2 and 1.2.3, the change in permittivity of a substance on metal NPs can be detected using the SP resonance and LSP resonance. This is applicable to sensors to detect the presence of substances such as biomolecules [16–21] and gases [22,23]. In recent years, aiming at more highly sensitive sensing, sensors utilizing the electric field simultaneously enhanced by the LSP excitation as well as by the SP excitation have been proposed [24], while sensors utilizing SP [25] or LSP [26] excited by the light with electric field that was enhanced while propagating in an optical waveguide, have also been reported. In relation to the above, fabrication of a new plasmonic structure with a three-dimensional distribution of Au NPs embedded into nanopores formed on SiO_2 glass and its applicability will be described in Chapter 3. Furthermore, a waveguide-mode sensor has been attracted much attention recently, since its sensitivity is a few times or several ten times as high as that of a usual SP resonance sensor [27–31]. In this regard, a waveguide-mode sensor can be in principle used for shape estimation of metal nanostructures. This application will be shown in Chapter 6.

· High-performance Photocatalysts, Solar Cells, Lasers, and Light-emitting Diodes

When SP or LSP is excited, the electric field intensity is enhanced by a factor of several tens compared to that of the incident light in the vicinities of metal surfaces [2]. There have been several papers reporting that high-performance optical devices can be realized using the electric field enhancement. Awazu and co-workers have reported that the photocatalytic activity of anatase TiO_2

films [32] can be enhanced by a factor of five, by utilizing the electric field enhanced in the TiO_2 films by the LSP excitation induced around Ag NPs embedded in the TiO_2 [33]. Similarly, improvement in photoelectric conversion efficiency has also been reported for polymer solar cells by the use of the electric field enhancement around Ag NPs [34]. Furthermore, the electric field enhancement can also increase the output of a vertical-cavity surface-emitting laser [35] and a light-emitting diode [36]. In regard to the above, fabrication of Ag NPs coated with thin-protective SiO_2 glass films, aiming at applications to photocatalysts, will be described in Chapters 4 and 5.

· Other Applications

Optical near-fields are, as a matter of course, applicable to various other devices. For example, Raman scattering can be enhanced if the electric field is enhanced by LSP, which is called "surface-enhanced Raman scattering" [37–42]. Optical near-fields can also be applied to a microscope to observe a substance with a size smaller than the one limited by the diffraction [43,44]. Namely, in a microscope called scanning near-field optical microscope, optical near-field is localized in a small region by illuminating light to a small aperture with a diameter of several ten nm formed in metal or to a sharp metal needle with a curvature of several ten nm. When the optical near-field is very close to a target substance, it is scattered depending on the surface shape of the substance. Thus, by measuring scattering properties, an extremely small region can be observed.

Moreover, utilization of optical near-fields has been rapidly expanding to many other applications or devices such as a plasmonic waveguide in which SP propagates along Ag NPs aligned one-dimensionally and periodically [45], lithography utilizing optical near-fields induced by LSP excitation [46], and estimation of particle diameters utilizing the shape-dependent strong scattering of optical near-fields by the particles upon the total internal reflection [47].

1.3 Fabrication of Micro- and Nano-structures

To realize devices utilizing optical near-fields, it is necessary to form micro- and nano-structured metals and insulators so that the SP or LSP resonance or the evanescent wave resulting from the total internal reflection of light may be induced. In this section, advanced methods employed in the present research to fabricate these structures are described.

1.3.1 Swift-heavy-ion Beam Lithography

To fabricate materials in the order of μm or nm, a combination of lithography and reactive ion etching (RIE) is often used due to ease of handling [48–51]. In this method, first, aperture patterns are formed in a photoresist film on a certain material by lithography. Then, the material is etched by being exposed to a corrosive gas through a patterned photoresist mask. As a result, desirable concavo-convex shapes can be transcribed on the surface of the material.

However, since corrosive gases are used for the etching, it is inevitable that sidewalls of fabricated trenches become bumpy. Figure 1.6 shows a scanning electron microscopy (SEM) image of a soda-lime glass surface etched by the above-mentioned procedure [48], while Fig. 1.7 shows an SEM image obtained after a TiO_2 film on a Si substrate was etched by a similar one [49]. The etched surfaces shown in these figures are not smooth. Furthermore, solid state residues are generated during RIE of certain materials. For example, RIE cannot be used to fabricate Er-doped optical waveguides for optical amplification [52], since reactions between fluorine-containing gases and Er yield ErF_3, which is solid at room temperature [53].

In order to overcome these problems, a novel fabrication method called "latent-track etching" has been proposed [54–58]. If heavy ions with a high acceleration energy in the order of MeV are implanted on materials, cylindrical damages, called "latent tracks", with diameters of a few nm and depths of a few μm are generated; one for each ion. For example, the etching rate of latent tracks in SiO_2 glass by immersion in hydrofluoric acid is around five times as high as that of nonirradiated regions [54]. Namely, micro- and nano-structures can be fabricated by utilizing the difference in etching rate between latent tracks and nonirradiated regions.

Figure 1.8 shows a surface SEM image of SiO_2 glass observed after the irradiation of 33-MeV Se ions and subsequent etching of latent tracks [54], while Fig. 1.9 shows a cross sectional SEM image of polyimide obtained after immersion in an aqueous solution of sodium hypochlorite following the irradiation of 13-MeV/u Au ions [55]. Figures 1.8 and 1.9 show that sidewall surfaces formed by the latent track etching are smooth, compared to those obtained by RIE shown in Figs. 1.6 and 1.7. Furthermore, it seems that no residues remain on the surfaces, probably because the residues generated should have been flown away into a solution.

As the latent-track formation mechanism, two models have been proposed. The thermal spike model [59] assumes that the temperature at the ion-irradiated region increases above the melting point instantly due to interactions between phonons and hot electrons resulting from energetic ions [60], and then it goes down quickly to room temperature. Figure 1.10 shows the lattice temperature of quartz hit by a 3.4-MeV/u Kr ion, which was derived by this model, as a function of the time elapsed from the ion collision [61]. Note that spectra (a), (b), (c), and (d) correspond lattice temperatures at points 1.0, 3.0, 4.5, and 8.0 nm away from the ion path, respectively, and that T_m represents the melting point of quartz. Spectra (a) and (b) indicate that the lattice temperature immediately reaches the melting point within 4×10^{-14} s, while it falls to room temperature in only $\sim 3 \times 10^{-10}$ s. Namely, the thermal spike model assumes that latent tracks are formed since the structural change induced by the temperature increase above the melting point remains after the subsequent rapid quench. On the other hand, the ionic spike model assumes that structural changes occur due to the Coulombic repulsion between positive charges induced by the irradiated ions [62]. Note that the thermal spike model is more widely accepted recently, since calculated results agree

well with experimental ones [61,63–67].

In regard to the above, the threshold to form latent tracks on a rutile TiO_2 single crystal by swift-heavy-ion irradiation will be discussed in Chapter 2 using theoretical calculations of energy deposited to electrons. Two-dimensional patters of holes on the surface of TiO_2 microscopically fabricated by irradiation of 120-MeV Br ions and subsequent etching of latent tracks in a hydrofluoric acid solution will be also demonstrated in Chapter 2. As a further development of the contents in Chapter 2, sizes of the latent tracks formed in SiO_2 glass by swift-heavy-ion irradiation will be discussed in Chapter 3 using a lattice-temperature simulation based on the thermal spike model. Moreover, nanopore formation by etching of latent tracks through exposure to hydrofluoric acid vapor will be demonstrated in Chapter 3 in order to show that this method is useful for nanofabrication of high-aspect-ratio nanopores in insulators.

1.3.2 Chemical Synthesis in a Solution

Metal NPs have been attracting much attention recently, since light can be localized in a small region beyond the diffraction limit by the LSP resonance mentioned in Section 1.2.3. One method to fabricate metal NPs is physical fabrication such as a combination of the lithography and RIE mentioned in Section 1.3.1. However, it is quite difficult to form small NPs with diameters around 10 nm by such a physical method. Thus, reduction of metal ions in a solution is frequently employed to solve this problem [68–72]. The NPs with diameters below 10 nm can be obtained easily by this method, although they cannot be aligned at a desirable position. As a typical example, Fig. 1.11 is a transmission electron microscopy (TEM) image of quite small Au NPs with an average diameter of 5.5 nm, fabricated by the reduction of Au ions [68]. Thus, a chemical synthesis is attractive since it can break the fabrication limit of a physical method.

When NPs are coated with a film using a physical method, the film thickness tends to be inhomogeneous since deposition occurs only one-dimensionally [33]. On the other hand, a film with a homogenous thickness can be obtained by chemical synthesis in a solution. Therefore, it is suitable for coating of a film around NPs [7,73–81]. Figure 1.12 shows a TEM image of Au NPs coated with block copolymer consisting of polystyrene and acrylic acid by chemical synthesis in a solution [73]. It is clearly shown that films with a homogenous thickness are coated around the Au NPs.

In relation to the above, fabrication of Ag NPs using reduction of metal ions in a solution and coating of a protective SiO_2-glass film around the NPs will be mentioned in Chapter 4. Further, influences of solution conductivity upon aggregation of the SiO_2-glass coated Ag NPs will be analyzed and the condition to realize no aggregation will be discussed based on the analysis in Chapter 5.

References for Chapter 1

[1] *Near-Field Optics and Surface Plasmon Polaritons*, edited by S. Kawata (Springer, Berlin, 2001).

[2] *Hikari Nanotekunoroji No Kiso (Basics of Optical Nanotechnology)*, edited by M. Fukui and M. Ohtsu (Ohmsha, Tokyo, 2003) [in Japanese].

[3] *Recent Advances on Design and Applications of Plasmonic Nanomaterials*, edited by S. Yamada (CMC Publishing, Tokyo, 2006) [in Japanese].

[4] *Evanescent Waves: From Newtonian Optics to Atomic Optics*, edited by F. de Fornel (Springer, Berlin, 2001).

[5] *Introduction to Solid State Physics*, 3rd ed., edited by C. Kittel (John Wiley and Sons, New York, 1967).

[6] *Yudentai Bussei (Dielectric Properties)*, edited by Y. Ohki (Baifukan, Tokyo, 2002) [in Japanese].

[7] T. Hirakawa and P. V. Kamat, J. Am. Chem. Soc. **127**, 3928 (2005).

[8] A. C. Templeton, J. J. Pietron, R. W. Murray, and P. Mulvaney, J. Phys. Chem. B **104**, 564 (2000).

[9] P. Mulvaney, Langmuir **12**, 788 (1996).

[10] J. Homola, S. S. Yee, and G. Gauglitz, Sens. Actuators A **54**, 3 (1999).

[11] K. Welford, Opt. Quantum Electron. **23**, 1 (1991).

[12] *Denjikigaku (Electromagnetism)*, edited by Y. Ohki (Ohmsha, Tokyo, 2007) [in Japanese].

[13] J. P. Bearinger, S. Terrettaz, R. Michel, N. Tirelli, H. Vogel, M. Textor, and J. A. Hubbell, Nat. Mater. **2**, 259 (2003).

[14] *Metal Nanoparticles: Synthesis, Characterization, and Applications*, edited by D. L. Feldheim and C. A. Foss, Jr. (Marcel Dekker, New York, 2002).

[15] T. Okamoto, I. Yamaguchi, and T. Kobayashi, Opt. Lett. **25**, 372 (2000).

[16] N. Fukuda, Y. Kasuya, and H. Ushijima, e-J. Surf. Sci. Nanotech. **7**, 571 (2009).

[17] X. D. Hoa, A. G. Kirk, and M. Tabrizian, Biosens. Bioelectron. **23**, 151 (2007).

[18] S. C. B. Gopinath, D. Balasundaresan, J. Akitomi, and H. Mizuno, J. Biochem. **140**, 667 (2006).

[19] A. J. Haes, W. P. Hall, L. Chang, W. L. Klein, and R. P. Van Duyne, Nano Lett. **4**, 1029 (2004).

[20] N. Nath and A. Chilkoti, J. Fluoresc. **14**, 377 (2004).

[21] J. Homola, Anal. Bioanal. Chem. **377**, 528 (2003).

[22] A. Abdelghani, J. M. Chovelon, N. Jaffrezic-Renault, C. Ronot-Trioli, C. Veillas, and H. Gagnaire, Sens. Actuators B **38-39**, 407 (1997).

[23] B. Liedberg, C. Nylander, and I. Lundstrom, Sens. Actuators **4**, 299 (1983).

[24] L. He, M. D. Musick, S. R. Nicewarner, F. G. Salinas, S. J. Benkovic, M. J. Natan, and C. D. Keating, J. Am. Chem. Soc. **122**, 9071 (2000).

[25] J. Dostálek, J. Čtyroký, J. Homola, E. Brynda, M. Skalský, P. Nekvindová, J. Špirková, J. Škvor, and J. Schröfel, Sens. Actuators B **76**, 8 (2001).

[26] K. Mitsui, Y. Handa, and K. Kajikawa, Appl. Phys. Lett. **85**, 4231 (2004).

[27] M. Fujimaki, C. Rockstuhl, X. Wang, K. Awazu, J. Tominaga, Y. Koganezawa, Y. Ohki, and T. Komatsubara, Opt. Express **16**, 6408 (2008).

[28] M. Fujimaki, C. Rockstuhl, X. Wang, K. Awazu, J. Tominaga, N. Fukuda, Y. Koganezawa, and Y. Ohki, Nanotechnology **19**, 095503 (2008).

[29] K. Awazu, C. Rockstuhl, M. Fujimaki, N. Fukuda, J. Tominaga, T. Komatsubara, T. Ikeda, and Y. Ohki, Opt. Express **15**, 2592 (2007).

[30] G. Rong, A. Najmaie, J. E. Sipe, and S. M. Weiss, Biosens. Bioelectron. **23**, 1572 (2008).

[31] W. Knoll, Annu. Rev. Phys. Chem. **49**, 569 (1998).

[32] A. Fujishima and K. Honda, Nature **238**, 37 (1972).

[33] K. Awazu, M. Fujimaki, C. Rockstuhl, J. Tominaga, H. Murakami, Y. Ohki, N. Yoshida, and T. Watanabe, J. Am. Chem. Soc. **130**, 1676 (2008).

[34] A. J. Morfa, K. L. Rowlen, T. H. Reilly III, M. J. Romero, and J. van de Lagemaat, Appl. Phys. Lett. **92**, 013504 (2008).

[35] T. Onishi, T. Tanigawa, T. Ueda, and D. Ueda, IEEE J. Quantum Electron. **43**, 1123 (2007).

[36] S. Pillai, K. R. Catchpole, T. Trupke, G. Zhang, J. Zhao, and M. A. Green, Appl. Phys. Lett. **88**, 161102 (2006).

[37] T. Itoh, K. Hashimoto, A. Ikehata, and Y. Ozaki, Appl. Phys. Lett. **83**, 5557 (2003).

[38] C. Wang, C. Liu, Y. Liu, and Z. Zhang, Appl. Surf. Sci. **147**, 52 (1999).

[39] Y. Iwanabe, M. Fujimaki, K. Awazu, T. Horiuchi, and J. Tominaga, Nanotechnology **17**, 1717 (2006).

[40] M. Fujimaki, K. Awazu, J. Tominaga, and Y. Iwanabe, J. Appl. Phys. **100**, 074303 (2006).

[41] J. T. Krug II, G. D. Wang, S. R. Emory, and S. Nie, J. Am. Chem. Soc. **121**, 9208 (1999).

[42] S. J. Henley, J. D. Carey, and S. R. P. Silva, Appl. Phys. Lett. **88**, 081904 (2006).

[43] T. Saiki and K. Matsuda, Appl. Phys. Lett. **74**, 2773 (1999).

[44] M. Specht, J. D. Pedarnig, W. M. Heckl, and T. W. Hänsch, Phys. Rev. Lett. **68**, 476 (1992).

[45] S. A. Maier, P. G. Kik, H. A. Atwater, S. Meltzer, E. Harel, B. E. Koel, and A. A. G. Requicha, Nat. Mater. **2**, 229 (2003).

[46] X. Luo and T. Ishihara, Appl. Phys. Lett. **84**, 4780 (2004).

[47] X. Yu, Y. Araki, K. Iwami, and N. Umeda, Opt. Lett. **33**, 2794 (2008).

[48] J. Vieillard, R. Mazurczyk, L. L. Boum, A. Bouchard, Y. Chevolot, P. Cremillieu, B. Hannes,

and S. Krawczyk, Microelectron. Eng. **85**, 465 (2008).

[49] S. Norasetthekul, P. Y. Park, K. H. Baik, K. P. Lee, J. H. Shin, B. S. Jeong, V. Shishodia, E. S. Lambers, D. P. Norton, and S. J. Pearton, Appl. Surf. Sci. **185**, 27 (2001).

[50] C. F. Wang, R. Hanson, D. D. Awschalom, E. L. Hu, T. Feygelson, J. Yang, and J. E. Butler, Appl. Phys. Lett. **91**, 201112 (2007).

[51] A. Behnam, Y. Choi, L. Noriega, Z. Wu, I. Kravchenko, A. G. Rinzler, and A. Ural, J. Vac. Sci. Technol. B **25**, 348 (2007).

[52] *Optical Fiber Communications: Principles and Practice*, 2nd ed., edited by J. M. Senior (Prentice Hall, Hertfordshire, UK, 1992).

[53] http://www.phelly.com/Evaporation/E1.html

[54] K. Awazu, S. Ishii, K. Shima, S. Roorda, and J. L. Brebner, Phys. Rev. B **62**, 3689 (2000).

[55] C. Trautmann, W. Brüchle, R. Spohr, J. Vetter, and N. Angert, Nucl. Instrum. Methods Phys. Res. B **111**, 70 (1996).

[56] P. Apel, A. Schulz, R. Spohr, C. Trautmann, and V. Vutsadakis, Nucl. Instrum. Methods Phys. Res. B **146**, 468 (1998).

[57] R. G. Musket, J. M. Yoshiyama, R. J. Contolini, and J. D. Porter, J. Appl. Phys. **91**, 5760 (2002).

[58] D. Dobrev, J. Vetter, R. Neumann, and N. Angert, J. Vac. Sci. Technol. B **19**, 1385 (2001).

[59] G. Bonfiglioli, A. Ferro, and A. Monjoni, J. Appl. Phys. **32**, 2499 (1961).

[60] M. P. R. Waligorski, R. N. Hamm, and R. Kats, Nucl. Tracks Radiat. Meas. **11**, 309 (1986).

[61] Z. G. Wang, Ch. Dufour, E. Paumier, and M. Toulemoude, J. Phys.: Condens. Matter **6**, 6733 (1994).

[62] R. L. Fleischer, MRS Bull. **20**, 17 (1995).

[63] M. Toulemonde, J. M. Costantini, Ch. Dufour, A. Meftah, E. Paumier, and F. Studer, Nucl. Instrum. Methods Phys. Res. B **116**, 37 (1996).

[64] A. Meftah, F. Brisard, J. M. Costantini, E. Dooryhee, M. Hage-Ali, M. Hervieu, J. P. Stoquert, F. Studer, and M. Toulemonde, Phys. Rev. B **49**, 12457 (1994).

[65] T. van Dillen, A. Polman, W. Fukarek, and A. van Blaaderen, Appl. Phys. Lett. **78**, 910 (2001).

[66] G. Szenes, K. Havancsák, V. Skuratov, P. Hanák, L. Zsoldos, and T. Ungár, Nucl. Instrum. Methods Phys. Res. B **166-167**, 933 (2000).

[67] H. Trinkaus and A. I. Ryazanov, Phys. Rev. Lett. **74**, 5072 (1995).

[68] N. R. Jana, L. Gearheart, and C. J. Murphy, Langmuir **17**, 6782 (2001).

[69] N. R. Jana, L. Gearheart, and C. J. Murphy, Chem. Mater. **13**, 2313 (2001).

[70] S. Link and M. A. El-Sayed, J. Phys. Chem. B **103**, 4212 (1999).

[71] S. Panigrahi, S. Kundu, S. K. Ghosh, S. Nath, and T. Pal, J. Nanopart. Res. **6**, 411 (2004).

[72] K. S. Chou and C. Y. Ren, Mater. Chem. Phys. **64**, 241 (2000).

[73] Y. Kang and T. A. Taton, Angew. Chem. Int. Ed. **44**, 409 (2005).

[74] Y. Kobayashi, H. Katakami, E. Mine, D. Nagao, M. Konno, and L. M. Liz-Marzán, J. Colloid Interface Sci. **283**, 392 (2005).

[75] V. Salgueiriño-Maceira, F. Caruso, and L. M. Liz-Marzán, J. Phys. Chem. B **107**, 10990 (2003).

[76] T. Ung, L. M. Liz-Marzán, and P. Mulvaney, Colloids Surf. A: Physicochem. Eng. Aspects **202**, 119 (2002).

[77] T. Ung, L. M. Liz-Marzán, and P. Mulvaney, Langmuir **14**, 3740 (1998).

[78] L. M. Liz-Marzán, M. Giersig, and P. Mulvaney, Langmuir **12**, 4329 (1996).

[79] S. Liu and M. Han, Adv. Funct. Mater. **15**, 961 (2005).

[80] S. Liu, Z. Zhang, and M. Han, Anal. Chem. **77**, 2595 (2005).

[81] C. Graf, D. L. J. Vossen, A. Imhof, and A. van Blaaderen, Langmuir **19**, 6693 (2003).

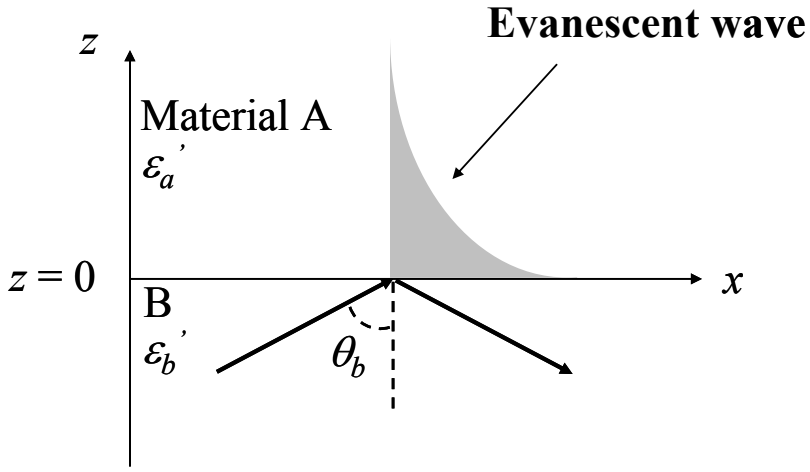

Fig. 1.1. Schematic drawing showing an evanescent wave induced by the total internal reflection of light incident on material A with the incident angle θ_b from material B.

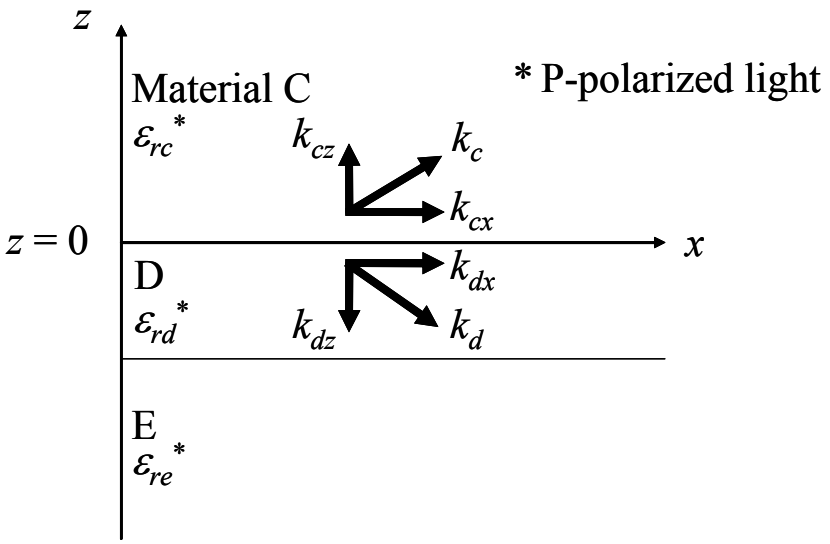

(a)

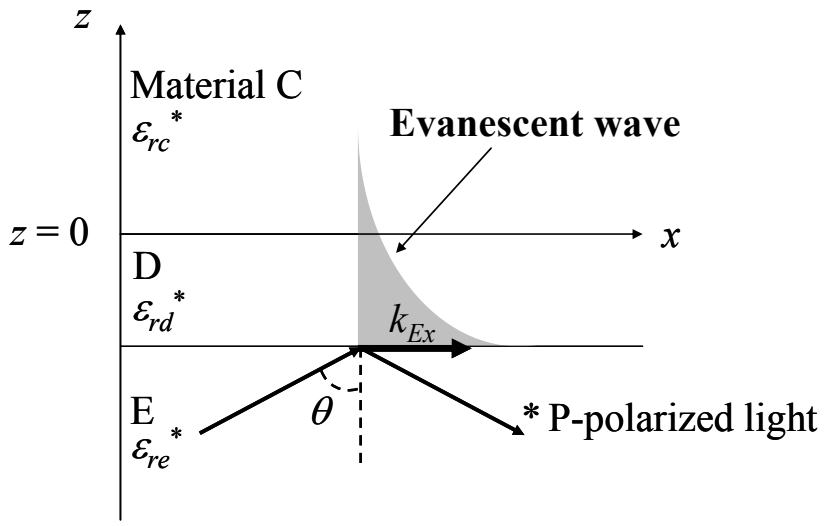

(b)

Fig. 1.2. Schematic drawing of three layers, composed of materials C, D, and E, to estimate the condition of SP excitation. (a) Wavevectors of P-polarized light propagating in materials C and D. (b) An evanescent wave induced by the total internal reflection of P-polarized light incident on metal D from material E.

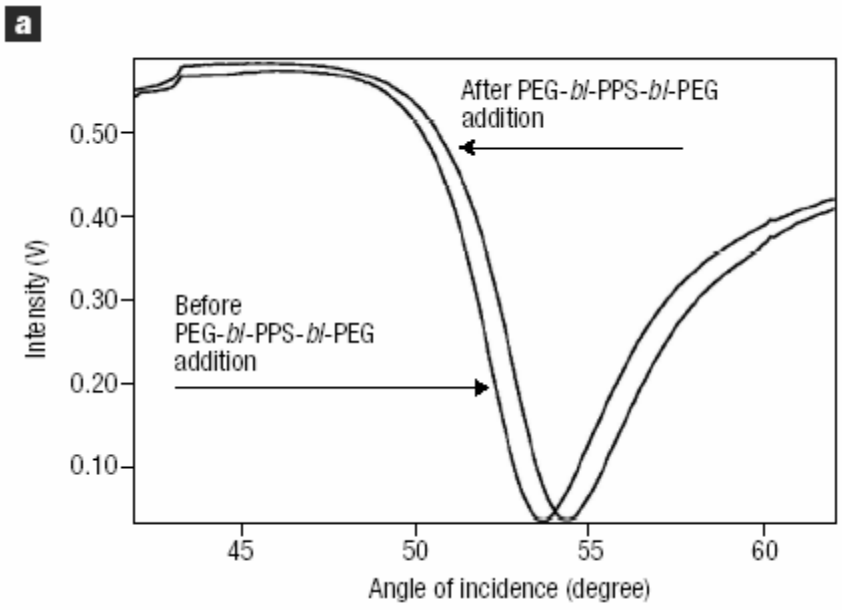

Fig. 1.3. Comparison of the optical reflection spectra of a 45-nm-thick Au film on an SF-10 glass substrate with a 1-nm-thick Cr adhesive layer, before and after block copolymer consisting of poly(ethylene glycol) and poly(propylene sulphide) was attached on the surface of the Au film. (After Ref. 13)

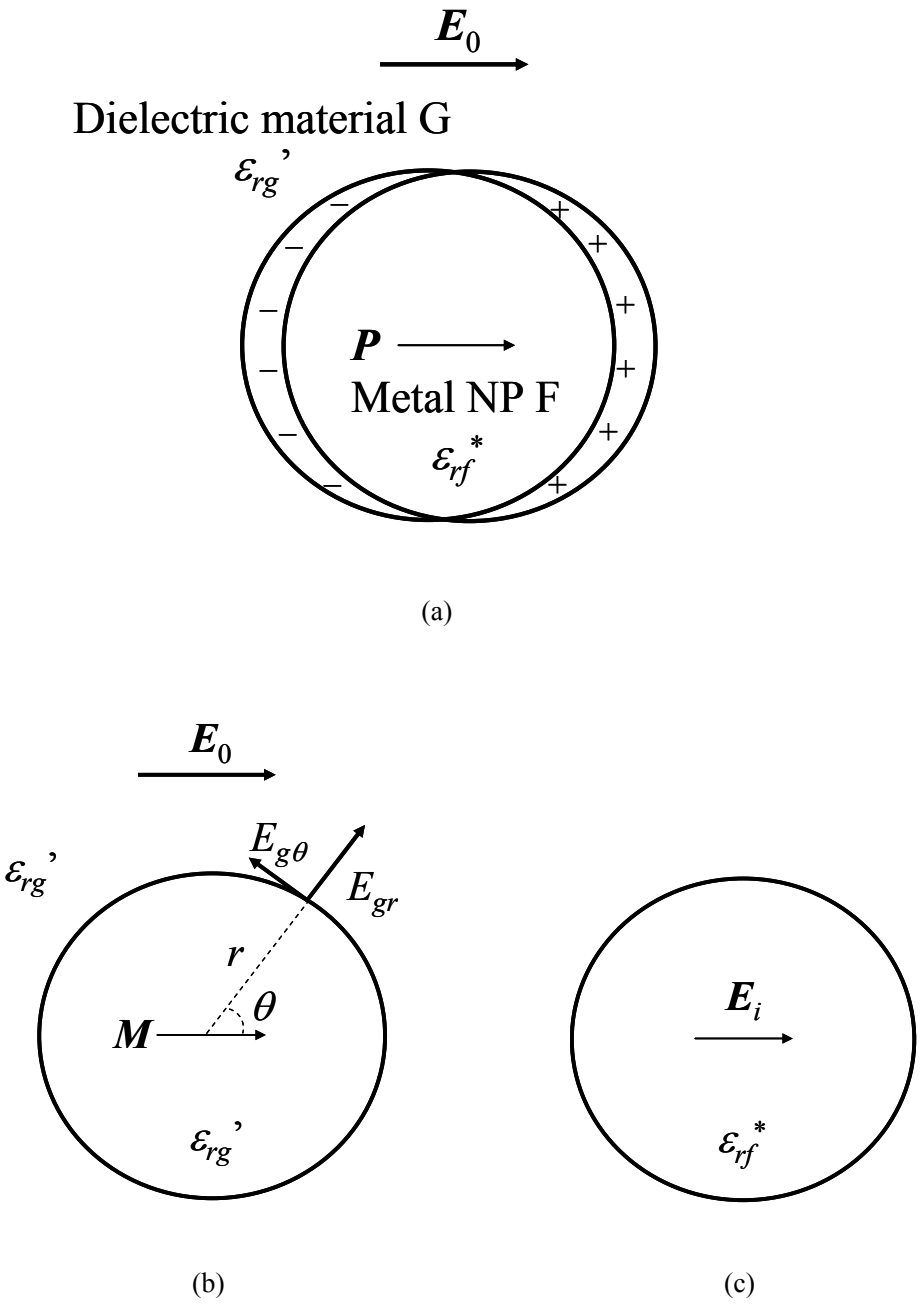

Fig. 1.4. Schematic drawing showing a spherical metal NP called F in a dielectric G. (a) Polarization $\boldsymbol{P}$ induced in F by an external electric field $\boldsymbol{E}_0$. (b) Dipole moment $\boldsymbol{M}$ equivalent to $\boldsymbol{P}$ and its electric field components E_{gr} and $E_{g\theta}$ to estimate the electric field outside the metal F. (c) Electric field $\boldsymbol{E}_i$ inside the metal F.

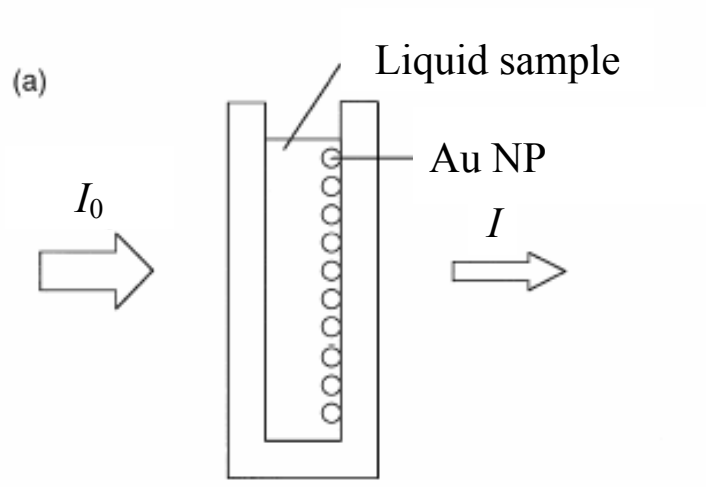

(a)

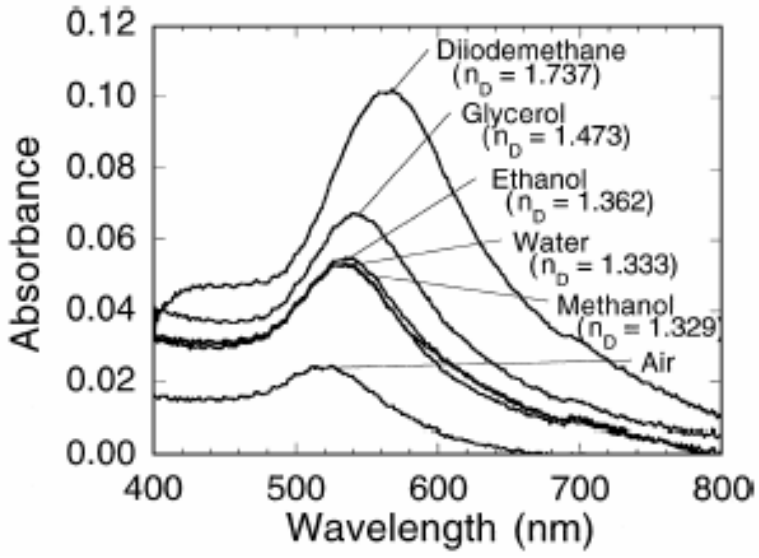

(b)

Fig. 1.5. (a) Schematic drawing of Au NPs in liquid in a cell to estimate LSP excitation wavelengths. (b) Examples of spectra obtained using the system shown in (a). (After Ref. 15)

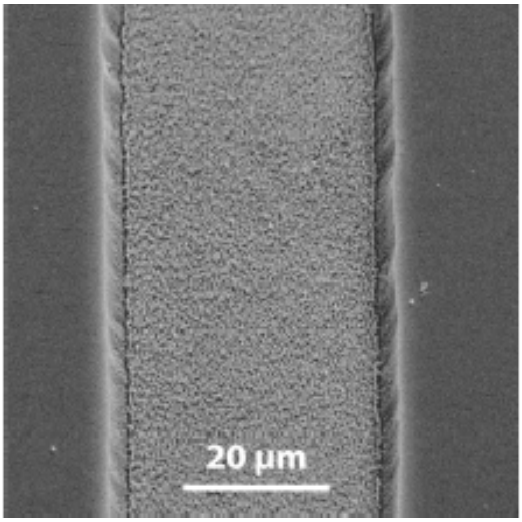

Fig. 1.6. A surface SEM image of a soda-lime glass etched by the combination of lithography and RIE. (After Ref. 48)

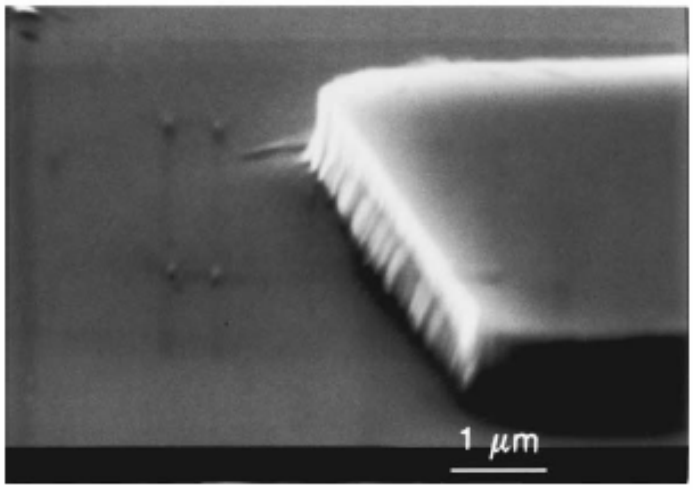

Fig. 1.7. An SEM image of a TiO_2 film on a Si substrate etched by the combination of lithography and RIE. (After Ref. 49)

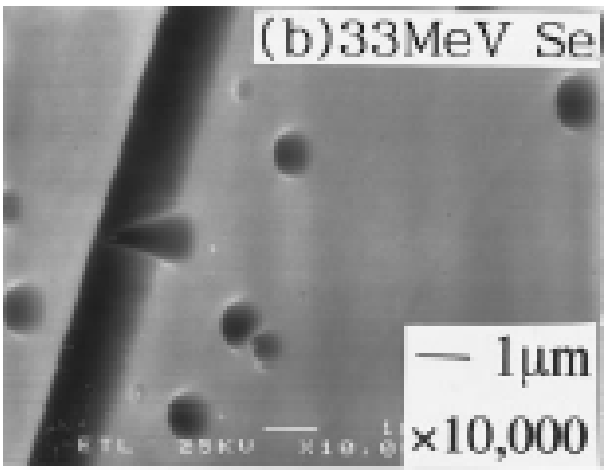

Fig. 1.8. An SEM image of SiO_2 glass obtained after the irradiation of 33-MeV Se ions and subsequent etching of latent tracks by 48% hydrofluoric acid. (After Ref. 54)

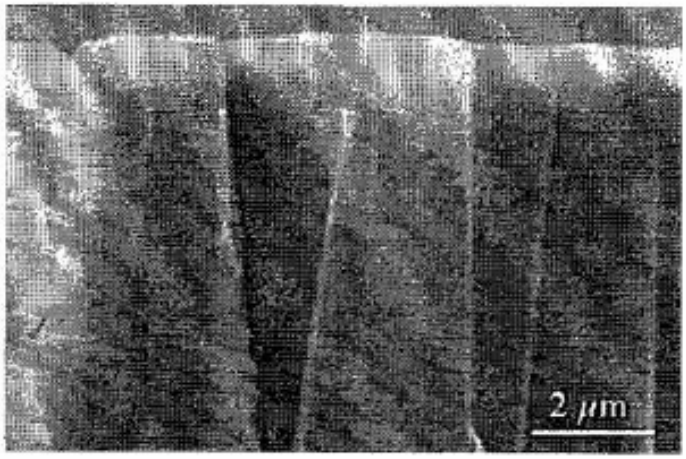

Fig. 1.9. A cross sectional SEM image of polyimide obtained after the irradiation of 13-MeV/u Au ions and subsequent etching of latent tracks through immersion in an aqueous solution of sodium hypochlorite. Note that “u” in “MeV/u” means “atomic mass unit”. (After Ref. 55)

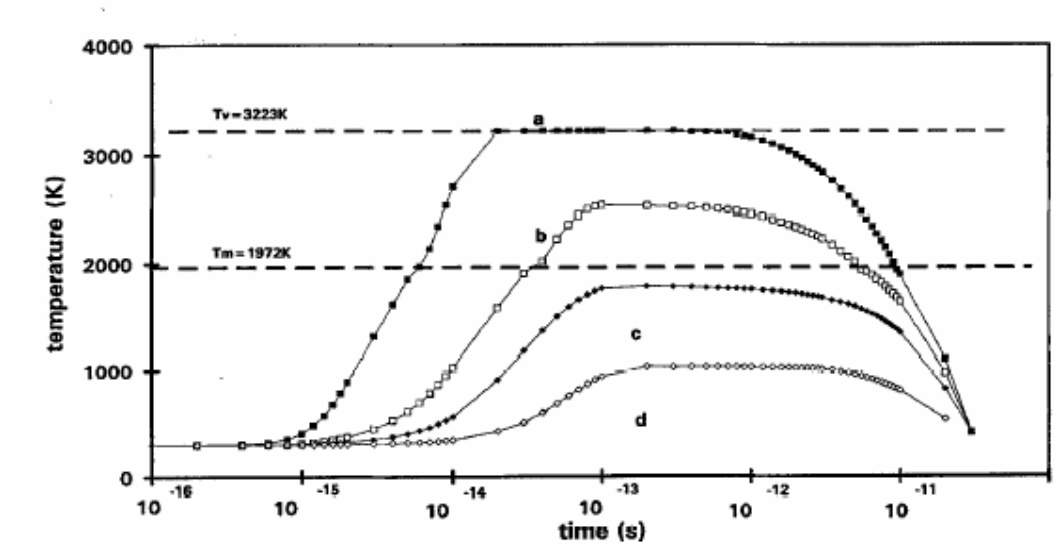

Fig. 1.10. Lattice temperature of quartz hit by a 3.4-MeV/u Kr ion, derived based on the thermal spike model as a function of the time elapsed from the ion collision. Spectra (a), (b), (c), and (d) correspond lattice temperatures at points 1.0, 3.0, 4.5, and 8.0 nm away from the ion path, respectively. T_m and T_v represent the melting point and boiling point of quartz, respectively. (After Ref. 61)

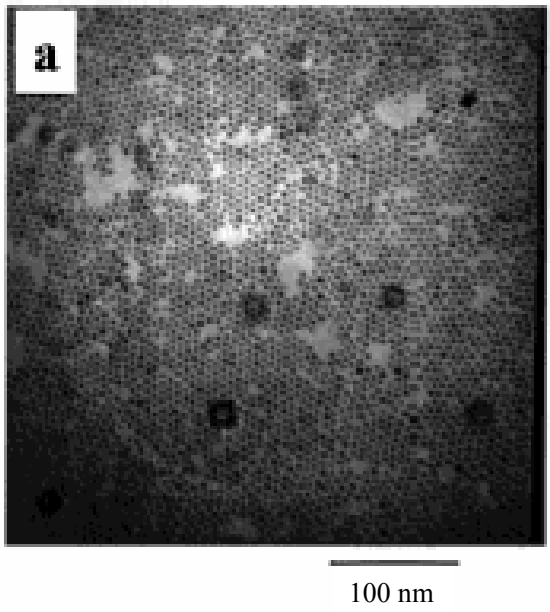

Fig. 1.11. A TEM image of Au NPs with an average diameter of 5.5 ± 0.6 nm, fabricated by the reduction of Au ions in a solution. (After Ref. 68)

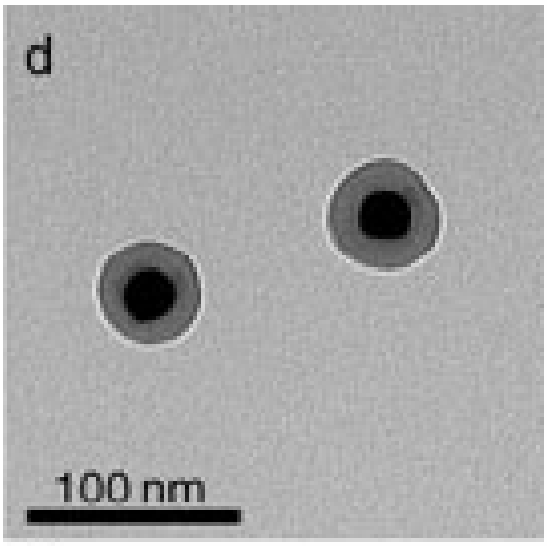

Fig. 1.12. A TEM image of Au NPs coated with block copolymer consisting of polystyrene and acrylic acid by chemical synthesis in a solution. (After Ref. 73)

–Chapter 2– Structural Changes Induced in TiO_2 by Swift Heavy Ions and Its Applications to Three-dimensional Lithography

Abstract

A rutile TiO_2 single crystal was irradiated by heavy ions with a high energy of the order of several tens of MeV. A good etching selectivity, where only the irradiated surface is well etched by hydrofluoric acid, is induced by the irradiation. Through x-ray diffraction and high-resolution electron microscopy, it became clear that the crystallinity became worse in the ion-irradiated region. It is considered that this amorphous region and the surrounding region are dissolved in hydrofluoric acid. Through the calculation of the ion energy, it was found that the etching always stopped at the depth where the electronic stopping power of the ion decayed to a critical value of 6.2 keV/nm, regardless of the ion species in the case of I, Br, Cu, and Ti ions. However, in the case of Ca ions with energies higher than about 72 MeV or Cl ions with energies higher than about 77 MeV, the irradiated top surface was not etched with hydrofluoric acid, but the inside surface several μm deep from the irradiated surface was etched. A calculation shows that the critical factor which determines whether the irradiated surface can be etched or not is the lateral energy density on the surface deposited by ions. The etched surface observed by atomic force microscopy is very smooth with a roughness of the order of nm. Therefore, a combination of ion irradiation and etching can be used as a novel fabrication method of nanostructures in rutile.

2.1 Introduction

Titanium dioxide (TiO_2), which has three crystalline polymorphs—rutile, anatase, and brookite—is attracting much attention due to its versatile application possibilities, such as semiconductor-electrolyte interfaces for photocatalysts [1–3] and solar cells [4,5]. Rutile TiO_2 single crystal, hereafter abbreviated as rutile, with a large birefringence and an excellent chemical resistance has wide potentialities in the fields of integrated optics and photonic devices. Titanium dioxide with a low optical loss at wavelengths in the vicinity of 1.5 μm can be used as a dopant for a planar optical waveguide for optical communication [6–9]. Amorphous TiO_2 with optical band gap at 3 eV is also available as a coating material for a window of Hg and Xe arc lamps [10].

A new paradigm emerged in the past decade, in which the band-structure concept of solid-state physics is applied to radio [11], microwave [12], and optical waves [13]. This has led to the invention of photonic crystal structures in two or three dimensions [14], which can be applied for outstanding optical devices for controlling electromagnetic waves such as a superprism [15,16], sharp-bend optical waveguide [17], and high-Q cavity [18]. Among numerous possible materials for photonic devices, semiconductors such as Si, GaAs, and InP have been most examined because of the abundant knowledge of microfabrication [19,20]. However, their refractive index values—e.g.,

3.5 for Si—are higher than 1.45 for SiO_2 [21,22], resulting in a high connection loss between the photonic crystal and SiO_2-based optical waveguide. Their band gaps are too small to make photonic crystals for visible light. Compared to these materials, the refractive index of rutile—2.4 perpendicular to the *c* axis or 2.7 parallel [23]—is close to SiO_2. Furthermore, its band gap is as wide as 3.0 eV [10] and its optical transmission loss is 10 times lower than that of Si at wavelengths near 1.5 μm [24]. For these reasons, rutile TiO_2 has a high potentiality for a photonic crystal.

In order to use rutile for integrated optics, photonic devices, and photonic crystals, a proper micro- or nano-fabrication process must be developed. Reactive ion etching cannot be used, since the fabricated side wall is not smooth enough to be used for photonic devices [25,26] such as an arrayed waveguide grating. Furthermore, a proper etching gas for rutile is not known. Although the sol-gel method [27,28] was used to fabricate an artificial opal structure of TiO_2 [29], shrinkage and cracking of the gel are unavoidable.

Since 2000, examples of nanofabrication using swift heavy ions have been reported [30]. When a swift heavy ion passes through most insulators, its energy is reduced while creating a heavily damaged zone along its path. The damaged zone can be made visible by chemical etching: thus the ion path and visible track are called the “latent track” and “etched track”, respectively. In many solid materials such as amorphous SiO_2, generation of etched tracks has been reported [30]. The sidewall of the etched track is very flat with a roughness of only a few nm [30]. Most of the earlier studies on that are concerned with identification of both particle species and their energy by observation of the etched track diameter, made possible by the chemical etch rate along a particle track dependent on projectile mass [31]. Other studies have focused on the very early stages of track formation and how excited electrons transfer energy to the network. The thermal spike model [32] is one of the most widely accepted theories for describing how ion energy is transferred rapidly and locally, introducing extremely high temperatures along the ion path. However, the model gives little information on the structure of the latent track and on the atomic mechanism underlying the enhanced etch rate of the latent track. In the present study, it is attempted to improve our understanding of these latter issues by approaching the problem from different angles, correlating the changes of x-ray diffraction (XRD), atomic force microscopy (AFM), SEM, and high-resolution transmission electron microscopy (HREM). Rutile TiO_2 single crystal was chosen to examine the defects generated in the particle tracks in order to develop three-dimensional fabrication with nm flatness, yet the structure of the latent track and the mechanism underlying the generation of latent tracks in these materials have not been investigated. The threshold ion energy necessary for fabrication is also discussed.

2.2 Experimental Procedures

The samples used in the present experiment are rutile TiO_2 single crystals (purity > 99.99%,

density 4.25 g/cm^3) synthesized by the Verneuil flame-fusion method. For most experiments, crystals with (100) faces were used, while those with (111) and (001) faces were also used to examine the effect of crystal orientation. Unless otherwise stated, the results obtained for the (100) crystal will be described. The samples were cut into plates 500 μm thick and polished. The root-mean-square roughness of the polished surface estimated by AFM is less than 0.8 nm.

Ion irradiation using a 12-MV tandem accelerator at the Tandem Accelerator Complex, University of Tsukuba (UTTAC) was performed at room temperature in a vacuum with a residual pressure below 1×10^{-3} Pa. The ions were irradiated to the sample either directly or through a free-standing Al or Au foil in order to diffuse them and to lower their energy. The structural change induced by ion irradiation was examined by XRD with a Rigaku FR-MDG spectrometer. The sample surface was observed by SEM, Hitachi S-2500CX and HREM, Hitachi H-9000NAR in addition to AFM. Chemical etching was performed with a hydrofluoric acid solution of 20% at room temperature.

2.3 Results

First, the etching rate of the rutile (100) crystal that had not been irradiated by ions was measured. Half of the rutile surface was covered with polytetrafluoroethylene tape and was etched with the hydrofluoric acid solution for seven days. No step was found by a profilometer with a resolution of several nm between the covered and noncovered regions, which means that rutile is not etched by hydrofluoric acid.

Figure 2.1(a) shows an AFM image of the rutile surface irradiated by Br ions with an energy of 120 MeV to a fluence of 8.0×10^{13} cm^{-2} through a 13-μm-thick Au stencil mask with a two-dimensional array pattern of square-shaped holes of 32×32 μm^2. An SEM image of the Au mask is also shown in Fig. 2.1(b). It is observed that the irradiated parts swelled due to expansion of the volume. The height of the step induced by the swelling increases with an increase in the irradiated fluence until it reaches a saturation value H shown in Table 2.1. Part of the surface of another rutile sample was covered by a clearly cut Si single-crystal wafer and irradiated by 110-MeV Cu ions to a fluence of 8.0×10^{13} cm^{-2}. Figure 2.2(a) shows an SEM image of the surface after being soaked in the hydrofluoric acid solution for 40 min. A clear 8.1-μm step with a very smooth sidewall can be seen between the irradiated and nonirradiated regions. The bottom surface of the irradiated region also looks very smooth. This smoothness is more clearly manifested by its AFM image shown in Fig. 2.2(b), where the maximum observable roughness is 2.5 nm.

The rutile (100) crystals were irradiated by Cu ions with an energy of 84.5 MeV to a fluence of either 7.0×10^{12}, 1.0×10^{13}, or 5.0×10^{13} cm^{-2}, and then etched with the hydrofluoric acid solution. Figure 2.3(a) shows the etched depth D as a function of the etching time. The kinked solid line represents the result of a least-squares fit to the data for the sample irradiated to a fluence of 5.0×10^{13} cm^{-2}. That the values of D start with negative values corresponds to the volume expansion

caused by irradiation. The D value increases linearly to a saturation value D_e of about 5.4 μm for the case of 1.0×10^{13} cm^{-2} and 6.4 μm for 5.0×10^{13} cm^{-2}. The dependence of D on the etching time was also examined for the (111) and (001) crystals irradiated by Cu ions to a fluence of 5.0×10^{13} cm^{-2}, and the result is shown in Fig. 2.3(b). A similar increase in D is seen, although D_e may depend on the surface orientation. Note that the reason of the small difference in D value for the (100) crystal between Figs. 2.3(a) and (b) is that the experiment was repeated to confirm the reproducibility.

As shown in Fig. 2.3(a), D_e depends on the irradiation fluence. Figure 2.4 shows the change in D_e as a function of the irradiation fluence of 84.5-MeV Cu ions. It can be seen that etching becomes possible at fluences higher than 5×10^{12} cm^{-2} and that D_e becomes saturated at D_s when the fluence exceeds a critical value of about 2×10^{13} cm^{-2}. The values of D_s observed for various ions with different energies are summarized in the rightmost column in Table 2.1. The value of D_s is always around 10 times higher than H, which strongly indicates that the structural change through which the etching becomes possible is closely related to the volume expansion.

Figure 2.5 shows XRD spectra of the (100) rutile irradiated by the 84.5-MeV Cu ions. Spectrum (i) is for the nonirradiated sample. Two peaks at 39.2° and 84.3°, to be assigned to the (200) and (400) planes, are seen. Curves (ii), (iii), (iv), and (v) are the spectra obtained in the samples after having been irradiated to respective fluences of 1.0×10^{12}, 3.0×10^{12}, 7.0×10^{12}, and 5.0×10^{13} cm^{-2}, while curve (vi) is the one after the sample used to obtain curve (iii) was etched in the hydrofluoric acid solution for 30 min. The two XRD peaks become smaller by the ion irradiation. Besides them, new peaks appear at 38.3° and 82.5° in spectrum (iii). They become smaller and move to smaller angles as the irradiation fluence increases, and finally disappear in spectrum (v).

In order to observe separate individual latent tracks, the rutile was irradiated by 84.5-MeV Cu ions to a low fluence of 1.0×10^{10} cm^{-2} and was observed by HREM. Two white spots located near the upper-left and lower-right corners in Fig. 2.6(a) are latent tracks. Another HREM image with a larger magnification shown in Fig. 2.6(b) indicates that the latent tracks is of a circular shape with a radius of 0.9 ± 0.2 nm and is surrounded by a dark region with a radius of about 1.8 nm.

Figure 2.7 shows the electronic stopping power S_e calculated by the SRIM 98 code [33] as a function of depth from the sample surface. The solid circle on each curve is plotted so that its value on the x axis corresponds to the value of D_s summarized in Table 2.1. The dotted curves in Fig. 2.7 imply the regions where etching was observed, while solid curves imply the nonetched regions. It is easily seen that D_s is smaller than the depth at $S_e = 0$, where ions are to stop. An important fact is that all the D_s values or the solid circles lie nearly on the solid horizontal line representing the positions where the electronic stopping power becomes 6.2 keV/nm irrespective of the ion species and acceleration energy. It is considered that a threshold electronic stopping power of 6.2 keV/nm is necessary for the ions to make the rutile structure suitable for etching.

The validity of the threshold electronic stopping power is further examined for different ions. As a first step, Ca ions with various energies were irradiated on the rutile crystals to a fluence of 8.0×10^{13} cm^{-2}. Then, they were examined by XRD and were etched in the hydrofluoric acid solution. Figure 2.8 shows the obtained XRD spectra for the nonirradiated crystal (a) and for the irradiated crystals at energies of 15.3 MeV (b), 31.9 MeV (c), 50.8 MeV (d), 72.3 MeV (e), and 82.0 MeV (f). Both the intensity of the 39.2° peak and that of the 84.3° peak decrease until 50.8 MeV and then return to their original values. As a surprising result, it was found that the sample surface irradiated by either the 15.3-MeV, 31.9-MeV, or 50.8-MeV ions was etched, while the one irradiated by the 72.3-MeV or 82.0-MeV ions was not.

Furthermore, another surprising result was obtained. Namely, after the crystals were irradiated by the Ca ions with various energies to a fluence of 8.0×10^{13} cm^{-2}, they were cut perpendicularly to the surface and immersed in the hydrofluoric acid solution. Figure 2.9 shows a typical cross-sectional SEM image taken for the sample irradiated by the 72.3-MeV ions. The position of the irradiated top surface and the direction of ions are indicated by arrows. The top surface was not etched, while an inside gap or a vacant hollow was created by etching about 4 μm below the surface. Similar inside gaps were always observed if the energy of Ca ions was higher than 72.3 MeV, and the position of the gap became deeper as the energy increased. For example, when the energy was 82.0 MeV, the gap was seen at depths between 5.4 and 7.7 μm from the top surface. Figure 2.10 shows the electronic stopping power S_e as a function of the depth. The dotted portion of each curve shows the depths where the hollow etching was made. Similar hollow etching was also observed in rutile irradiated by Cl ions with energies of 77.0 MeV and higher to a fluence of 1.0×10^{15} cm^{-2}.

2.4 Discussion

As shown in Fig. 2.5, the XRD peaks at 39.2° and 84.3° due to the rutile crystal structure decrease and move to smaller angles by the ion irradiation. According to the Bragg law, peaks at smaller angles are due to a structure with larger lattice constants. Therefore, it is clear that the irradiated layer of the sample became amorphous and increased its volume as evidenced by H shown in Table 2.1. Since rutile has the largest density among TiO_2 polymorphs, it is reasonable that the volume expands as the structure becomes amorphous. As shown by a comparison of spectra (i)–(v) in Fig. 2.5, the intensities of the crystal peaks scarcely change when the fluence exceeds 3.0×10^{12} cm^{-2}. Since the penetration depth of x rays for XRD is much deeper than that of ions [34], the crystal peaks in curves (iii)–(v) are considered to come from the undamaged rutile beyond the ion penetration depth. Therefore, it was assumed that the samples shown in (iii)–(v) became completely amorphous after having undergone a partly amorphous state. The surrounding dark region in the HREM lattice image in Fig. 2.6 corresponds to the region where the lattice constant becomes larger.

In order to examine whether the etched region is limited to the amorphous region or covers the

surrounding region, the following calculations were performed. In general, the ratio F of the area affected by the ion irradiation to the whole sample surface is known to be expressed by the equation

$$F = 1 - \exp(-A\phi), \tag{2.1}$$

where A is the area affected by the passage of a single ion and ϕ is the total ion fluence [35]. If only the amorphous region is regarded as the affected area, A is estimated from Fig. 2.6 to be $\pi \times 0.9^2$ nm^2 for the 84.5-MeV Cu ion. The solid curve in Fig. 2.11 shows the change in F as a function of ϕ for the 84.5-MeV Cu ions. If F represents the ratio of the area which can be etched, this result indicates that a fluence higher than about 3×10^{14} cm^{-2} is needed for the amorphous region to cover the whole sample surface. This fluence is more than one order of magnitude higher than the fluence at which the etching started. If a similar calculation is made for the area including the surrounding region with a radius of 1.8 nm, the dashed curve in Fig. 2.11 is obtained. It is indicated that the region to be etched covers about 50% of the sample surface at the irradiation fluence of 7.0×10^{12} cm^{-2}, where the surface etching was really observed in Fig. 2.4. From these calculations, it is highly probable that the surrounding region as well as the amorphous region can be etched by the hydrofluoric acid solution. The fact that the XRD peaks ascribed to the surrounding region also disappear by etching as clearly shown by a comparison between the curves (iii) and (v) in Fig. 2.5 is in a good agreement with the above assumption. The fact that the etching rate for the fluence of 7.0×10^{12} cm^{-2} is widely scattered and is slower than that for higher fluences as shown in Fig. 2.3(a) is also explained by the dotted curve in Fig. 2.11, which indicates that the etching becomes possible at fluences of the order of 10^{12} cm^{-2}.

Next, the mechanism of the inside hollow etching shown in Fig. 2.9 is discussed. Figure 2.10 indicates that the hollow etching is not simply understandable by S_e. It has been reported that a slower electron deposits a higher energy density to the target surface than a faster electron [36]. It has been also reported that a faster ion makes a smaller latent track than a slower ion with the same S_e [37]. These reports indicate that the velocity of electrons or ions is another factor besides S_e to decide the deposited energy and the radius of latent tracks. A semiempirical equation based on the Rutherford formula, in which the ion velocity is taken into account, has been developed to calculate the radial distribution of energy deposited on the sample surface around the path of ions [38]. Figure 2.12 shows calculation results of the radial distribution of energy deposited on a rutile surface around the path of ions as a function of the distance (or radius) from the ion incident point, obtained by assuming the same ion species and energies as those used in the present experiment. Solid curves with roman letters represent the conditions where the rutile surface was etched, while dotted curves with italics represent those where the inside was etched. All the solid curves lie above the dotted ones irrespective of the ion species and energy, which indicates that the energy deposited on the surface by incident ions is a more critical factor to determine whether the irradiated rutile can be etched or not.

Last, applications of the phenomena obtained in the present research are discussed. The sample to which the 120-MeV Br ions were irradiated through the two-dimensional pattern of holes, of which AFM image is shown in Fig. 2.1(a), was etched in the hydrofluoric acid solution for 40 min and subjected to SEM observation. Figure 2.13 shows the result. While the bottom surfaces of the etched cavities seem very flat, the sidewalls look as if they were rough. However, this sidewall structure is a replica of the shape of the holes. Therefore, this means that the present combination of ion irradiation and etching has a very precise resolution, capable of being applied as a nanofabrication method. By combining the irradiation of ions with various energies suitable for multilayer inside hollow etching, three-dimensional nanofabrication is also possible.

2.5 Conclusions

The structural change induced in rutile TiO_2 single crystals by irradiation of swift heavy ions has been investigated. Through x-ray diffraction and high-resolution electron microscopy analyses, it is considered that the latent tracks induced by the passage of ions become amorphous and that the lattice constants in the surrounding region become larger. If the rutile crystal is irradiated by swift heavy ions to a fluence higher than the critical value at which the latent tracks and their surrounding regions presumably cover a large portion of the rutile surface, the surface becomes possible to be etched by hydrofluoric acid. When Ti, Cu, Br, or I ions are irradiated, the etching continues to the depth from the surface where the electronic stopping power decays to a threshold value of 6.2 keV/nm, regardless of the ion species. Excepting the above, the surface cannot be etched even if the stopping power exceeds the threshold when the ion is Cl or Ca. However, in this case, a hollow vacancy layer is etched inside the sample. By calculating the radial distribution of energy deposited on the surface by the incident ions, it becomes evident that there is a clear demarcation in the radial energy distribution which determines whether the surface can be etched or not. The bottom and side surfaces of the etched cavities were found to be very smooth in the order of nm. Therefore, combination of irradiation by swift heavy ions with various energies and following etching is believed to be a good processing method to fabricate three-dimensional nanostructures.

References for Chapter 2

[1] A. Fujishima and K. Honda, Nature **238**, 37 (1972).

[2] A. Mills and S. Le Hunte, J. Photochem. Photobiol. A **108**, 1 (1997).

[3] H. Liu, H. T. Ma, X. Z. Li, W. Z. Li, M. Wu, and X. H. Bao, Chemosphere **50**, 39 (2003).

[4] R. K. Karn and O. N. Srivastava, Int. J. Hydrogen Energy **24**, 27 (1999).

[5] M. G. Kang, N. G. Park, Y. J. Park, K. S. Ryu, and S. H. Chang, Sol. Energy Mater. Sol. Cells **75**, 475 (2003).

[6] C. Chaudhari and D. K. Gautam, Opt. Commun. **181**, 61 (2000).

[7] E. M. Yeatman, M. M. Ahmad, O. McCarthy, A. Vannucci, P. Gastaldo, D. Barbier, D. Mongardien, and C. Moronvalle, Opt. Commun. **164**, 19 (1999).

[8] C. Tosello, F. Rossi, S. Ronchin, R. Rolli, G. C. Righini, F. Pozzi, S. Pelli, M. Fossi, E. Moser, M. Montagna, M. Ferrari, C. Duverger, A. Chiappini, and C. De Bernardi, J. Non-Cryst. Solids **284**, 230 (2001).

[9] Z. Jiwei, Y. Tao, Z. Liangying, and Y. Xi, Ceram. Int. **25**, 667 (1999).

[10] T. C. Lu, L. B. Lin, S. Y. Wu, J. Chen, and Y. Y. Ahang, Nucl. Instrum. Methods Phys. Res. B **191**, 236 (2002).

[11] D. F. Sievenpiper and E. Yablonovitch, Phys. Rev. Lett. **80**, 2829 (1998).

[12] W. M. Robertson and G. Arjavalingam, Phys. Rev. Lett. **68**, 2023 (1992).

[13] V. V. Poborchii, T. Tada, and T. Kanayama, Appl. Phys. Lett. **75**, 3276 (1999).

[14] E. Yablonovitch, Phys. Rev. Lett. **58**, 2059 (1987).

[15] S. Y. Lin, V. M. Hietala, L. Wang, and E. D. Jones, Opt. Lett. **21**, 1771 (1996).

[16] H. Kosaka, T. Kawashima, A. Tomita, M. Notomi, T. Tamamura, T. Sato, and S. Kawakami, J. Lightwave Technol. **17**, 2032 (1999).

[17] A. Mekis, J. C. Chen, I. Kurland, S. Fan, P. R. Villeneuve, and J. D. Joannopoulos, Phys. Rev. Lett. **77**, 3787 (1996).

[18] P. R. Villeneuve, S. Fan, J. D. Joannopoulos, K. Y. Lim, G. S. Petrich, L. A. Kolodziejski, and R. Reif, Appl. Phys. Lett. **67**, 167 (1995).

[19] A. Birner, A. P. Li, F. Müller, U. Gösele, P. Kramper, V. Sandoghdar, J. Mlynek, K. Busch, and V. Lehmann, Mater. Sci. Semicond. Process. **3**, 487 (2000).

[20] C. Weisbuch, H. Benisty, M. Rattier, C. J. M. Smith, and T. F. Krauss, Synth. Met. **116**, 449 (2001).

[21] R. H. Klazes, M. H. L. M. van der Broek, J. Bezemer, and S. Raderlaar, Philos. Mag. B **45**, 377 (1982).

[22] I. H. Malitson, J. Opt. Soc. Am. **55**, 1205 (1965).

[23] D. Mergel, Thin Solid Films **397**, 216 (2001).

[24] S. Yamazaki, N. Hata, T. Yoshida, H. Oheda, A. Matsuda, H. Okushi, and K. Tanaka, J. Phys. Colloq. **42**, C4-297 (1981).

[25] C. Cardinaud, M. C. Peignon, and P. Y. Tessier, Appl. Surf. Sci. **164**, 72 (2000).

[26] S. Norasetthekul, P. Y. Park, K. H. Baik, K. P. Lee, J. H. Shin, B. S. Jeong, V. Shishodia, E. S. Lambers, D. P. Norton, and S. J. Pearton, Appl. Surf. Sci. **185**, 27 (2001).

[27] S. Shimada, K. Miyazawa, and M. Kuwabara, Jpn. J. Appl. Phys., **41**, L291 (2002).

[28] M. Lanata, M. Cherchi, A. Zappettini, S. M. Pietralunga, and M. Martinelli, Opt. Mater. **17**, 11 (2001).

[29] W. Hu, H. Li, B. Cheng, J. Yang, Z. Li, J. Xu, and D. Zhang, Opt. Lett. **20**, 964 (1995).

[30] K. Awazu, S. Ishii, K. Shima, S. Roorda, and J. L. Brebner, Phys. Rev. B **62**, 3689 (2000).

[31] G. Fiedler, J. Aschenbach, W. Otto, T. Rautenberg, U. Steinhauser, and G. Siegert, Nucl. Instrum. Methods **147**, 35 (1977).

[32] G. Bonfiglioli, A. Ferro, and A. Monjoni, J. Appl. Phys. **32**, 2499 (1961).

[33] *The Stopping Power and Ranges of Ions in Matter Vol. I*, edited by J. F. Ziegler (Pergamon, New York, NY, 1985).

[34] http://www-cxro.lbl.gov/

[35] M. Toulemonde, E. Balanzat, S. Bouffard, J. J. Grob, M. Hage-Ali, and J. P. Stoquert, Nucl. Instrum. Methods Phys. Res. B **46**, 64 (1990).

[36] R. Kats and E. J. Kobetich, Phys. Rev. **186**, 344 (1969).

[37] A. Meftah, F. Brisard, J. M. Costantini, M. Hage-Ali, J. P. Stoquert, F. Studer, and M. Toulemonde, Phys. Rev. B **48**, 920 (1993).

[38] M. P. R. Waligorski, R. N. Hamm, and R. Kats, Nucl. Tracks Radiat. Meas. **11**, 309 (1986).

Table 2.1. Saturation values of the height of swollen surface H induced by ion irradiation and the etched depth D_s.

Ion species	Energy [MeV]	H [μm]	D_s [μm]
I	78.8	0.5	4.6
Br	120	0.9	8.1
	50	0.4	4.0
Cu	110	0.9	8.1
	84.5	0.7	6.3
	15	0.1	0.9
Ti	100	1.0	9.6

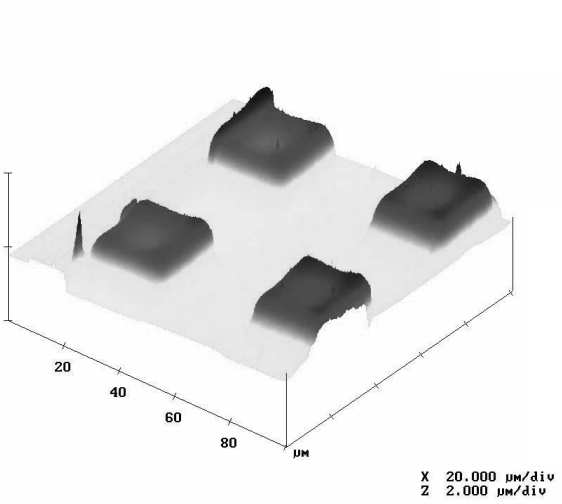

(a)

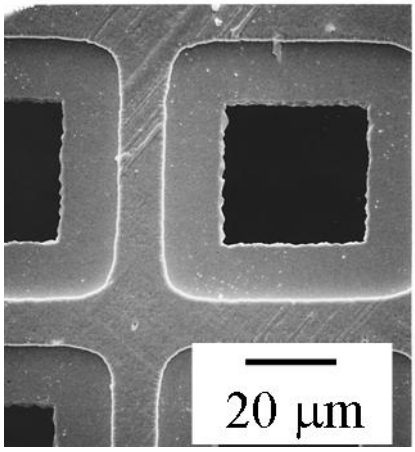

(b)

Fig. 2.1. (a) An AFM image of the rutile surface irradiated by 120-MeV Br ions to a fluence of 8.0 $\times 10^{13}$ cm^{-2} through a Au mask with square-shaped holes. (b) An SEM image of the Au mask.

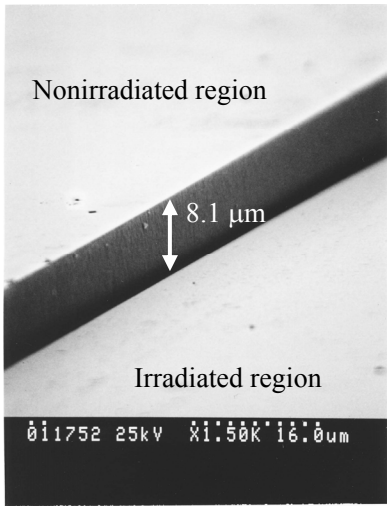

(a)

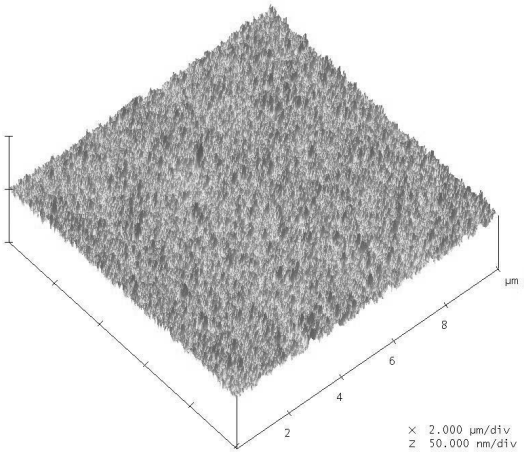

(b)

Fig. 2.2. (a) An SEM image of the rutile surface irradiated with 110-MeV Cu ions to a fluence of 8.0×10^{13} cm^{-2} and etched by 20% hydrofluoric acid. The upper left area was covered with a Si wafer during the irradiation. (b) An AFM image of the etched surface.

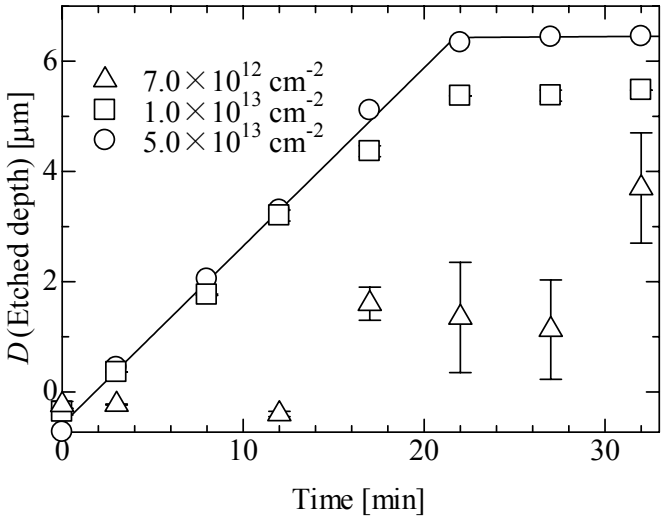

(a)

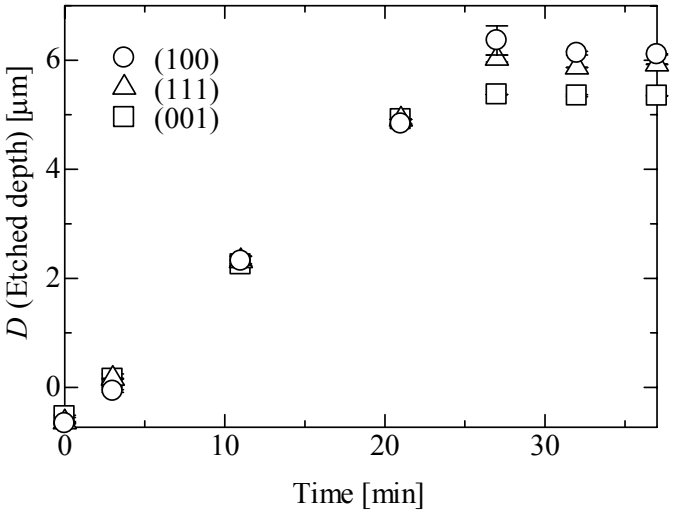

(b)

Fig. 2.3. (a) Relation between the etching time and the etched depth D, observed for the samples irradiated by 84.5-MeV Cu ions to fluences of 7.0×10^{12} cm^{-2} (triangles), 1.0×10^{13} cm^{-2} (squares), and 5.0×10^{13} cm^{-2} (circles). The kinked line represents the result of least-squares fit to the data for the sample irradiated to 5.0×10^{13} cm^{-2}. (b) Effect of the surface orientation on the etching property for the samples irradiated to a fluence of 5.0×10^{13} cm^{-2}.

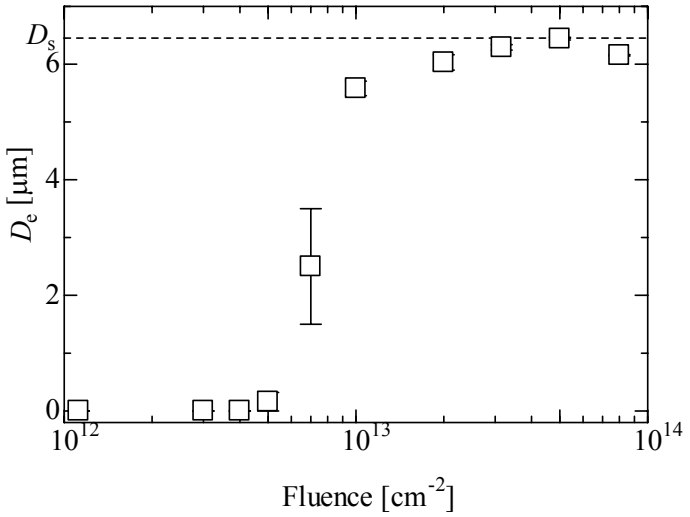

Fig. 2.4. Change in D_e as a function of irradiated fluence of 84.5-MeV Cu ions.

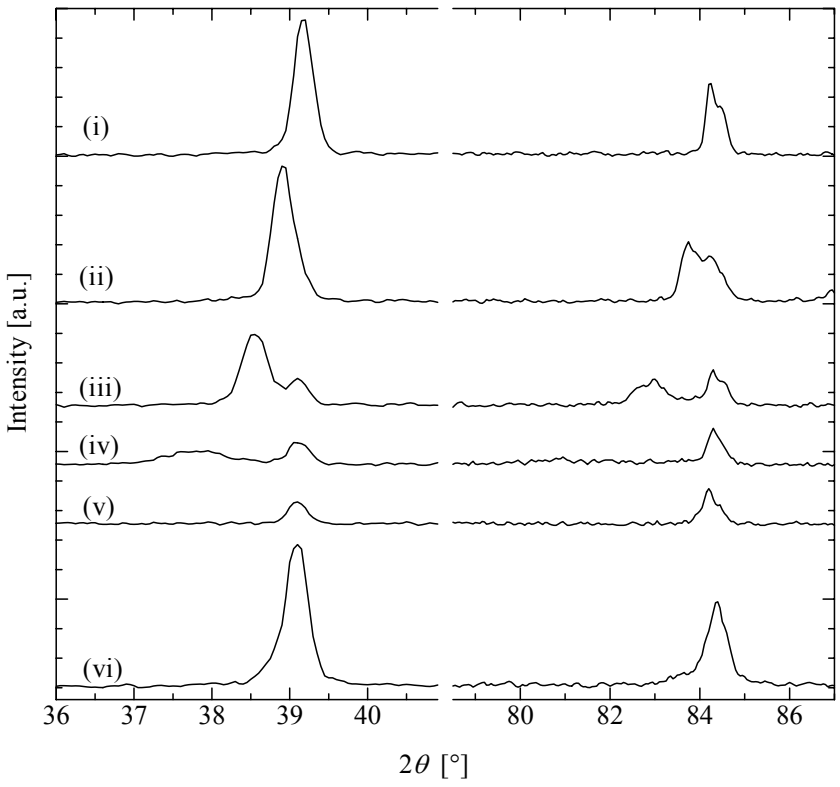

Fig. 2.5. X-ray diffraction spectra of the nonirradiated rutile (i), after irradiation of 84.5-MeV Cu ions to fluences of 1.0×10^{12} (ii), 3.0×10^{12} (iii), 7.0×10^{12} (iv), and 5.0×10^{13} cm^{-2} (v). Curve (vi) is the spectrum of the sample (iii) after having been etched in hydrofluoric acid for 30 min. The peaks at 39.2° and 84.3° are due to the (200) and (400) planes, respectively.

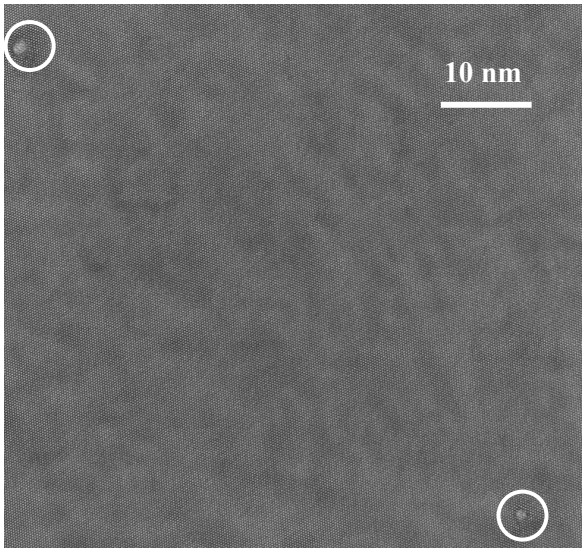

(a)

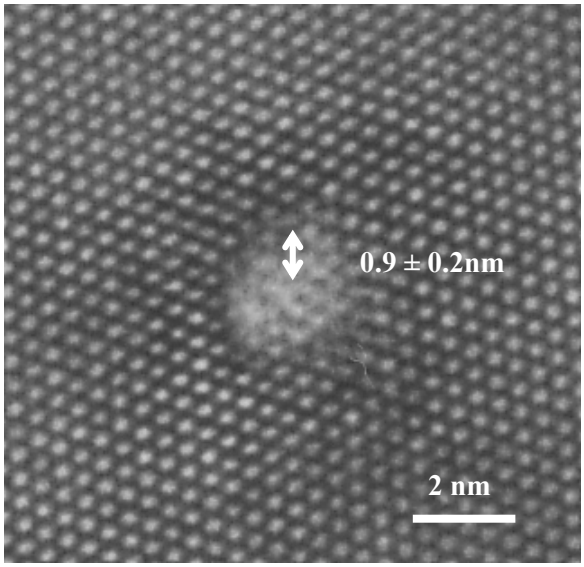

(b)

Fig. 2.6. High-resolution electron microscopy images of the rutile irradiated by 84.5-MeV Cu ions to a fluence of 1.0×10^{10} cm^{-2}. A bright image and a lattice image are shown in (a) and (b), respectively.

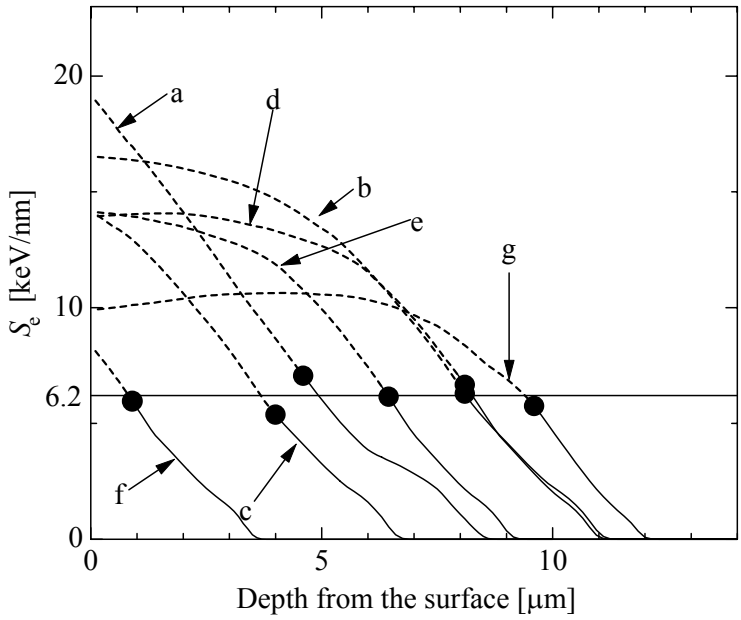

Fig. 2.7. Calculated electronic stopping power S_e as a function of the depth from the surface. a: 78.8-MeV I ions, b: 120-MeV Br ions, c: 50-MeV Br ions, d: 110-MeV Cu ions, e: 84.5-MeV Cu ions, f: 15-MeV Cu ions, and g: 100-MeV Ti ions. The *x*-axis values of the solid circles indicate the depths where the etching stopped.

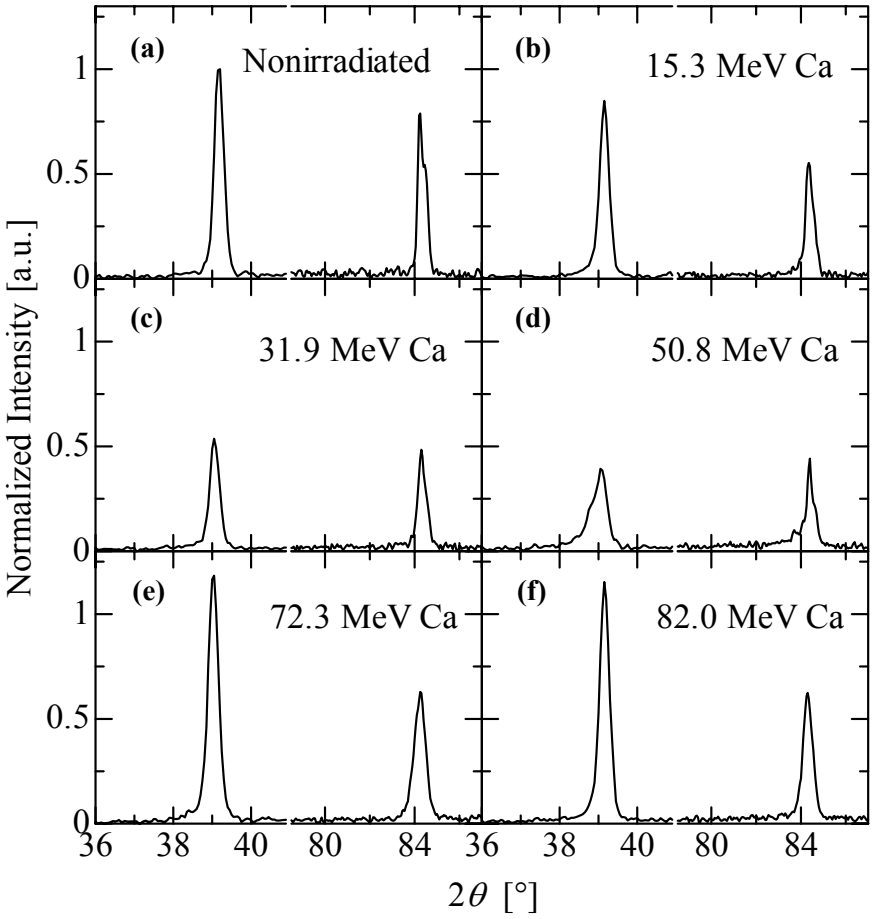

Fig. 2.8. X-ray diffraction spectra obtained before and after irradiation of Ca ions to a fluence of 8.0×10^{13} cm^{-2}. (a) Before irradiation. (b)–(f) After irradiation of ions with energies of 15.3 MeV (b), 31.9 MeV (c), 50.8 MeV (d), 72.3 MeV (e), and 82.0 MeV (f).

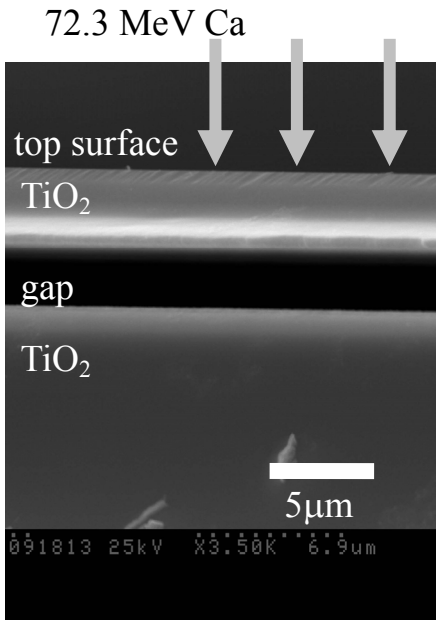

Fig. 2.9. A cross-sectional SEM image of the sample etched following the irradiation of the 72.3-MeV Ca ions to a fluence of 8.0×10^{13} cm^{-2}.

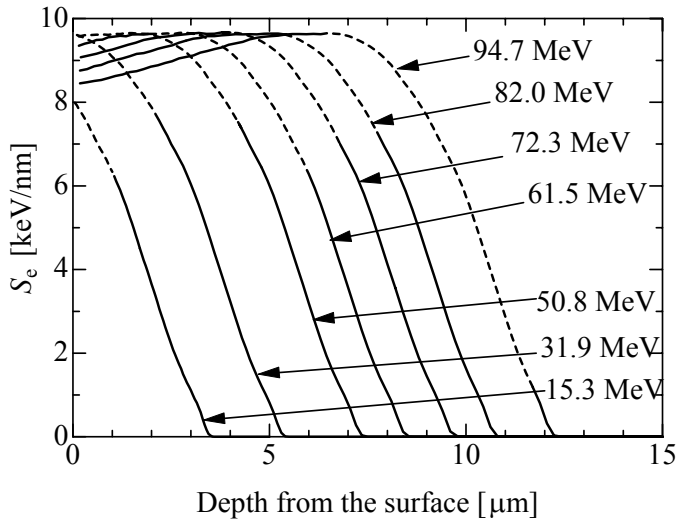

Fig. 2.10. Calculated values of S_e of Ca ions injected with various energies as a function of the depth from the sample surface. The dotted portion of each curve represents the depths where the hollow etching was made.

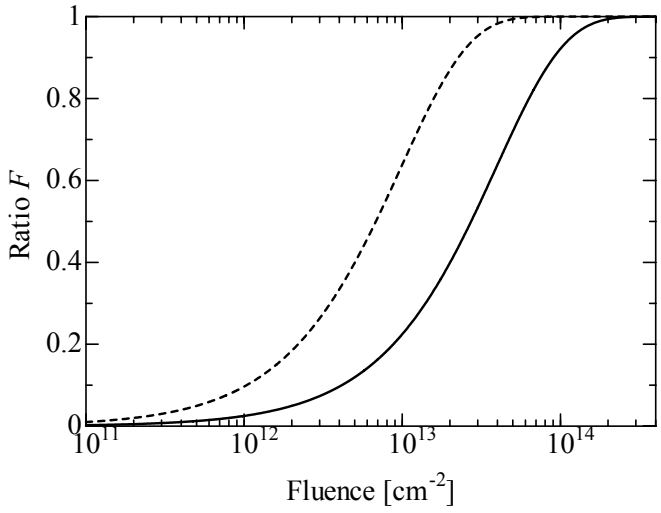

Fig. 2.11. Change in the ratio F of the area affected by the irradiation of 84.5-MeV Cu ions to the entire sample surface. The solid curve is the result obtained by assuming that the area affected is limited to the amorphous region, while the dotted one is under the assumption that the area includes the surrounding region.

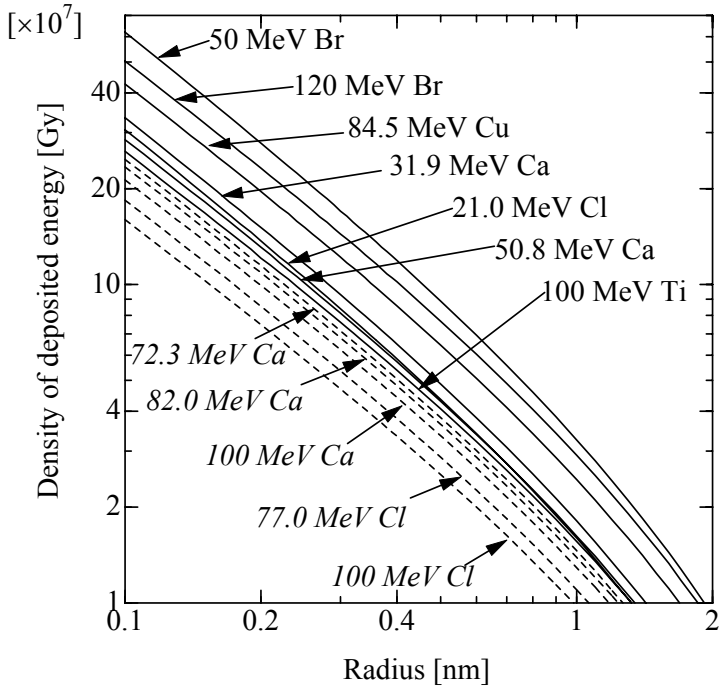

Fig. 2.12. Radial distribution of energy deposited on the rutile surface as a function of the distance from the ion incident point. Solid curves with roman letters mean that the surface was etched, while dotted ones with italics represent that the inside was etched.

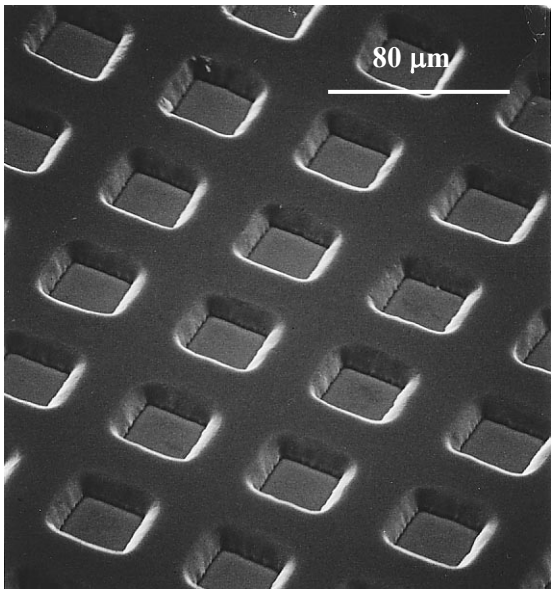

Fig. 2.13. An SEM image of the etched surface with 20% hydrofluoric acid of the same sample shown in Fig. 2.1(a). The sidewall pattern is a replica of that of the holes through which the ions were irradiated.

–Chapter 3– Plasmonic Activity on Au Nanoparticles Embedded in Nanopores Formed in a Surface Layer of SiO_2 Glass by Swift-heavy-ion Irradiation

Abstract

Swift heavy ions were irradiated into SiO_2 glass by selecting the ion species and its energy in order to induce the largest damaged regions. These regions were then selectively etched by hydrofluoric acid vapor to form nanopores on the glass surface. Subsequently, Au nanoparticles were embedded into the nanopores by vacuum evaporation, followed by thermal treatment. In the new plasmonic structure obtained with these procedures, the localized surface plasmon excitation wavelength induced around the Au nanoparticles was found to show a redshift, which agreed well with the theoretical calculation, when water, introduced into the nanopores, surrounded the nanoparticles. This indicates that the fabricated structure can be used as a sensing element to detect the adhesion of substances such as biomolecules to the nanoparticles by measuring the redshift.

3.1 Introduction

When metal nanoparticles (NPs) are illuminated by light of an appropriate wavelength, localized surface plasmons (LSPs) are excited which absorb the light significantly. Since the LSP excitation wavelength shifts toward a longer wavelength with an increase in the refractive index around NPs [1–5], the attachment of a substance to the NPs can be detected by observing this shift. This is applicable to sensors, especially in the biomolecular field. In addition, the electric field enhancement around NPs induced by the LSP excitation can be applied to highly active photocatalysts [6] and to surface-enhanced Raman scattering [7]. It is also attractive in that various devices can be downsized, since it can be easily induced by simple illumination with light of an appropriate wavelength.

Metal NPs are often arranged two-dimensionally on a substrate in order to apply them to devices by using several methods, such as the Langmuir-Blodgett method. However, the range of their application would be enlarged if they could be arranged three-dimensionally. One possible way to realize this is the formation of a large number of nanopores in a surface layer of the substrate and the subsequent embedding of the NPs into the nanopores. If such a structure is obtained in a transparent substrate such as SiO_2 glass or in an optical waveguide, it would help to investigate the plasmonic property of metal NPs by allowing their optical absorption spectra to be observed. This would further expand their application to high-performance plasmonic devices, since the electric field should be enhanced by the realization of a permissible mode in the waveguide and by the LSP excitation of metal NPs.

As a possible method to form nanopores on the surface of SiO_2 glass, the latent-track etching method is fascinating. Namely, if heavy ions with a high energy in the order of MeV are implanted on the surface of an insulator, cylindrical damage occurs, called “latent tracks”. These tracks, one for

each ion, are formed along the ion paths, with diameters ranging from a few to ~10 nm and depths of a few μm [8–15]. The etching rate for latent tracks in SiO_2 glass by hydrofluoric acid is approximately five times as high as that of nonirradiated regions [10], by which conical nanopores are formed on the surface [10,15]. Recently, as a further development, it has been reported that deep cylindrical nanopores with an ultrahigh-aspect-ratio of ~40 can be obtained in SiO_2 glass using hydrofluoric acid vapor for etching [14]. Since metal NPs should be embedded more in cylindrical nanopores than in conical ones, vapor etching was employed in the present experiment.

It has been reported that precipitation of metal NPs has been realized by implanting many swift heavy ions in insulators [16,17]. However, since the fabricated NPs are inevitably completely surrounded by the insulators, they cannot be used as plasmonic sensors to detect refractive index changes around the NPs. On the other hand, in the present method, the metal NPs are in nanopores intensively formed by swift-heavy-ion irradiation in a surface layer of SiO_2 glass. Namely, if a certain change in refractive index around the NPs is induced by a substance introduced into the nanopores, such a change can be easily detected. As far as this viewpoint is concerned, our fabrication method is superior to the ones reported in [16,17].

One of the most desirable materials for embedding NPs is Au, since Au NPs are chemically inert and their LSP excitation wavelength is in the range of visible light. This paper discusses the most appropriate ion irradiation condition for forming an adequate number of cylindrical nanopores with a desirable diameter in a surface layer of SiO_2 glass by taking into account the thermal effect of ion irradiation. The formation of a new plasmonic structure with a three-dimensional distribution of Au NPs, by the above-mentioned method, is also reported. Furthermore, the plasmonic activity of the structure measured in two different dielectric environments, air and water, is reported.

3.2 Experimental Procedures

3.2.1 Calculation of the Radius of the Melted Region

It is assumed that latent tracks are formed if the lattice temperature is increased above the melting point as a result of the interaction between electrons excited by ions and phonons in the material [9,13,18,19]. The latent-track radii experimentally obtained for quartz [9], $BaFe_{12}O_{19}$ [9] and rutile TiO_2 single crystal [13] have been reported to agree well with the radii of melted regions estimated by calculations using heat diffusion equations, in which the effect of ion irradiation is taken into account [9,13]. Therefore, a similar calculation was performed for SiO_2 glass. When a solid material is hit by a single ion, the electronic temperature T_e and lattice temperature T are expressible by the following Eqs. (3.1) and (3.2) [9,13,18,19].

$$C_e \frac{\partial T_e}{\partial t} = \nabla \cdot (K_e \nabla T_e) - g(T_e - T) + A(r,t), \tag{3.1}$$

$$C(T)\frac{\partial T}{\partial t} = \nabla \cdot (K(T)\nabla T) + g(T_e - T), \quad (3.2)$$

where C_e and K_e are the electronic specific heat per unit volume and the electronic thermal conductivity, respectively, while $C(T)$ and $K(T)$ are the corresponding values for the lattice. Further, g is the coupling constant governing the electron-phonon interaction. The term $A(r,t)$, which is expressed by the equation,

$$A(r,t) = A_0 D(r) \exp(-t/\tau), \quad (3.3)$$

is the energy transferred from a single ion to the electrons in a unit volume at a radial distance r from the ion path during a unit period of time at a time t, if $t = 0$ is taken as the instant of the arrival of the ion at the surface of the material. Here, A_0 is a constant, $D(r)$ is the initial spatial distribution of the energy transferred to the electrons from the ion [20] and τ is the mean flight time of the delta-ray electrons. The constant A_0 is calculated from the equation,

$$S_e = \int_{r=0}^{\infty}\int_{t=0}^{\infty} A(r,t)2\pi r\,dr\,dt = A_0 \int_{r=0}^{\infty} D(r)2\pi r\,dr \int_{t=0}^{\infty} \exp(-t/\tau)dt, \quad (3.4)$$

where S_e is the electronic stopping power of the ion.

Using these equations, T and the radius of the melted region induced in SiO_2 glass were estimated as functions of the ion acceleration energy, which ranged from 1 to 200 MeV for the implantation of Si, Cl, Se, Br, I, and Au ions, assuming that T was 300 K before the ion implantation. While the thermodynamic parameters were approximated by the values for quartz, since those for SiO_2 glass are unknown, the temperature dependences of $C(T)$ and $K(T)$ were based on [18], and the electronic stopping power was calculated for each ion using the SRIM 2006 code [21], under the condition that the density of SiO_2 glass is 2.2 g cm^{-3} [18].

3.2.2 Materials

Three kinds of samples were used in the present experiment. The first one, sample A, was a 10 × 10 × 1.2 mm^3 substrate with a ~500-nm-thick SiO_2 glass surface layer, which was obtained by the oxidation of a 1.2-mm-thick SiO_2 glass substrate with a 440-nm-thick Si single crystal layer on the surface (Shin-Etsu Chemical) in an O_2/H_2O mixture vapor at 1000 °C for 65 min. Sample B was purchased from KST World Corp. It was a 10 × 10 × 0.5 mm^3 Si single crystal substrate with a 2-μm-thick thermally grown SiO_2 glass layer. Sample C was a 13 × 20 × 0.7 mm^3 optically polished SiO_2 glass substrate purchased from Ohyo Koken Kogyo Co., Ltd. They were irradiated by 137-MeV Au ions to a fluence of 5 × 10^9 cm^{-2} at the Tandem Accelerator Complex, University of Tsukuba (UTTAC) under a pressure below 1 × 10^{-3} Pa at room temperature. Using the SRIM 2006 code [21], the average projected range was calculated to be ~17 μm for 137-MeV Au ions implanted into SiO_2 glass.

Sample A was etched in a 4.8% hydrofluoric acid solution after the ion irradiation in order to

perforate the nanopores by etching the latent tracks formed in the surface layer. The perforated surface of sample A was observed by SEM (Hitachi High-Technologies S-4800) to measure the radii of the nanopores. Then, the nanopore radii were compared with those reported in [15], in which nanopores were also formed in SiO_2 glass obtained by an oxidation process similar to the one used to prepare sample A. On the other hand, for samples B and C, a vapor of 18.4% hydrofluoric acid was used to obtain nanopores, and chemically stable Au was then vacuum-evaporated on the sample surface. This sample, together with Au in the nanopores, was subsequently treated thermally at 300 °C for 30 min. With these procedures, Au was embedded into the nanopores, taking the shape of nanoparticles.

While sample B was used for surface and cross-sectional observations by SEM, since a smooth cross-section was obtainable by the cleavage of the Si substrate, sample C, which was transparent, was used to measure the absorption from 300 to 800 nm with a spectrophotometer (Shimadzu UV-2500) before and after the embedding of Au NPs. Furthermore, in order to investigate the dependence of plasmonic activity on the dielectric environment around the Au NPs, water was dropped on the sample surface and the absorption spectrum was measured.

3.3 Results and Discussion

It has been previously reported by the author and colleagues that in the case of Cl and Ca ions, latent tracks cannot be formed on the surface of a rutile TiO_2 single crystal if the ion velocity is too high [12]. It has also been reported that the latent track on a $Y_3Fe_5O_{12}$ film becomes smaller if the speed of the Kr or Xe ions is faster [8]. This is due to the fact that the reaction cross-section becomes smaller with an increase in ion velocity. Therefore, the latent track should show an ion species-dependent largest radius at a certain ion energy.

In order to effectively embed Au NPs into nanopores, large nanopores are desirable. Therefore, it was necessary to choose the best ion species and acceleration energy to perforate the nanopores with the maximum radius before starting the ion implantation experiments. With this view, the author first examined the radius of the region melted upon ion irradiation, which was in agreement with that of the latent track as mentioned above [9,13], for as many ion species as possible.

Figure 3.1 shows the radius of the melted region that should result from the implantation of a single ion into the SiO_2 glass as a function of the acceleration energy, calculated for Si, Cl, Se, Br, I, and Au ions. For Si, Cl, and Se ions, the maximum radius is seen in a certain energy range. It reaches about 0.35 nm at 7–10 MeV for Si, 0.75 nm at 10–20 MeV for Cl, and 2.75 nm at 150 MeV for Se. On the other hand, as shown in Fig. 3.1, the radius becomes larger with an increase in the atomic number and with an increase in the acceleration energy, at least as far as in the energy range below 200 MeV for Br, I, and Au, which have atomic numbers larger than those of Si, Cl, and Se. In view of the objective of the present research to create nanopores with the largest radius, Au was the

most appropriate of the six ion species implanted, since it yielded the largest melted region, as shown in Fig. 3.1.

Therefore, it was decided to compare the calculated radius of the melted region with the average radius of the perforated nanopores for Au ions. For this purpose, the SiO_2 glass sample A was irradiated by 137-MeV Au ions and perforated by wet etching in a 4.8% hydrofluoric acid solution for 7 min at room temperature. A comparison was also made to the radii of nanopores that were reported in the literature [15] to have been ion implanted and perforated by etching, similarly to the present research. Namely, for each ion irradiation condition, the radius of the melted region was calculated as shown in Fig. 3.1, and re-plotted on the abscissa in Fig. 3.2. On the other hand, the radii of the nanopores reported in [15] are plotted on the vertical axis as open circles, while the open square represents the average radius of the nanopores, as estimated from the surface SEM image shown in the inset, which were observed for sample A after the ion implantation and perforation by etching. This should not detract much from the value of the comparison, since the fact that the results obtained in different researches lie on a single smooth curve demonstrates well the validity of the present objective to predict the radii of perforated nanopores from the calculated radii of melted regions. The average radius of the nanopores becomes larger with an increase in the calculated radius of the melted region, as shown in Fig. 3.2, which in turn indicates that the average pore or latent-track radius induced in any ion irradiation condition is a function of the radius of the melted region. This is consistent with previous findings that the energy transferred from ions to electrons in substances governs the formation of latent tracks [9,12,13]. Here, the observed nanopore radius is significantly larger than the calculated one. This is due to the fact that hydrofluoric acid can also etch nonirradiated regions, although the etching speed there is slow compared to that for the irradiated regions.

As mentioned above, in order to effectively embed Au NPs into nanopores, nanopores with large radii are desirable. Therefore, after examining the result shown in Fig. 3.2, it was decided to use 150-MeV Au ions, since they had the largest atomic number and energy of the ions that could be emitted with a sufficiently large beam current by our ion accelerator. An Al foil with a thickness of 0.8 μm was set between the ion accelerator and the sample, to ensure that the ions were diffused and implanted on the sample surface uniformly. The average ion energy to hit the sample surface after having passed through the foil was calculated to be 137 MeV.

The insets (i)–(v) in Fig. 3.3 show schematically the nanostructure fabrication procedures, from the ion irradiation to the embedding of Au NPs, while (a), (b), and (c) show photographs of sample C on a nonwoven cotton mesh taken after the processes of Au evaporation (iii), annealing (iv), and the removal of the Au film (v), respectively. In process (i), in order to form latent tracks, Au ions were implanted on either sample B or C with an energy of 137 MeV. In the next process (ii) to form nanopores, the ion irradiated sample was kept at 36 °C and exposed to a vapor of 18.4% hydrofluoric

acid at 20 °C for 40 min to etch only the latent tracks. Next, in order to embed Au into the nanopores (iii), Au was deposited on the perforated SiO_2 glass sample by vacuum evaporation to a thickness that corresponded to 50 nm if it were deposited on a flat substrate, as determined by measurement with a quartz crystal microbalance. During the process, only a part of the evaporated Au is expected to have been embedded into the nanopores, while the majority seems to have been deposited on the surface of the SiO_2 glass as a film, since a metallic luster was observed, as shown in (a). Then, the sample was heated at 300 °C for 30 min in N_2 (iv), which allowed the contact between the Au film and the SiO_2 glass to become weak enough so that it could be peeled off, as shown in (b). By using these procedures, a structure with Au NPs embedded into nanopores was obtained (v). The area where the Au was evaporated looks purple, as shown in Fig. 3.3(c), which indicates that optical absorption was induced over a wide area as a result of the LSP excitation around the Au NPs embedded in the nanopores. This in turn indicates that nanopores with embedded Au NPs were formed over the entire sample surface, as expected.

Figures 3.4(a) and (b) show SEM images of the surface and cross-section of sample B, observed after irradiation with 137-MeV Au ions to a fluence of 5×10^9 cm^{-2} and then etched for 40 min, namely at the stage corresponding to Fig. 3.3(ii). The direction of the ion irradiation was perpendicular to the surface, as indicated by the arrows. It is clear that high-aspect-ratio cylindrical nanopores with a diameter of ~50 nm can be formed by the selective etching of latent tracks. Here, as shown in Fig. 3.4(a), some nanopores overlap with each other, since the ions hit the surface at random. These overlaps could be eliminated if nano-patterned masks thick enough to shield ions, such as the ones fabricated by the LIGA process or nanoimprint lithography, can be used [22].

Surface and cross-sectional SEM images of sample B, obtained after the removal of the deposited Au film by the thermal treatment, or at the stage corresponding to Figs. 3.3(v) and (c), are shown in Figs. 3.5(a) and (b), respectively. In these figures, spherical substances with radii of several tens of nm, which indicate the presence of Au NPs, can be seen in the nanopores after the Au embedment. Note that such spherical substances cannot be seen in Fig. 3.4 obtained before the embedment. Figures 3.6(a) and (b) show histograms of the diameters of the nanopores or black regions in surface SEM images observed before and after the Au NP embedment, respectively.

Figure 3.7 shows surface SEM images observed in sample C, which was perforated and etched similarly to sample B. Compared to the image taken before the Au embedment (a), the one taken after the embedment (b) shows that Au NPs are in the nanopores. As shown in Figs. 3.4, 3.5, and 3.7, the Au NPs seem to be present only in the nanopores, not on the top surface, indicating that, as expected, the excess Au deposited on the top surface in the shape of a film was completely removed by the thermal treatment, as shown in Figs. 3.3(iv) and (v).

Figure 3.8 shows the optical absorption spectra measured for sample C at the as-received stage (a), after the nanopore etching (b), after the embedment of Au NPs into the nanopores (c), and after

introducing water into the nanopores with the Au NPs embedded (d). The inset shows the spectra (a) and (b) enlarged for the wavelength range from 560 to 800 nm. The significant increase in absorbance seen in the sample after the formation of nanopores at wavelengths shorter than about 560 nm (spectrum (b)) is due to the Rayleigh scattering induced by the increase in surface roughness during the nanopore formation process, including the vapor etching. On the other hand, the absorbance at wavelengths longer than 560 nm becomes low compared with the as-received sample, which means that the transmittance is increased in this wavelength region by perforating the SiO_2 glass. This is quite reasonable since the presence of air in the nanopores, which covers ~10% of the surface of the SiO_2 glass, decreases the difference between the refractive indices of the two materials at each side of the incident plane of the light. This should be beneficial for optical applications of the present structure.

Figure 3.9 compares the absorption spectra of sample C with nanopores and embedded Au NPs before and after dropping water on the surface. Here, in order to eliminate the above-mentioned effects of Rayleigh scattering and an increase in transmittance, and to clarify the effect induced by the embedding of Au NPs, differential absorption spectra obtained by subtracting the spectrum (b) from the spectra (c) and (d) shown in Fig. 3.8 are shown. The absorption peak at 525 nm, induced as a result of the LSP excitation around the Au NPs, is shifted by 17 nm toward a longer wavelength by the water. Assuming that the peak shift is caused by the fact that the refractive index around the Au NPs is really increased by the presence of water in the nanopores, the shift is compared with the theoretical value. The LSP excitation wavelength, λ_1, induced around Au NPs present in the surrounding medium with a refractive index n_1 is expressed by the following equation [1,2],

$$\lambda_1 = \lambda_p (\varepsilon^\infty + 2n_1^2)^{1/2}, \tag{3.5}$$

where λ_p and ε^∞ are the plasmon wavelength of bulk Au and the high-frequency dielectric constant of the NPs, respectively. While λ_p is 136.5 nm [23], n_1 can be regarded as the value of water, 1.377 [24], since the area of contact between each Au NP and the SiO_2 glass is small, although both water and SiO_2 glass are present around the Au NPs. Furthermore, ε^∞ is expressed as

$$\varepsilon^\infty = \lambda_2^2 / \lambda_p^2 - 2n_2^2, \tag{3.6}$$

where λ_2 and n_2 are the LSP excitation wavelength induced around the Au NPs and the refractive index of the surrounding medium before the dropping of water [1,2]. While λ_2 can be determined to be 525 nm from the spectrum (a) shown in Fig. 3.9, n_2 can be regarded as 1.0 by assuming that the Au NPs are uniformly surrounded by air, as in the case of the estimation of n_1, by neglecting the presence of SiO_2 glass. By using these values, ε^∞ is calculated to be 12.8, which is close to the value reported in the literature [1,3]. Then, the redshift in the LSP excitation wavelength, $\lambda_1 - \lambda_2$, induced by the embedding of water around the Au NPs can be calculated as 27 nm. This value and the value experimentally observed, 17 nm, should be regarded as close enough if the limits of the calculation accuracy are taken into account, which in turn indicates the validity of the above-mentioned

assumption. Namely, the redshift in the LSP excitation wavelength is induced as a result of the presence of water around the NPs. This demonstrates that a change in the medium surrounding the NPs can be detected by measuring the shift in the LSP excitation wavelength, which in turn means that the structure fabricated in this research can be applied to a plasmonic sensor, which should be useful in many fields such as biomolecular research.

3.4 Conclusions

Gold nanoparticles were three-dimensionally dispersed in nanopores formed on the surface of SiO_2 glass, and their plasmonic activity was investigated to examine the possibility of applying the structure to plasmonic devices. The following important results were obtained.

(i) At ion acceleration energies below 200 MeV, the radii of nanopores formed by ion implantation and subsequent perforation by etching become larger with an increase in the atomic number and acceleration energy of the ions.

(ii) With irradiation of 137-MeV Au ions and subsequent etching, nanopores with a high-aspect-ratio and diameters of approximately 50 nm can be formed on SiO_2 glass.

(iii) The localized surface plasmon excitation wavelength induced around the Au nanoparticles in nanopores shifts toward a longer wavelength by 17 nm, which agrees with the calculation result, when water is dropped on the surface. Thus, a change in the material around the Au nanoparticles can be detected, indicating that the present nanostructure is applicable to plasmonic sensors.

References for Chapter 3

[1] A. C. Templeton, J. J. Pietron, R. W. Murray, and P. Mulvaney, J. Phys. Chem. B **104**, 564 (2000).

[2] P. Mulvaney, Langmuir **12**, 788 (1996).

[3] T. Ung, L. M. Liz-Marzán, and P. Mulvaney, Colloids Surf. A: Physicochem. Eng. Aspects **202**, 119 (2002).

[4] S. H. Liu and M. Y. Han, Adv. Funct. Mater. **15**, 961 (2005).

[5] M. J. Ko, J. Plawsky, and M. Birnboim, J. Mater. Sci. Lett. **17**, 917 (1998).

[6] K. Awazu, M. Fujimaki, C. Rockstuhl, J. Tominaga, H. Murakami, Y. Ohki, N. Yoshida, and T. Watanabe, J. Am. Chem. Soc. **130**, 1676 (2008).

[7] C. Wang, C. Liu, Y. Liu, and Z. Zhang, Appl. Surf. Sci. **147**, 52 (1999).

[8] A. Meftah, F. Brisard, J. M. Costantini, M. Hage-Ali, J. P. Stoquert, F. Studer, and M. Toulemonde, Phys. Rev. B **48**, 920 (1993).

[9] M. Toulemonde, J. M. Costantini, C. Dufour, A. Meftah, E. Paumier, and F. Studer, Nucl. Instrum. Methods Phys. Res. B **116**, 37 (1996).

[10] K. Awazu, S. Ishii, K. Shima, S. Roorda, and J. L. Brebner, Phys. Rev. B **62**, 3689 (2000).

[11] V. A. Skuratov, D. L. Zagorski, A. E. Efimov, V. A. Kluev, Y. P. Toporov, and B. V. Mchedlishvili, Radiat. Meas. **34**, 571 (2001).

[12] K. Nomura, T. Nakanishi, Y. Nagasawa, Y. Ohki, K. Awazu, M. Fujimaki, N. Kobayashi, S. Ishii, and K. Shima, Phys. Rev. B **68**, 064106 (2003).

[13] K. Awazu, X. Wang, M. Fujimaki, T. Komatsubara, T. Ikeda, and Y. Ohki, J. Appl. Phys. **100**, 044308 (2006).

[14] M. Fujimaki, C. Rockstuhl, X. Wang, K. Awazu, J. Tominaga, T. Ikeda, Y. Ohki, and T. Komatsubara, Microelectron. Eng. **84**, 1685 (2007).

[15] J. Jensen, A. Razpet, M. Skupiński, and G. Possnert, Nucl. Instrum. Methods Phys. Res. B **243**, 119 (2006).

[16] Z. Dai, S. Yamamoto, K. Narumi, A. Miyashita, and H. Naramoto, Nucl. Instrum. Methods Phys. Res. B **149**, 108 (1999).

[17] A. Oliver, J. C. Cheang-Wong, J. Roiz, L. Rodriguez-Fernández, J. M. Hernández, A. Crespo-Sosa, and E. Muñoz, Nucl. Instrum. Methods Phys. Res. B **191**, 333 (2002).

[18] K. Awazu, X. Wang, M. Fujimaki, J. Tominaga, H. Aiba, Y. Ohki, and T. Komatsubara, Phys. Rev. B **78**, 054102 (2008).

[19] Z. G. Wang, C. Dufour, E. Paumier, and M. Toulemonde, J. Phys.: Condens. Matter **6**, 6733 (1994).

[20] M. P. R. Waligorski, R. N. Hamm, and R. Kats, Nucl. Tracks Radiat. Meas. **11**, 309 (1986).

[21] http://www.srim.org/SRIM/SRIM2006.htm

[22] G. Kumar, H. X. Tang, and J. Schroers, Nature **457**, 868 (2009).

[23] *Near-Field Optics and Surface Plasmon Polaritons*, edited by S. Kawata (Springer, Berlin, 2001).

[24] *Handbook of Optical Constants of Solids II*, edited by E. D. Palik (Academic Press, San Diego, CA, 1991).

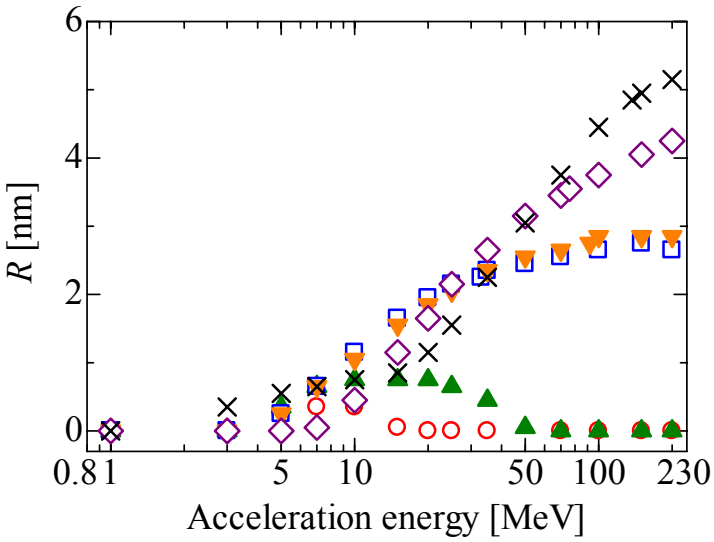

Fig. 3.1. The radius of the melted region R formed by the irradiation of a single ion into SiO_2 glass as a function of ion acceleration energy, calculated using heat diffusion equations (3.1)–(3.4). ○: Si (atomic number: 14), ▲: Cl (17), □: Se (34), ▼: Br (35), ◇: I (53), and ×: Au (79).

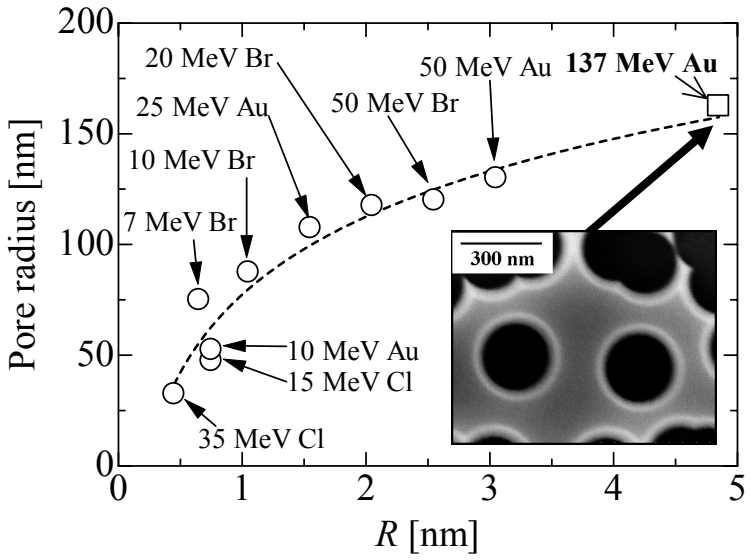

Fig. 3.2. The average radius of nanopores perforated in SiO_2 glass by wet etching after the implantation of various ions, as a function of the calculated radius of the melted region *R* shown in Fig. 3.1. Note that the open square represents the nanopore radius experimentally obtained for 137-MeV Au ions, while the open circles represent those reported in [15]. The broken line is a guide for the eyes. The inset shows a surface SEM image of the perforated sample A.

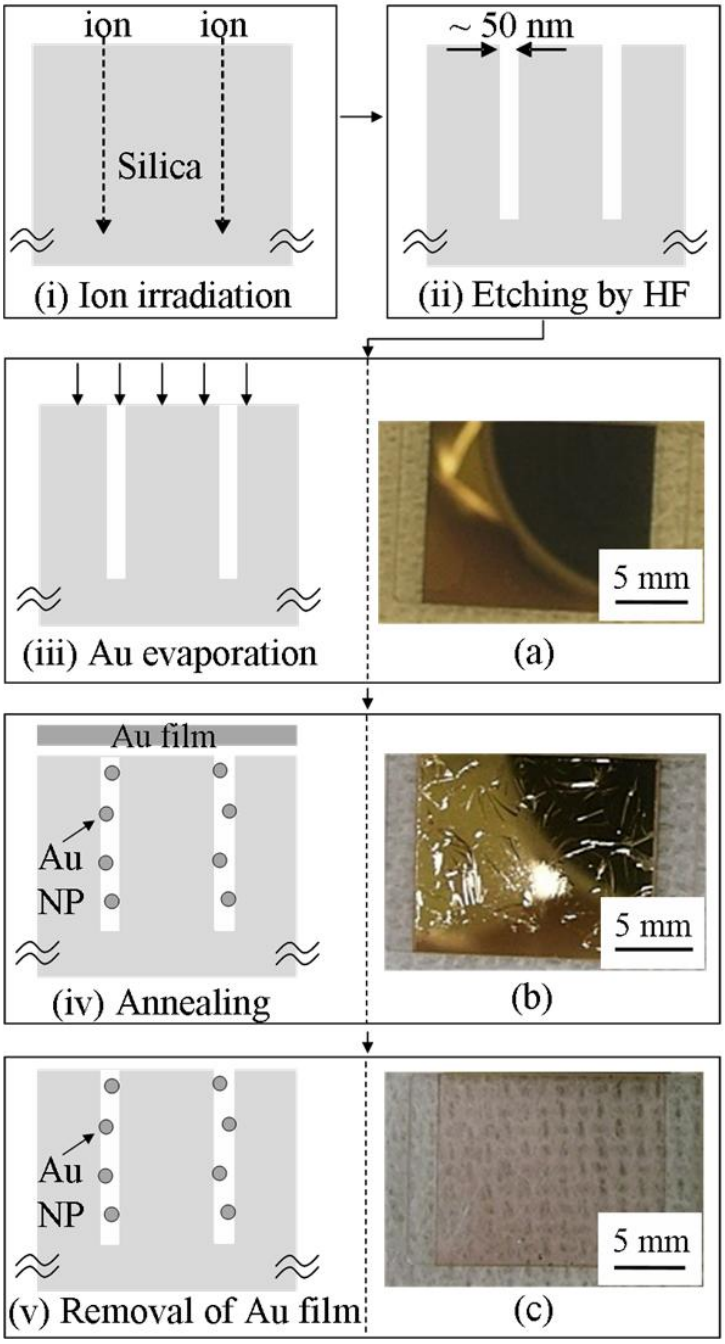

Fig. 3.3. Schematic procedures for the embedding of Au NPs into nanopores in a surface layer of SiO_2 glass: irradiation of 137-MeV Au ions to form latent tracks (i), etching of the latent tracks by hydrofluoric acid vapor to form nanopores (ii), evaporation of Au (iii), thermal treatment to remove the Au layer from the glass surface (iv), and the final structure (v). Photographs of sample C on a nonwoven cotton mesh taken at stages (iii)–(v) are shown in (a)–(c), respectively.

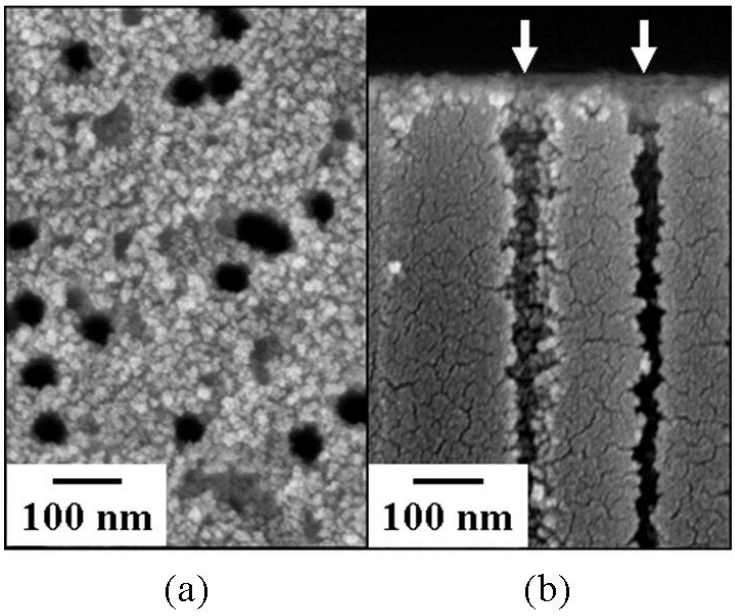

Fig. 3.4. Surface (a) and cross-sectional (b) SEM images of sample B after perforation by vapor etching. White arrows represent the direction of ion implantation.

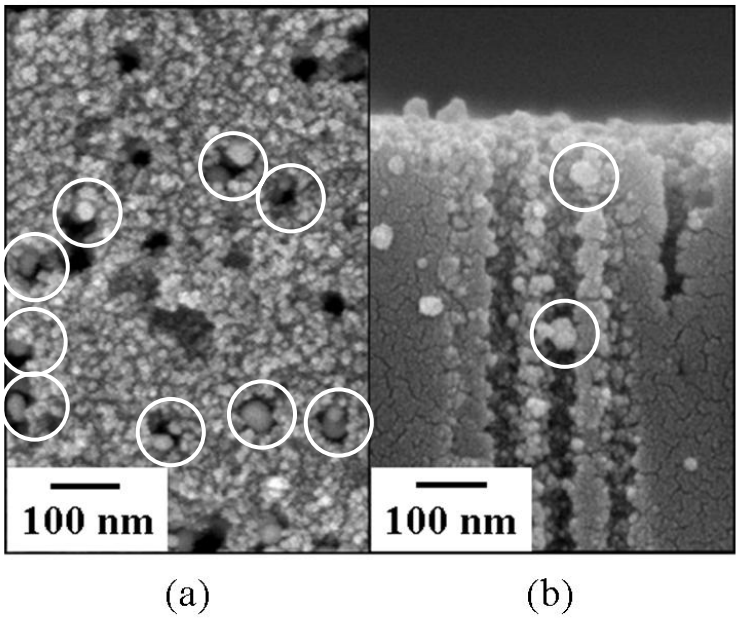

Fig. 3.5. Surface (a) and cross-sectional (b) SEM images of sample B, showing the presence of Au NPs embedded into the nanopores. White circles indicate the presence of Au NPs.

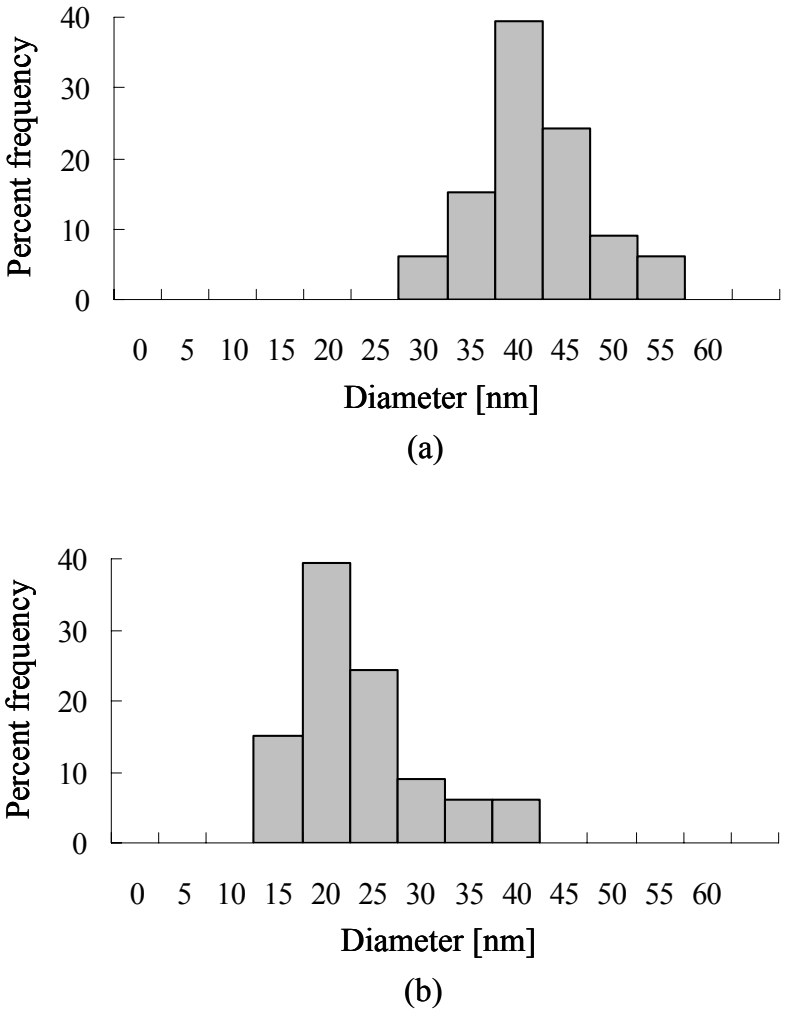

Fig. 3.6. Histograms of the diameters of the nanopores or black regions observed before (a) and after the Au NP embedment (b).

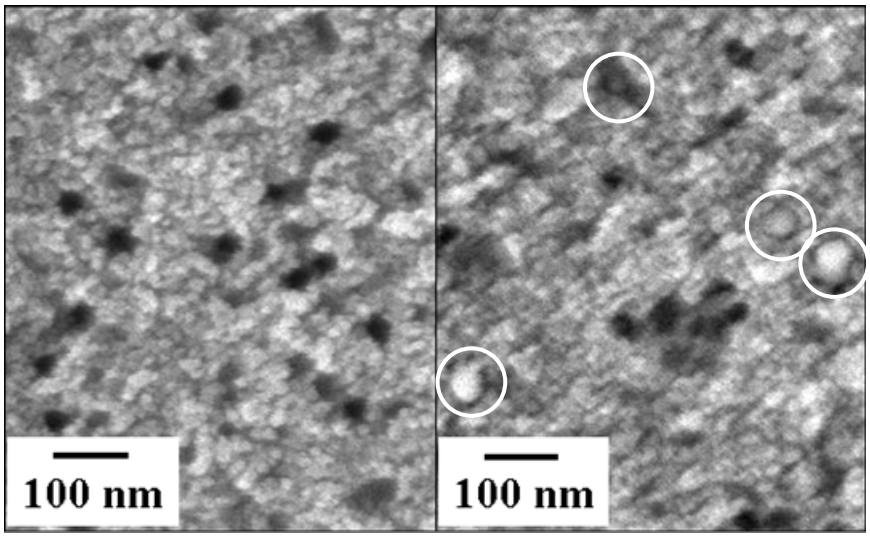

Fig. 3.7. Surface SEM images of perforated sample C taken before (a) and after the Au embedment (b). White circles in (b) indicate the presence of Au NPs.

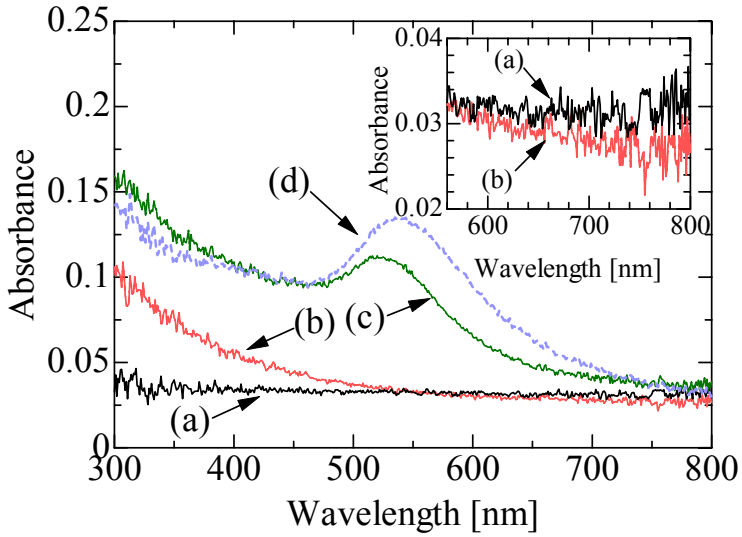

Fig. 3.8. Absorption spectra measured for sample C at the as-received stage (a), after the nanopore etching (b), after the embedment of Au NPs into the nanopores (c), and after introducing water into the nanopores with the Au NPs embedded (d). The inset shows the spectra (a) and (b) enlarged at wavelengths from 560 to 800 nm.

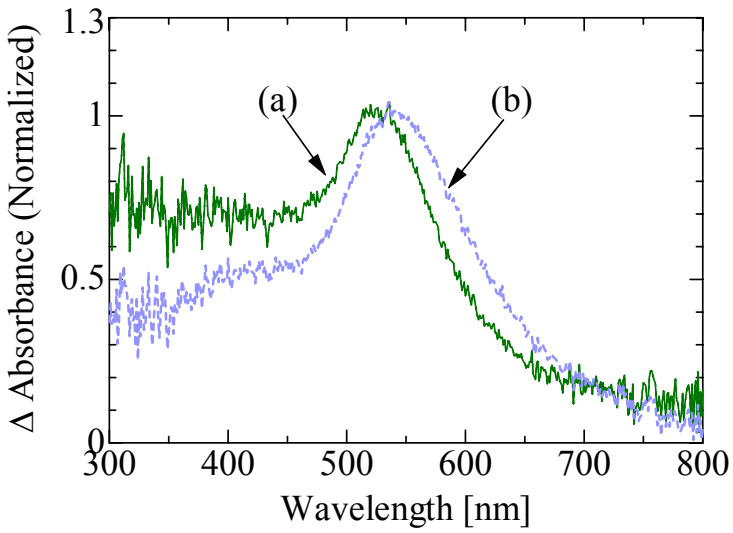

Fig. 3.9. Effect of water present around Au NPs on the absorption of sample C. Curves (a) and (b) are the normalized differential absorption spectra before and after the water was dropped, obtained by subtracting the spectrum (b) from the spectra (c) and (d) shown in Fig. 3.8, respectively.

–Chapter 4– Fabrication of Inert Ag Nanoparticles with a Thin SiO_2 Coating

Abstract

The author presents a genuine experimental technique to fabricate Ag nanoparticles with an ultrathin SiO_2 coating, thus making the nanoparticles chemically inert. The impact of the coating on plasmonic properties is experimentally quantified and compared with theoretical predictions. Furthermore, numerical simulations of the near-field enhancing properties of the nanoparticles are conducted. It is found that the coatings fabricated are sufficiently thin to make the plasmonic resonance wavelength shift negligible and for observing a significant field enhancement on the surface of the SiO_2 shell at the resonance wavelength. Application of such inert nanoparticles to sensitize the absorption of near-ultraviolet light is discussed.

4.1 Introduction

Metallic nanoparticles (NPs) with diameters in the order of only a few nm sustain fascinating electrical and optical properties that are not observable in their bulk counterparts [1,2]. Potentially the most appealing property is the possible excitation of localized surface plasmon (LSP) resonance. Research on LSP is mainly driven by the promise of numerous potential technological applications, such as for the localization of light in volumes much smaller than the diffraction limit [3], for Raman scattering spectroscopy [4], and many optical devices such as plasmonic waveguides [5], plasmonic photocatalysts [6], or biomolecular sensors [7].

Most of these applications rely on the significant scattering cross-section or the near-field amplitude largely enhanced in the close vicinity of the NP at the LSP resonance. Potentially the best metal for this purpose is Ag as it shows the lowest damping among the noble metals [8]. Nevertheless, its widespread use in devices is not encountered, because an intrinsic problem of Ag is its sensitive reaction with surrounding chemicals, causing easy oxidization of Ag and significant degradation of plasmonic properties. Therefore, there is a strong need to protect the Ag NP from its surrounding using an appropriate coating. Since SiO_2 is chemically inert and highly transparent over sufficiently large spectral domains, it is an attractive material for such protection. Therefore, the synthesis of SiO_2-coated Ag NPs by employing the Stöber method [9] or by depositing SiO_2 using ethyl alcohol [10] has been reported [10,11]. However, the SiO_2 coatings studied in these reports were much thicker than the diameter of the metallic NP. Because the electric field enhanced by the LSP excitation is localized to the surface between the metal and the dielectric with a roughly exponentially decaying strength in space, the near-field enhancing qualities of coated NPs in these papers could not be used as it fades away for coatings that are excessively thick. To address this limitation, the author introduces and details here a genuine experimental technique to fabricate Ag NPs with protecting SiO_2 coatings having a thickness of approximately 5 nm or even less. The

author presents the experimental results of the absorption spectra of such NPs and analyzes the impact of the coating on plasmonic properties observable in the far- and near-field.

4.2 Experimental Procedures

The SiO_2-coated Ag NPs were obtained by the following methods. First, a 100-mL aqueous solution of 0.1-mM $AgNO_3$ containing 2.6 mg of trisodium citrate as a stabilizer was prepared. Second, into the solution, which was being stirred vigorously, a 10-mL aqueous solution of 2-mM $NaBH_4$ used as a reducing agent of Ag ions was poured gently and slowly. The procedure makes it possible to fabricate Ag NPs with a mean diameter of ≈10 nm at low size dispersion. This solution, in which the Ag NPs are homogenously dispersed, is termed throughout the manuscript "Ag sol". Next, the deposition of thin and homogenous SiO_2 films on the NPs dispersed in the Ag sol was performed with the following procedures. A 0.4-mL aqueous solution of 1-mM 3-aminopropyl-trimethoxysilane used as a coupling agent was added to the Ag sol. It was then stirred vigorously for 20 min. The sol was subsequently diluted by a factor of 10 with distilled water. In the next step, 5 mL of a 0.54-wt% sodium silicate solution was poured into the slowly stirred diluted sol within five hours, followed by gentle stirring for two days. Next, the sol was concentrated 10 times using a rotary evaporator, followed by a single dialysis using a dialytic film with a pore size of 5 nm. After the dialysis, the sol was concentrated by a factor of four. Finally, analytical grade ethyl alcohol, four times as much as the sol, was slowly added, resulting in the deposition of thin SiO_2 films on the surfaces of Ag NPs. The solution at this stage, in which the SiO_2-coated Ag NPs are dispersed, is referred to as "SiO_2-coated Ag sol". The SiO_2-coated Ag NPs were then collected on a Cu microgrid coated with carbon. Their shapes were observed using TEM (Hitachi H-9000). The LSP excitation wavelength was measured by observing the absorption spectrum with a Hitachi U-4100 ultraviolet-visible-near infrared spectrophotometer.

4.3 Results and Discussion

Figure 4.1 shows a TEM image of the synthesized Ag NPs coated with the thin SiO_2 films. It is clearly shown that Ag NPs with an average diameter of 7 nm are covered with a SiO_2 coating 3 nm thick on average. They form a string of beads, which is adequate for the efficient use of the enhanced electric field induced by the LSP excitation.

Absorption spectra of the Ag sol and the SiO_2-coated Ag sol are shown in Fig. 4.2. The absorption peak, induced by the excitation of LSP resonance, shifts toward a longer wavelength by 5 nm for the SiO_2-coated Ag NPs. The shift can be generally explained by considering that the SiO_2 coating increases the refractive index of the surrounding. A theoretical analysis was carried out at this stage of the research. The peak wavelength λ_{p1} of the LSP excited in a metallic NP with a spherical core (metal)–shell (dielectric) structure can be computed by [12]

$$\lambda_{p1} = \lambda_{p2}\left[\varepsilon^{\infty} + \frac{2n_s{}^2\left[n_s{}^2 g + n_{m1}{}^2(3-g)\right]}{n_s{}^2(3-2g) + 2n_{m1}{}^2 g}\right]^{1/2}, \tag{4.1}$$

where λ_{p2}, ε^{∞}, n_s, n_{m1}, and g are the bulk metal plasmon wavelength, high-frequency dielectric constant, refractive index of the film, refractive index of the medium surrounding the core–shell structure, and volume fraction of the shell layer, respectively. For Ag, λ_{p2} is 136.3 nm [13], and n_s is calculated to be 1.42 from the relation between the density and the refractive index of SiO_2 [14]. The density of SiO_2 deposited in the present experiment was assumed to be 2.0 g/cm^3 [15,16]. From the literature [17,18], n_{m1}, which corresponds to the refractive index of a mixture of ethyl alcohol and water with a volume ratio of 4 : 1, is estimated to be 1.368. The fraction g is described using the equation,

$$g = \frac{(R_c + T_s)^3 - R_c{}^3}{(R_c + T_s)^3}, \tag{4.2}$$

where R_c and T_s are the radius of the metallic NP and the thickness of the surrounding film, respectively. Furthermore, ε^{∞} is expressed using the equation [12,19],

$$\varepsilon^{\infty} = (\lambda_{p3}/\lambda_{p2})^2 - 2n_{m2}{}^2, \tag{4.3}$$

where λ_{p3} is the LSP excitation wavelength for the Ag NPs in the Ag sol, and n_{m2} is the refractive index of water surrounding the Ag NP, being 1.350 [17]. From the solid curve shown in Fig. 4.2, λ_{p3} is experimentally determined to be 395 nm. Therefore, by substituting 395 nm to λ_{p3} in Eq. (4.3), ε^{∞} is obtained to be 4.75. This is in a good agreement with the values reported in the literature [19]. Using these values, the shift in the LSP excitation wavelength induced by the SiO_2 coating $\lambda_{p1} - \lambda_{p3}$ is estimated to be 7.9 nm for the SiO_2-coated Ag NPs if R_c = 3.5 nm and T_s = 3.0 nm. This is close to the shift value observed, which was 5 nm. Thus, it is concluded that the SiO_2 coating is thin enough not to give any harmful effect on the plasmonic activity. The above-mentioned SiO_2-coated Ag NPs can be used as a sensitizer in the near-ultraviolet region.

Furthermore, the enhancement of the electric field in the vicinity of the SiO_2-coated Ag NP induced by the LSP was calculated using the Mie theory [20]. Figure 4.3(a) shows the field enhancement in a cross section of the NP. The enhancement is defined as the electric field intensity normalized to the intensity of the incident wave. The incident wave is assumed to be an x-polarized plane wave propagating in the positive z-direction and having a wavelength of 400 nm. The wavelength was chosen because it corresponds to the LSP resonance as deduced from Fig. 4.2. All the experimental parameters for the Ag–SiO_2 core–shell spherical NP as detailed before were taken into account. The refractive index of Ag at a wavelength of 400 nm was assumed to be 0.226 + 2.10i. The value is slightly different from the refractive index of the bulk Ag [8], since the finite size effects of the NP are fully taken into account [20]. Figure 4.3(b) shows change in the ratio of the field intensity along the x axis. As shown in Fig. 4.3(b), the electric field intensity on the surface of

the SiO_2 coating is enhanced by a factor of 1.8. This indicates that the electric field remains enhanced on the surface of the SiO_2 shell. Stronger electric field enhancement can be obtained for a larger Ag NP, since higher plasmonic activity and a longer penetration length are realized with an increase in the radius of the NP.

4.4 Conclusions

Synthesis of Ag nanoparticles with an average diameter of 7 nm coated with thin SiO_2 films with an average thickness of 3 nm has been successfully carried out by a chemical reaction in a liquid. The redshift of the localized surface plasmon resonance wavelength due to the SiO_2 coating was measured to be 5 nm, resulting in only a subtle change in the plasmonic activity in the near-ultraviolet region. The redshift observed agrees very well with the calculated. Numerical simulation showed that the electric field intensity on the surface of the Ag–SiO_2 core–shell spherical nanoparticle is enhanced at the localized surface plasmon excitation wavelength by a factor of 1.8. This field enhancement should bring about a higher performance of an optical device that utilizes the resonance absorption enhanced in the near-ultraviolet region.

References for Chapter 4

[1] P. V. Kamat, J. Phys. Chem. B **106**, 7729 (2002).

[2] S. Link and M. A. El-Sayed, J. Phys. Chem. B **103**, 8410 (1999).

[3] T. Tanaka, K. Yamaguchi, and S. Yamamoto, Opt. Commun. **212**, 45 (2002).

[4] N. Hayazawa, Y. Inouye, Z. Sekkat, and S. Kawata, Opt. Commun. **183**, 333 (2000).

[5] S. A. Maier, P. G. Kik, H. A. Atwater, S. Meltzer, E. Harel, B. E. Koel, and A. A. G. Requicha, Nat. Mater. **2**, 229 (2003).

[6] K. Awazu, M. Fujimaki, C. Rockstuhl, J. Tominaga, H. Murakami, Y. Ohki, N. Yoshida, and T. Watanabe, J. Am. Chem. Soc. **130**, 1676 (2008).

[7] K. Mitsui, Y. Handa, and K. Kajikawa, Appl. Phys. Lett. **85**, 4231 (2004).

[8] P. B. Johnson and R. W. Christy, Phys. Rev. B **6**, 4370 (1972).

[9] W. Stöber, A. Fink, and E. Bohn, J. Colloid Interface Sci. **26**, 62 (1968).

[10] T. Ung, L. M. Liz-Marzán, and P. Mulvaney, Langmuir **14**, 3740 (1998).

[11] C. Graf, D. L. J. Vossen, A. Imhof, and A. van Blaaderen, Langmuir **19**, 6693 (2003).

[12] A. C. Templeton, J. J. Pietron, R. W. Murray, and P. Mulvaney, J. Phys. Chem. B **104**, 564 (2000).

[13] T. Hirakawa and P. V. Kamat, J. Am. Chem. Soc. **127**, 3928 (2005).

[14] B. Marler, Phys. Chem. Miner. **16**, 286 (1988).

[15] A. van Blaaderen and A. P. M. Kentgens, J. Non-Cryst. Solids **149**, 161 (1992).

[16] J. J. Penninkhof, T. van Dillen, S. Roorda, C. Graf, A. van Blaaderen, A. M. Vredenberg, and A. Polman, Nucl. Instrum. Methods Phys. Res. B **242**, 523 (2006).

[17] *Handbook of Optical Constants of Solids II*, edited by E. D. Palik (Academic Press, San Diego, CA, 1991).

[18] *Kagaku Binran Kisohen (Handbook of Chemistry)*, edited by The Chemical Society of Japan (Maruzen, Tokyo, 1984) [in Japanese].

[19] P. Mulvaney, Langmuir **12**, 788 (1996).

[20] *Near-Field Optics and Surface Plasmon Polaritons*, edited by S. Kawata (Springer, Berlin, 2001).

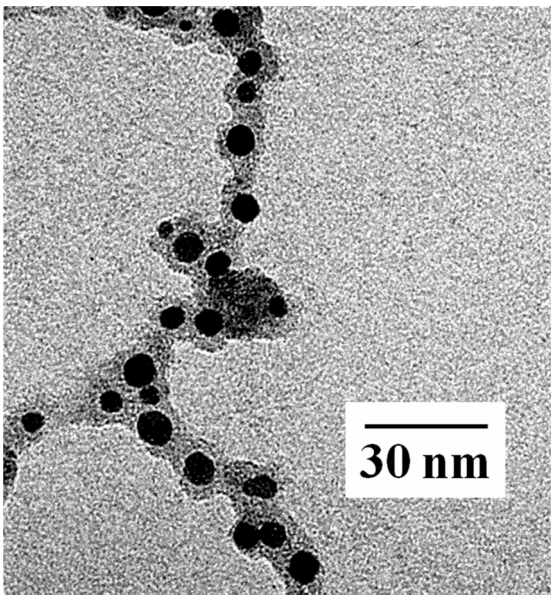

Fig. 4.1. Transmission electron microscopy image of the synthesized Ag NPs coated with thin SiO_2 film.

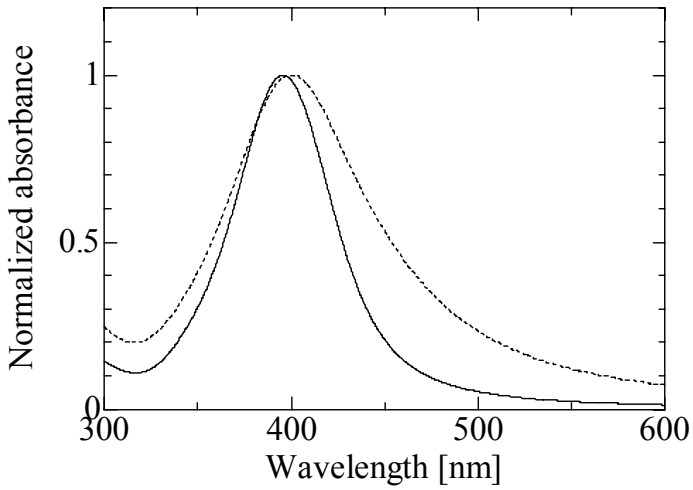

Fig. 4.2. Absorption spectra of the Ag sol (solid curve) and the SiO_2-coated Ag sol (broken curve).

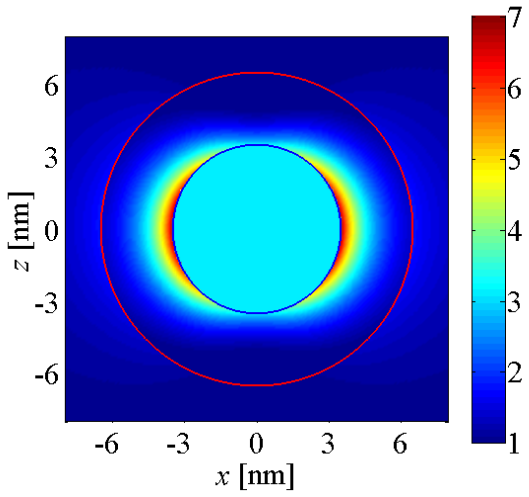

(a)

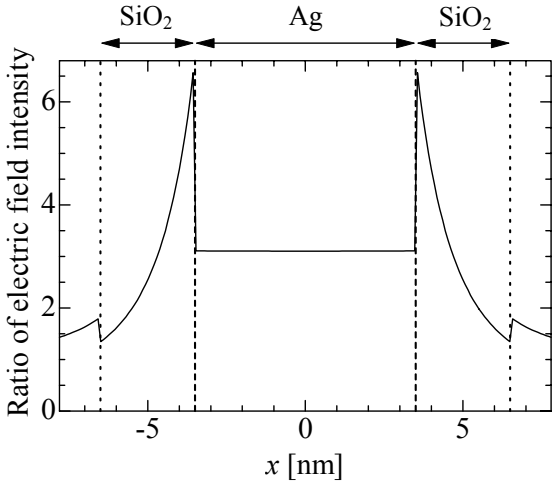

(b)

Fig. 4.3. (a) Electric field intensity in the vicinity of a Ag core centered at the origin with a diameter of 7 nm covered with a 3-nm-thick SiO_2 shell, calculated using the Mie theory. The core–shell particle in a mixture of ethyl alcohol and water with a volume ratio of 4 : 1 is exposed to plane-wave light with a wavelength of 400 nm. The color bar indicates the ratio of the electric field intensity against that of the incident light. (b) Change in the ratio along the *x* axis or the diameter of the NP.

–Chapter 5– Solution Conductivity as a Key Factor for Thin SiO_2 Coating on Colloidal Ag

Abstract

In order to utilize Ag nanoparticles for various applications such as photocatalysts while maintaining their chemical stability, enhanced electric fields on the nanoparticle surfaces induced by localized surface plasmon excitation must be used effectively. For satisfying these requirements, an ultrathin SiO_2 coating with a thickness of only a few nm was formed around Ag nanoparticles by a chemical reaction in a solution, while parameters such as the amount of sodium silicate and the number of dialysis procedures performed were changed. As a result, it was found that a key factor for obtaining stable thin-SiO_2-coated Ag nanoparticles is the conductivity of the solution. Using a solution with an appropriate conductivity above 2.7 mS/m, SiO_2 films can be coated on Ag nanoparticles without causing deterioration of the plasmonic activity resulting from the aggregation of Ag.

5.1 Introduction

As a source of future photonic technology, the new research field of "plasmonics" has attracted much attention. Among the many phenomena in plasmonics, the enhancement of an electric field by localized surface plasmon (LSP) excitation occurring in metallic nanoparticles (NPs), which has various applications [1–4], is one of the most fascinating. Silver (Ag) NPs are particularly suitable for applications that utilize near-ultraviolet light, such as photocatalysts, since the excitation wavelength of these NPs is in the near-ultraviolet wavelength region. Silver NPs are also attractive in that strong electric fields can be expected since Ag has the lowest damping constant of the commonly used noble metals [5].

Silicon dioxide (SiO_2) is very attractive as a material for protective films that prevent the deterioration of Ag NPs, since it is chemically inert and highly transparent in a wide range from the near-infrared to the near-ultraviolet wavelength. Two SiO_2 coating methods are possible, namely direct deposition by a method such as sputtering on Ag NPs located on a substrate and chemical deposition on NPs in solution. Such physical methods are relatively simple and are widely used [2]. However, in the first method, the film thickness deposited tends to be nonuniform since the deposition occurs by an inherently one-dimensional method on Ag NPs scattered on the substrate. However, with the use of chemical synthesis in a solution, homogenous SiO_2 films can be deposited on Ag NPs. Therefore, the fabrication of Ag NPs and the coating of them with SiO_2, both carried out by chemical synthesis in appropriate solutions, have been reported [6–8].

Once Ag NPs are coated with SiO_2 films, the electric field enhancement can be utilized only in the region beyond the surface of the protective film. The enhancement is the largest on the NP surface, and decreases markedly in the form of r^{-3}, where r is the distance from the center of the NP [9]. Therefore, a thin SiO_2 film is desirable in order to utilize the electric field enhancement effectively.

However, in most studies reported previously [6–8], the thicknesses of SiO_2 films obtained are greater than the diameters of respective Ag NPs.

In order to address this limitation, Ag NPs were coated with thin SiO_2 films by chemical synthesis in a solution, and ultrathin SiO_2 coatings with an average thickness of 3 nm were formed successfully around extremely small Ag NPs with an average diameter of 7 nm [10]. Realizing this structure without causing aggregation of Ag NPs during synthesis is of prime importance in order to utilize the stable plasmonic activity of Ag NPs for a long period. For the formation of SiO_2 coating, the ion concentration in a solution is expected to be a key factor. However, to the authors' knowledge, there are few papers reporting the effect of ion concentration on the formation of a SiO_2 coating on Ag NPs. In the present research, the ion concentration changed by dialysis was evaluated by measuring the conductivity of the solution, and the condition for achieving a stable SiO_2 coating on Ag NPs was obtained. The appropriate condition for the injection of the silane coupling agent, which is essential to deposit SiO_2 on Ag NPs, is also discussed.

5.2 Experimental Procedures

Silver NPs were fabricated by slowly adding a 10-mL aqueous solution of 2-mM $NaBH_4$ (Aldrich) used as a reducing agent into a vigorously stirred 100-mL aqueous solution of 0.1-mM $AgNO_3$ (Kanto Chemical) and 0.1-mM trisodium citrate anhydrous (Wako Pure Chemical Industries) over a period of four hours. The LSP excitation wavelength of the Ag NPs dispersed in the sol was 395 nm [10]. The Ag NPs do not aggregate because of the electrostatic repulsion resulting from negatively charged citrate surrounding the Ag NPs [6,11]. Next, an aqueous solution of 1-mM 3-aminopropyl-trimethoxysilane (APS; Aldrich) used as a silane coupling agent was added into the Ag sol, and the negatively charged citrate around the NPs is assumed to be replaced with APS immediately [6,11]. Since siloxy groups in APS align facing the surrounding medium [6,11], SiO_2 is deposited on the Ag NPs. An aqueous solution containing 27-wt% sodium silicate (Aldrich) was used as the material for the SiO_2 coating. Distilled water was used for the aqueous solution and for dialysis, and cellulose dialytic films with a pore size of 5 nm (Sanko Junyaku) were used for dialysis.

In order to measure the LSP excitation wavelength of the Ag NPs, absorption spectra were obtained using a Hitachi U-4100 spectrophotometer. The solution conductivity and pH were measured at room temperature using a Mettler Toledo SevenMulti meter, which indicates the conductivity and pH of a solution at 25 °C by converting the corresponding values measured at an arbitrary temperature between 0 and 100 °C.

5.3 Results and Discussion

Figure 5.1(a) shows absorption spectra of the Ag-NP-containing solution into which aqueous solutions of 1-mM APS were added with total volumes of 0.2, 0.4, and 0.8 mL, together with the

spectrum before the addition of the APS solutions. No clear spectral changes are observed upon the addition of 0.2 mL, while a slight increase in absorbance at wavelengths longer than 450 nm is observed upon the addition of 0.4 mL or more. This increase in absorbance is considered to result from enlargement of the size of Ag NPs [12,13] by aggregation.

Figure 5.1(b) shows a sketch detailing the adhesion of APS to metal NPs [6,11]. It is known that the unprotonated amino group of each APS molecule attaches to the surface of a metal NP via a dative bond [6,11]. Furthermore, it is assumed that all three methoxy groups at the other end of the APS molecule are hydrolyzed to form three oxygen negative ions, since the pH of the solution is ~7.5, which is sufficiently high to cause complete ionization [6]. One APS molecule can cover 4.0×10^{-19} m^2 of the surface of Ag NPs [6] or Au NPs [11] dispersed in a solution. It has been reported, for Au NPs in a solution, that a bridging flocculation of APS occurs over a period of minutes to days, if the amount of APS solution added exceeds the amount that is necessary to cover all the surfaces of NPs or to make monolayered APS on NPs [11]. Assuming that a similar phenomenon occurs in the present experiment, the number of APS layers that is expected to cover the Ag NPs was calculated [11]. If all of the Ag NPs dispersed in the solution are spherical with identical radii R (m), their total surface area S (m^2) is expressed as

$$S = 4\pi R^2 Nx = 3(4/3\pi R^3 N)x / R = 3<\mathrm{Ag}>Vx / R, \quad (5.1)$$

where N ($1/m^3$), x (m^3), <Ag> (mol/m^3), and V (m^3/mol) are the number of the Ag NPs per unit volume, the volume of the solution, the molar concentration of Ag in the solution, and the molar volume of Ag, respectively. For Ag, V is 1.0×10^{-5} m^3/mol, while R is found to be 3.5×10^{-9} m from the TEM image reported in [10]. As mentioned above, <Ag> and x are 0.1 mol/m^3 and 1.0×10^{-4} m^3, respectively.

Using the above values, S is calculated to be 8.6×10^{-2} m^2. Assuming that all the APS molecules are attached to the Ag NPs, the number of layers of APS attached to the NPs corresponds to 2.2 for 0.8 mL of the APS solution. As mentioned in relation to Fig. 5.1(a), significant aggregation was induced by the addition of 0.8 mL of the APS solution. In the same way, all the surfaces of the Ag NPs should be covered by approximately one layer of APS when the amount of APS solution added is 0.4 mL. Although the basic assumption is developed for Au [11], as mentioned above, the increase in absorbance shown in Fig. 5.1(a) agrees well with the assumption that bridging flocculation occurs when APS solution is added in excess of the amount required, causing the formation of the monolayer coating. Therefore, adding 0.4 mL of the APS solution is appropriate to coat the total surface area, 8.6×10^{-2} m^2, of the Ag NPs.

Next, three Ag colloidal solutions, into which 0.4 mL of the APS solution had been added, were prepared. These solutions were diluted with 900 mL of water in order to prevent the aggregation of NPs by separating NPs from each other. Then, 2, 5, and 10 mL of 0.54-wt% sodium silicate solution were slowly added into the three diluted solutions within five hours. According to the volumes added,

the solutions with sodium silicate are referred to as S2, S5, and S10, and the solution before the addition of sodium silicate is referred to as S0. Figures 5.2(a) and (b) show absorption spectra of solutions S0, S2, S5, and S10, and their peak positions, respectively. The peaks shift toward a longer wavelength with an increase in sodium silicate. The redshift seen in Fig. 5.2(b) confirms that SiO_2 with a refractive index higher than that of water is formed on the Ag NPs [14].

Then, solutions S2, S5, and S10 were concentrated by a factor of 10 using a rotary evaporator, in order that the SiO_2-coated Ag NPs could be arranged with a higher density on substrates. The concentrated solutions are referred to as $S2_0$, $S5_0$, and $S10_0$. The solutions were dialyzed to remove excess ions, which prevents their precipitation in the form of a crystallized salt on the substrates. The solutions dialyzed once are referred to as $S2_1$, $S5_1$, and $S10_1$, and those dialyzed twice are referred to as $S2_2$, $S5_2$, and $S10_2$.

Figures 5.3(a) and (b) show absorption spectra of solutions $S2_1$, $S5_1$, and $S10_1$, and those of solutions $S2_2$, $S5_2$, and $S10_2$, respectively. For solution $S2_1$, a significant increase in absorbance at wavelengths longer than 420 nm is observed, which indicates the formation of larger Ag NPs [12,13] by aggregation. As shown in Fig. 5.3(b), the absorption peak at around 400 nm disappears in all three solutions after the second dialysis, which indicates that the Ag NPs aggregated further to form bulk metal.

The conductivity was measured for all the solutions to estimate the number of ions present. Figure 5.4 shows the conductivity converted to the value at 25 °C by the conductivity meter. The decrease in conductivity upon dialysis indicates that the number of ions in the solutions decreased. Solution $S2_1$ has the lowest conductivity of the three solutions after the first dialysis. Furthermore, all the solutions after the second dialysis have very low conductivity. These results indicate that there is a strong relationship between the solution conductivity and the aggregation of the Ag NPs. Namely, the adjustment of the ion concentration in the solution is important to avoid the aggregation of Ag NPs. A possible cause of the aggregation is the decrease in the number of ions, such as citrate ions, surrounding the NPs. It is known that Ag NPs dispersed in a solution containing sodium citrate are complexed with negatively charged citrate, and that no aggregation occurs because of electrostatic repulsion [6,11]. Furthermore, it has been reported that the ζ potential of SiO_2 NPs dispersed in a solution containing citric acid is negative [15], which indicates that, as in the case of the Ag NPs, the SiO_2 NPs form complexes with the negatively charged citrate. Therefore, after the Ag NPs were coated with SiO_2, the SiO_2 is expected to be surrounded by negatively charged citrate, which induces electrostatic repulsion. Therefore, aggregation of the SiO_2-coated Ag NPs can be avoided. This, in turn, indicates that the aggregation of the Ag NPs observed in the present experiment is caused by a significant decrease in the amount of negatively charged citrate around the SiO_2-coated Ag NPs. The results shown in Figs. 5.3(a), 5.3(b), and 5.4 indicate that the conductivity of solution $S5_1$, 2.7 mS/m, is the minimum conductivity that can prevent the aggregation of the Ag NPs.

In view of the objective of the present research to form a stable thin SiO_2 coating, solution $S5_1$ is the most suitable, since the aggregation of the Ag NPs is observed in solution $S2_1$, and the amount of sodium silicate is lower in $S5_1$ than in $S10_1$. By using solution $S5_1$, Ag NPs with an average diameter of 7 nm coated with extremely thin SiO_2 coatings with an average thickness of 3 nm, which exhibit an electric field enhancement factor of 1.8 on the SiO_2 surfaces, can be fabricated [10]. Such an extremely thin SiO_2 coating cannot be realized by a physical fabrication method. Furthermore, thicker SiO_2 coatings should be formed on Ag NPs with $S10_1$, the solution conductivity of which is higher than that of $S5_1$. Thus, the monitoring and adjustment of the solution conductivity is of prime importance for the control of the thickness of a SiO_2 coating as well as for the prevention of the aggregation of Ag.

5.4 Conclusions

The fabrication of Ag nanoparticles with a thin SiO_2 coating was conducted by chemical synthesis. It was determined that (i) an excessive decrease in solution conductivity owing to excess dialysis induces the aggregation of Ag. Namely, the decrease in ions, such as citrate ions, surrounding the nanoparticles should reduce electrostatic repulsion, causing aggregation of SiO_2-coated Ag nanoparticles and (ii) the solution conductivity is a key factor for obtaining SiO_2-coated Ag nanoparticles with an appropriate SiO_2 thickness, whereby the aggregation of Ag can be prevented and the plasmonic activity can be utilized effectively.

References for Chapter 5

[1] S. Nie and S. R. Emory, Science **275**, 1102 (1997).

[2] K. Awazu, M. Fujimaki, C. Rockstuhl, J. Tominaga, H. Murakami, Y. Ohki, N. Yoshida, and T. Watanabe, J. Am. Chem. Soc. **130**, 1676 (2008).

[3] T. Akiyama, T. Kawahara, T. Arakawa, and S. Yamada, Jpn. J. Appl. Phys. **47**, 3063 (2008).

[4] S. Kühn, U. Håkanson, L. Rogobete, and V. Sandoghdar, Phys. Rev. Lett. **97**, 017402 (2006).

[5] P. B. Johnson and R. W. Christy, Phys. Rev. B **6**, 4370 (1972).

[6] T. Ung, L. M. Liz-Marzán, and P. Mulvaney, Langmuir **14**, 3740 (1998).

[7] Y. Kobayashi, H. Katakami, E. Mine, D. Nagao, M. Konno, and L. M. Liz-Marzán, J. Colloid Interface Sci. **283**, 392 (2005).

[8] C. Graf, D. L. J. Vossen, A. Imhof, and A. van Blaaderen, Langmuir **19**, 6693 (2003).

[9] *Metal Nanoparticles: Synthesis, Characterization, and Applications*, edited by D. L. Feldheim and C. A. Foss (Marcel Dekker, New York, NY, 2002).

[10] K. Nomura, S. Fujii, Y. Ohki, K. Awazu, M. Fujimaki, J. Tominaga, N. Fukuda, T. Hirakawa, and C. Rockstuhl, Jpn. J. Appl. Phys. **47**, 8641 (2008).

[11] L. M. Liz-Marzán, M. Giersig, and P. Mulvaney, Langmuir **12**, 4329 (1996).

[12] J. J. Mock, M. Barbic, D. R. Smith, D. A. Schultz, and S. Schultz, J. Chem. Phys. **116**, 6755 (2002).

[13] J. Tiggesbäumker, L. Köller, K. H. Meiwes-Broer, and A. Liebsch, Phys. Rev. A **48**, R1749 (1993).

[14] A. C. Templeton, J. J. Pietron, R. W. Murray, and P. Mulvaney, J. Phys. Chem. B **104**, 564 (2000).

[15] Y. K. Hong, D. H. Eom, S. H. Lee, T. G. Kim, J. G. Park, and A. A. Busnaina, J. Electrochem. Soc. **151**, G756 (2004).

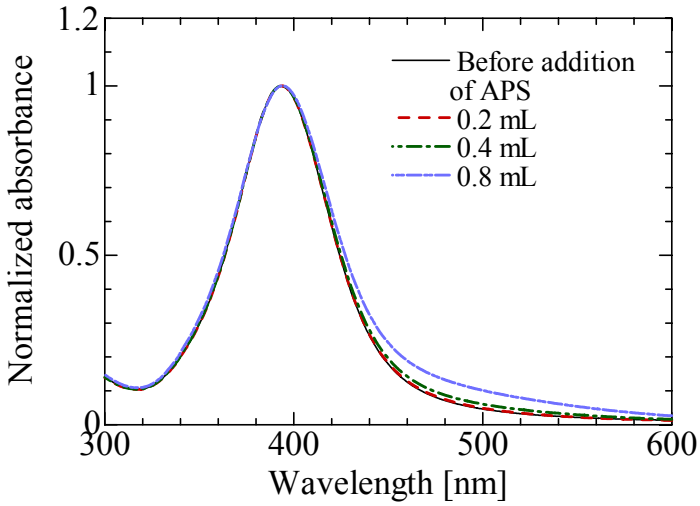

(a)

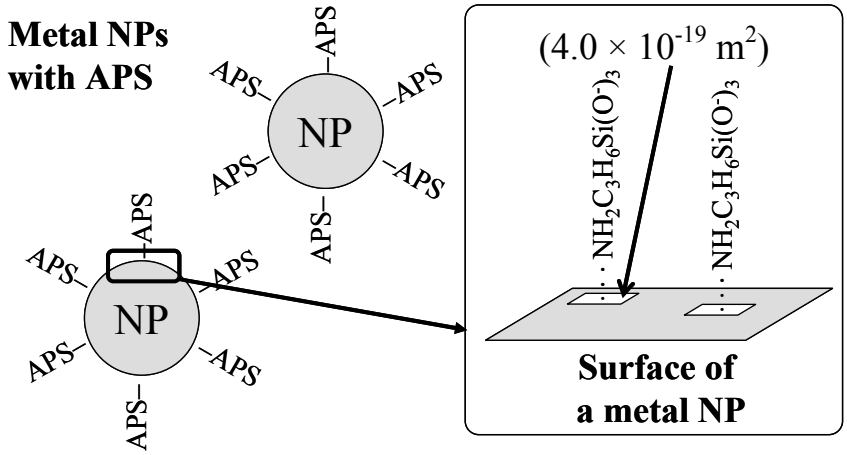

(b)

Fig. 5.1. (a) Absorption spectra of the solution before and after the addition of aqueous solutions of 1-mM APS with total volumes of 0.2, 0.4, and 0.8 mL. (b) A sketch showing an adhesion model of APS molecules on NPs.

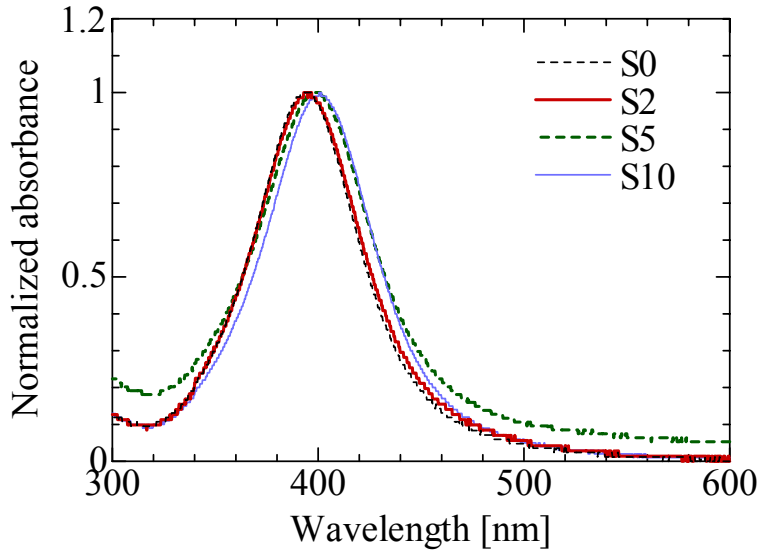

(a)

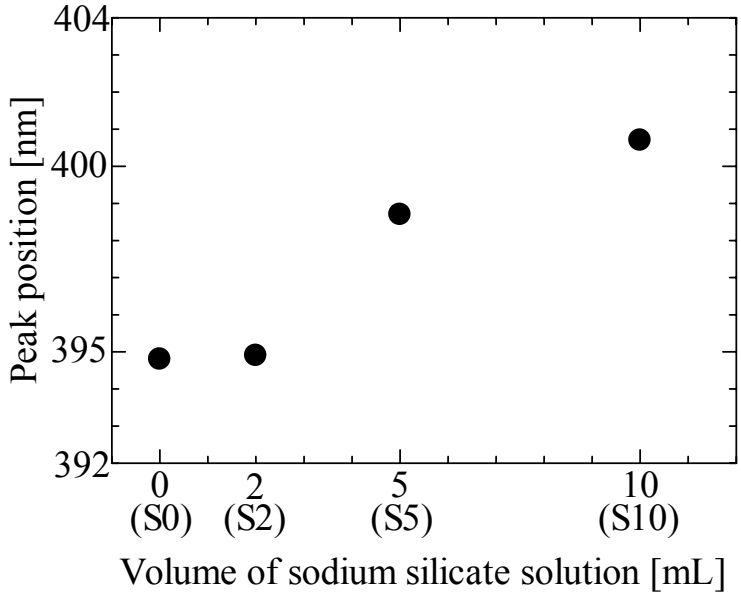

(b)

Fig. 5.2. (a) Absorption spectra of the solutions before (S0) and after the addition of 0.54-wt% sodium silicate solutions with volumes of 2 mL (S2), 5 mL (S5), and 10 mL (S10). (b) The peak positions of the spectra shown in (a).

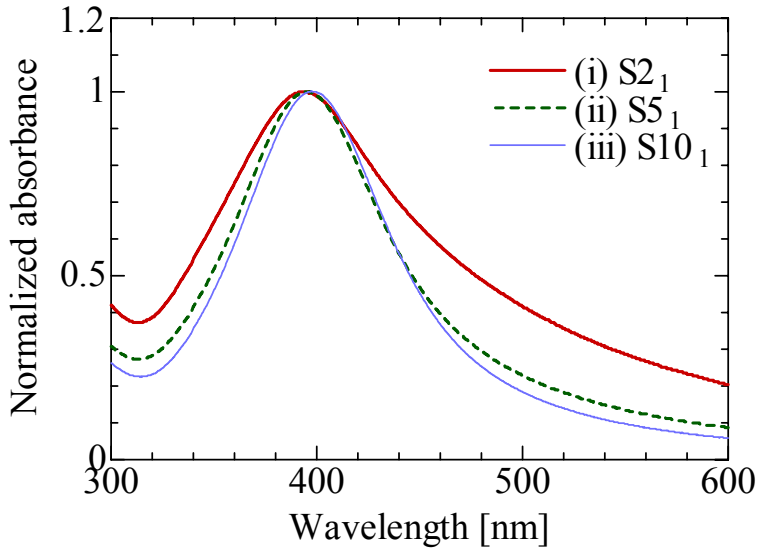

(a)

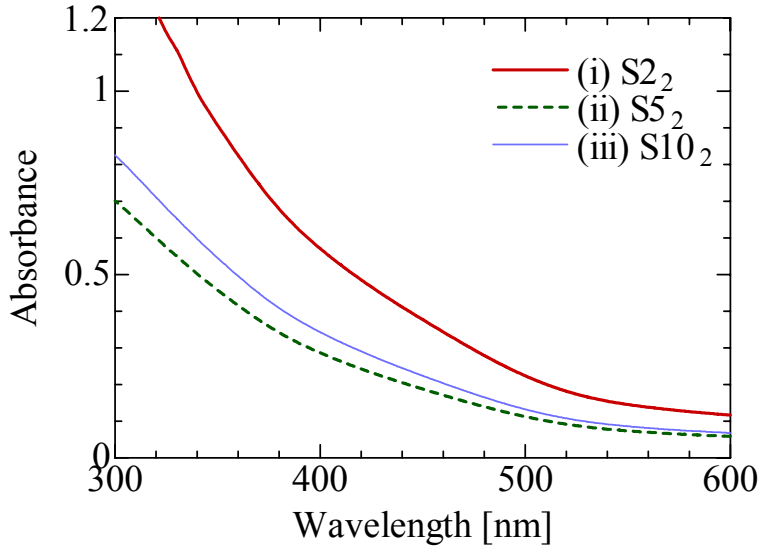

(b)

Fig. 5.3. Absorption spectra of the solutions obtained after the first dialysis (a) and the second dialysis (b).

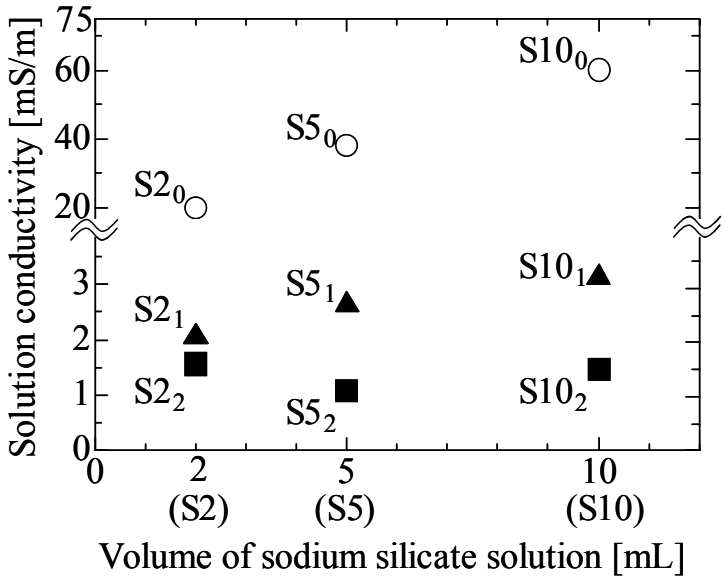

Fig. 5.4. Solution conductivity converted to the value at 25 °C before and after dialysis. ○: Before dialysis, ▲: after first dialysis, and ■: after second dialysis.

–Chapter 6– Shape-sensitive Reflectance by Nano-structured Metal Attached on an Optical Waveguide-mode Sensor

Abstract

Optical reflectance of a waveguide-mode sensor was measured as a function of light incident angle, in the case that either a Au film or nanoparticles converted from the film by thermal treatment were attached to the sensor. It is found that a dip in the spectrum, caused by waveguide-mode excitation, moves toward a lower angle in the case of the Au-film attachment, while it shifts toward a higher angle in the case of the attachment of an ensemble of nanoparticles. This difference in shift can be explained by theoretical calculations using average refractive indices of the Au-containing layer. Therefore, whether a Au nanostructure is film-like or spherical can be speculated by the spectra.

6.1 Introduction

Metal nanostructures such as thin films and nanoparticles (NPs) have attracted much attention because surface plasmon resonance can localize the energy of light into a region that is much smaller than that allowed by the diffraction limit [1–3]. As a matter of course, the plasmonic properties induced in them are influenced by their shapes [4]. Therefore, it is quite important that their shapes be recognized accurately. Among various methods for observing metal nanostructures, two methods, namely, SEM and TEM, are widely used. However, these methods are destructive and require a long time and technical mastery for sample preparation. Further, although the diameters of metal NPs can be estimated nondestructively using small-angle x-ray or neutron scattering [5,6], these methods need radioactive x-rays and neutrons. In the present research, optical reflectance of nano-structured metal attached on a waveguide-mode sensor was measured as a function of light incident angle. As a result, the shift of a dip in the spectrum was found to depend on metal shapes. This shape-sensitive reflectance of metal on a waveguide-mode sensor can be in principle used as a new nondestructive method for estimating the shapes of metal nanostructures.

6.2 Experimental Procedures

Figure 6.1 shows a schematic of the optical system used in the present experiment, which consists of a He-Ne laser, a polarizer, a waveguide-mode sensor, and a photodiode. The waveguide-mode sensor is composed of a prism and a transparent substrate with two layers of different refractive indices; the sensor and the substrate were assembled in the Kretschmann configuration on a goniometer. The substrate was prepared by oxidizing a silicon-on-quartz (SOQ) substrate (from Shin-Etsu Chemical Co. Ltd.) consisting of a 265-nm-thick Si single-crystal layer and a 1.2-mm-thick SiO_2 glass layer; the oxidization was carried out in an O_2/H_2O mixture vapor at 1000 °C for 62 min. The unoxidized Si single-crystal layer and the newly formed SiO_2 glass were used as the

above-mentioned two layers. The prism is SiO_2 glass in the shape of an isosceles triangle with a vertex angle of 30°. It was attached to the SiO_2 glass of the SOQ substrate on the side opposite to the Si and newly formed SiO_2 glass layers so as to form the Kretschmann configuration. Then, the prism was illuminated with S-polarized He-Ne laser light (λ = 632.8 nm) at various incident angles in air at room temperature, and the reflected light was detected by the photodiode.

As shown in Fig. 6.1, the incident angle θ was defined as the angle between the direction of the incident light beam before its incidence on the prism and the line perpendicular to the substrate surface. The incident light propagates in the Si and SiO_2 glass layers with repeated reflections, and finally returns to the prism side. Although waveguide-mode excitation is induced in these layers at a certain incident angle, the propagating light is partly absorbed by the Si layer due to its extinction coefficient. As a result, the reflectance decreases at the incident angle corresponding to waveguide-mode excitation, forming a dip in the reflection spectrum. If a substance is attached to the surface of the SiO_2 glass layer, the dip angle should depend on the complex refractive index of the substance. Further, if the refractive index changes depending on the substance shape, it should be possible to estimate the substance shape by measuring the dip angle.

Gold (Au) was chosen as a representative metal, and reflection spectra were measured in two cases: Au on the SiO_2-glass layer surface is either of a film-like shape or an ensemble of NPs. A Au film was obtained by vacuum evaporation, while Au NPs were fabricated by thermal treatment of the evaporated film, carried out in N_2 at 800 °C for 30 min. The thickness of the Au film was measured using a quartz crystal microbalance, while the Au NPs were observed using SEM (Hitachi High-Technologies S-4800). Here, if the medium surrounding the surface of the SiO_2 glass layer is water, the measured angle can be adjusted by comparing the critical angle of total reflection appearing in the reflection spectrum with the theoretical critical angle at θ = ~62.1°. On the other hand, the critical angle is out of the measurement range if the surrounding medium is air, which means that an angle error of ±0.1° is inevitable.

6.3 Results and Discussion

First, the thicknesses of the Si single-crystal layer and SiO_2 glass layer were estimated from the substrate's reflection spectrum measured with the surface of the SiO_2 glass layer surrounded by water and covered with neither a Au film nor NPs. Open circles in Fig. 6.2 show the reflectance of the substrate as a function of the incident angle. A dip, caused by the waveguide-mode excitation, is observed at θ = ~70.7°. Then, the reflection spectrum was calculated as a function of the thicknesses of the Si and SiO_2 glass layers by the transfer matrix method [7,8] using the complex refractive index of each layer summarized in Table 6.1 [8,9]. The solid curve in Fig. 6.2 is the theoretical spectrum calculated by assuming that the thicknesses of the Si and SiO_2 glass layers are 33 and 523 nm, respectively, which agrees well with the experimental spectrum (shown by open circles). This

indicates that the thickness of the original 265-nm-thick Si layer decreased to 33 nm and that the remaining 232 nm of Si was oxidized. Further, the fact that the thickness increases by 2.25 times from 232 nm to 523 nm by oxidation to SiO_2 is consistent with the previous result reported for an SOQ substrate treated under similar oxidation conditions [8]. Therefore, for further calculations, the thickness is assumed to be 33 nm for the remaining Si and 523 nm for the newly formed SiO_2 glass.

Next, Au was evaporated on the surface of the SiO_2 glass layer to a thickness of 4.0 nm, and then it was treated at 800 °C in N_2 for 30 min in order to convert the Au film to NPs. Figure 6.3 compares the SEM images of the surface taken after the evaporation of Au (a) and after the subsequent thermal treatment (b). It is clearly observed that the Au layer changes from being film-like to an ensemble of NPs. The diameters and the number density of NPs are measured to be 22.6 ± 4.8 nm and about 1000 μm^{-2}, respectively, from Fig. 6.3(b). However, the real diameters are assumed to be smaller than those measured because a conductive Pt film with a thickness of a few nm was coated on the substrate surface for the SEM observation. By assuming that the entire Au layer with a thickness of 4.0 nm transformed into an ensemble of Au NPs with the number density of 1000 μm^{-2}, the diameter of NPs can be calculated to be 19.7 nm. The difference between this diameter and the one estimated directly from Fig. 6.3(b) is ~3 nm, which is similar to the thickness of the Pt film. Thus, the average diameter of 19.7 nm will be used in further analysis.

Next, the author measured the reflection spectrum of a similar substrate with a SiO_2 glass surface surrounded by air. Here, it should be noted that water cannot be used as a surrounding medium for a SiO_2 glass layer on which a Au layer has been deposited; this is because the Au layer is easily peeled off in water. Figure 6.4(a) shows the reflection spectra obtained experimentally before (i) and after the deposition of a Au film having a thickness of 4.0 nm on the SiO_2-glass layer surface by vacuum evaporation (ii), and after the conversion of the Au film to NPs by the thermal treatment (iii). Here, as mentioned above, it was impossible to eliminate the angle error, ±0.1° at its maximum, since the medium surrounding the surface of the SiO_2 glass layer was air. Before the Au deposition, the incident angle of the dip, referred to as θ_d, is $\theta_d = 66.45°$. This implies that θ_d is 4.3° smaller than the dip angle shown in Fig. 6.2. This is because the refractive index of the medium surrounding the surface of the SiO_2 glass layer decreased from 1.332 (water) to 1.000 (air). Change in θ_d induced by the Au deposition, referred to as $\Delta\theta_d$, is $\Delta\theta_d = -2.43°$ before the thermal treatment as shown by spectrum (ii), while $\Delta\theta_d$ is +1.48° after the film was converted to NPs by the thermal treatment, as shown by spectrum (iii). Namely, the dip shifts toward opposite angles depending on whether the deposited Au is in the form of a film or NPs. It is also observed that the dip shape shown by spectrum (ii) is broad, while the one shown by spectrum (iii) is deep, compared to the one shown by spectrum (i).

The average complex refractive index of the Au layer should vary when the Au film is converted to NPs, due to the presence of air between NPs. This should be the reason of the above-mentioned

difference in θ_d. In order to confirm this hypothesis, the average complex refractive index (n) of a layer consisting of a homogenous mixture of Au NPs and air, hereafter referred to as the "Au/air layer", is estimated by Eq. (6.1) using the Lorentz-Lorenz effective medium expression [10],

$$\frac{n^2-1}{n^2+2} = f_{Au}\frac{{n_{Au}}^2-1}{{n_{Au}}^2+2} + (1-f_{Au})\frac{{n_a}^2-1}{{n_a}^2+2}, \tag{6.1}$$

where n_{Au} and f_{Au} are the complex refractive index and volume fraction of the Au NPs, respectively, while n_a is the complex refractive index of air. If n_a can be assumed to be unity, Eq. (6.1) can be written as

$$\frac{n^2-1}{n^2+2} = f_{Au}\frac{{n_{Au}}^2-1}{{n_{Au}}^2+2}. \tag{6.2}$$

From the Drude equation, taking account of the influence of the particle diameter [11], n_{Au} becomes 0.360 + 3.09i. Furthermore, it is assumed that the entire 4.0-nm-thick deposited Au layer was converted to the Au/air layer with a thickness equal to the average diameter of Au NPs, 19.7 nm. Then, f_{Au} becomes 4.0/19.7. By using these values, the complex refractive index of the Au/air layer was calculated to be n = 1.47 + 0.0441i, which is significantly different from that of film-like Au, 0.197 + 3.098i [12]. This difference in the complex refractive indices of film-like Au and the Au/air layer seems to be the reason for the significant difference in θ_d between spectra (ii) and (iii) shown in Fig. 6.4(a). Thus, whether film-like Au or Au NPs can be speculated easily by paying attention to this difference.

In order to verify the above assumption, reflection spectra were calculated by the transfer matrix method for the configurations and their parameters listed in Table 6.2. Figure 6.4(b) shows the calculated spectra before (i) and after the deposition of Au with a thickness of 4.0 nm on the surface of the SiO_2 glass layer (ii), and after the conversion of the deposited Au to NPs by the thermal treatment (iii). Spectrum (ii) shows that $\Delta\theta_d$ induced by the Au deposition is –1.43°. The fact that $\Delta\theta_d$ is negative or the dip shifts toward a lower angle is consistent with the experimental result shown by spectrum (ii) in Fig. 6.4(a). However, the dip shape does not agree with the experimental result. The fact that the actual deposited surface is not completely flat, as shown in Fig. 6.3(a), could be a possible cause. On the other hand, spectrum (iii) indicates that $\Delta\theta_d$ is +1.03°, when the deposited Au transforms into NPs, which agrees fairly well with the experimental result shown by spectrum (iii) in Fig. 6.4(a). It is also found that the dip shape is also in agreement with the experimental result.

Further verification was carried out. First, Au was deposited to a thickness of 2.0 nm and it was then annealed at 800 °C in N_2 for 30 min in order to obtain Au NPs. Open squares in Fig. 6.5 show the reflection spectrum of the substrate with NPs, while open circles represent the spectrum obtained

before the Au deposition, shown by the curve (i) in Fig. 6.4(a). From these spectra, $\Delta\theta_d$ is found to be +0.67°. The inset shows an SEM image of the surface after the formation of NPs, which reveals that the average diameter and number density of NPs are about 11.4 nm and 2570 μm^{-2}, respectively. From these values, the average complex refractive index was estimated to be 1.39 + 0.0463i. The solid curve in Fig. 6.5 shows the theoretical spectrum calculated using these estimated values; it is clearly observed that the shape as well as θ_d in the experimental spectrum agrees quite well with the theoretical result.

Here, in order to recognize easily that θ_d depends on whether the deposited Au is in the form of a film or NPs, Fig. 6.6 shows θ_d as a function of evaporation thickness of Au. The open circle represents θ_d obtained before the Au deposition, while solid squares and triangles represent θ_d obtained for substrates with and without the thermal treatment of Au deposited, respectively. As mentioned above, the Au shape is film-like before the thermal treatment, while it is NP-like after the treatment. Thus, θ_d shifts toward opposite angles depending on the shape of Au attached to the substrate: whether the Au is film-like or in the form of an ensemble of NPs. This fact indicates that the present waveguide-mode sensor can be in principle used for the shape estimation of metal nanostructures.

Furthermore, the spectral shape can be calculated theoretically if the Au attached is in the form of an ensemble of NPs. The variables here are the average diameter and number density of NPs. Therefore, if the volume, or the product of the diameter and number, of the Au deposited can be measured by an instrument such as a quartz crystal microbalance, the diameter and number can be estimated as the values that can reproduce the spectrum obtained experimentally. Furthermore, if the diameter of Au NPs is known, as in the cases of colloidal Au NPs used widely as labels for biomolecular detection, the number of NPs attached can be estimated. Thus, by using the waveguide-mode sensor, the average diameter and number of NPs can also be estimated.

In the present optical system, only the reflectance of light is measured. Therefore, it is nondestructive, and no radioactive rays are used. There have been several papers reporting similar shape-sensitive optical measurement results on nano-structured metal [13,14]. For example, Kalyuzhny *et al*. compared absorption spectra of a transparent substrate on which an island-like Au film or an ensemble of Au NPs had been deposited [13]. However, the measurement of absorption spectra cannot avoid inevitable influences of reflection and scattering. In this regard, the measurement of reflection, in which the incident and reflection angles can be determined precisely, is much superior. Furthermore, since the present optical system is not complex, *in-situ* observation during the formation of nanostructures can be performed by installing the system in the fabrication chamber. Moreover, the system can be used even when the substrate surface is covered with liquid, because the light is incident on the prism that is set on the opposite side of the metal-attached layer. Thus, the system is attractive because of these features that cannot be satisfied by any other methods.

6.4 Conclusions

It has been demonstrated clearly that the dip angle in the spectrum of the light reflected from a waveguide-mode sensor depends on the shape of Au included in a layer attached on the backside of the sensor: whether Au is in the form of a film or in the form of an ensemble of nanoparticles. This is because of the fact that the average refractive index of the Au-included layer is quite different between the two forms. Furthermore, in the case of Au nanoparticles, the spectrum obtained experimentally agrees fairly well with that obtained theoretically by taking account of the average complex refractive index, which can be calculated using the average diameter and number density of nanoparticles. Thus, the waveguide-mode sensor can be utilized for shape estimation of Au nanostructures. Moreover, if either the diameter or number density of nanoparticles is known or if the relation between the two is given, they can be estimated fairly accurately.

References for Chapter 6

[1] T. W. Ebbesen, H. J. Lezec, H. F. Ghaemi, T. Thio, and P. A. Wolff, Nature **391**, 667 (1998).

[2] S. A. Maier, P. G. Kik, H. A. Atwater, S. Meltzer, E. Harel, B. E. Koel, and A. A. G. Requicha, Nat. Mater. **2**, 229 (2003).

[3] S. Kawata, Y. Inouye, and P. Verma, Nat. Photonics **3**, 388 (2009).

[4] S. Link and M. A. El-Sayed, J. Phys. Chem. B **103**, 8410 (1999).

[5] J. R. Levine, J. B. Cohen, and Y. W. Chung, Surf. Sci. **248**, 215 (1991).

[6] T. Thomson, S. L. Lee, M. F. Toney, C. D. Dewhurst, F. Y. Ogrin, C. J. Oates, and S. Sun, Phys. Rev. B **72**, 064441 (2005).

[7] K. Awazu, C. Rockstuhl, M. Fujimaki, N. Fukuda, J. Tominaga, T. Komatsubara, T. Ikeda, and Y. Ohki, Opt. Express **15**, 2592 (2007).

[8] M. Fujimaki, C. Rockstuhl, X. Wang, K. Awazu, J. Tominaga, Y. Koganezawa, Y. Ohki, and T. Komatsubara, Opt. Express **16**, 6408 (2008).

[9] *Handbook of Optical Constants of Solids II*, edited by E. D. Palik (Academic Press, San Diego, CA, 1991).

[10] D. E. Aspnes, Thin Solid Films **89**, 249 (1982).

[11] *Near-Field Optics and Surface Plasmon Polaritons*, edited by S. Kawata (Springer, Berlin, 2001).

[12] M. Fujimaki, C. Rockstuhl, X. Wang, K. Awazu, J. Tominaga, N. Fukuda, Y. Koganezawa, and Y. Ohki, Nanotechnology **19**, 095503 (2008).

[13] G. Kalyuzhny, A. Vaskevich, G. Ashkenasy, A. Shanzer, and I. Rubinstein, J. Phys. Chem. B **104**, 8238 (2000).

[14] M. Kawasaki and M. Hori, J. Phys. Chem. B **107**, 6760 (2003).

Table 6.1. Materials used in individual layers of the sample. Complex refractive indices employed to obtain the theoretical spectrum shown in Fig. 6.2 are also listed.

Layer	Complex refractive index
SiO_2 glass prism and SiO_2 glass substrate	1.456
Si single-crystal layer	3.882+0.019i
SiO_2 glass layer	1.456
Water	1.332

Table 6.2. Materials used in individual layers of the sample and their thicknesses. Complex refractive indices employed to obtain the theoretical spectra shown in Fig. 6.4(b) are also listed.

Layer	Complex refractive index	Thickness [nm]
SiO_2 glass prism and SiO_2 glass substrate	1.456	–
Si single-crystal layer	3.882+0.019i	33
SiO_2 glass layer	1.456	523
Au-attached layer		
Au film (Spectrum (ii) in Fig. 6.4(b))	0.197+3.098i	4.0
Au NPs (Spectrum (iii) in Fig. 6.4(b))	1.47+0.0441i	19.7
Air	1.000	–

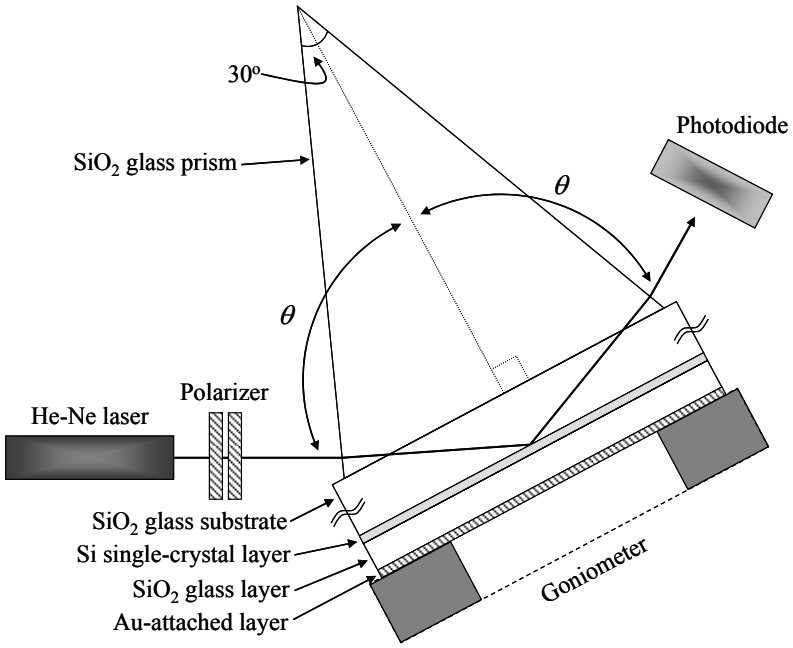

Fig. 6.1. Schematic showing the optical reflectance measurement system.

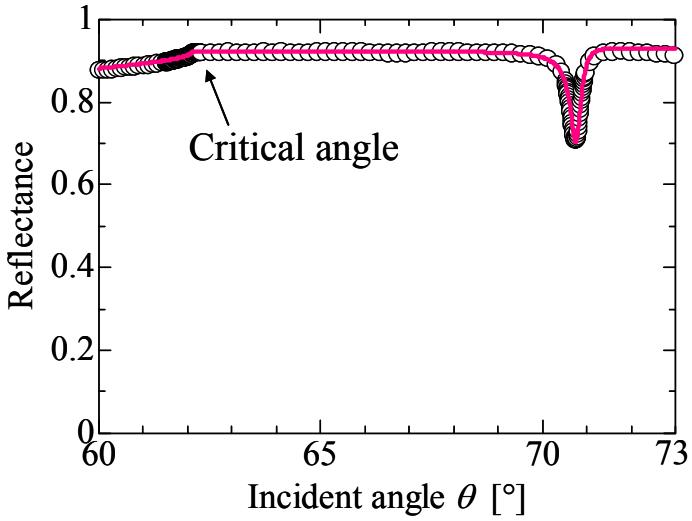

Fig. 6.2. Optical reflectance of the substrate as a function of the incident angle, observed with the surface of the SiO_2 glass layer surrounded by water and covered with neither a Au film nor NPs (open circles). The solid curve shows the theoretical spectrum calculated by assuming that the Si and SiO_2 glass layers are 33 and 523 nm thick, respectively.

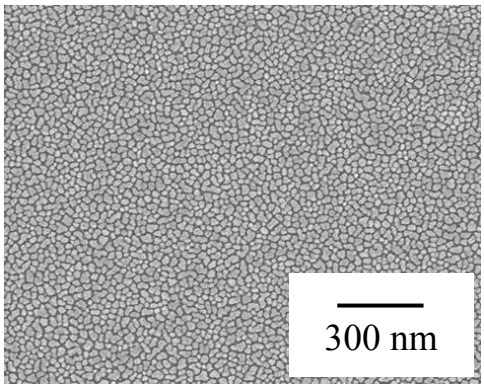

(a)

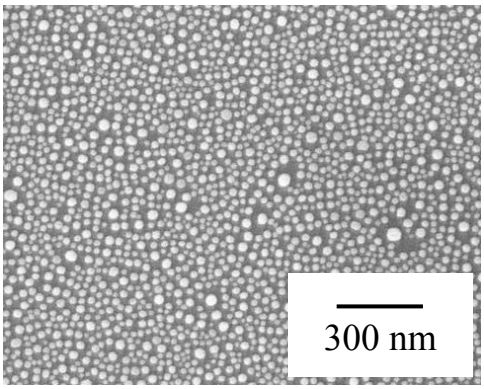

(b)

Fig. 6.3. Scanning electron microscopy images of the surface of the SiO_2 glass layer, taken after evaporating Au to a thickness of 4.0 nm on the surface (a) and after the subsequent thermal treatment at 800 °C in N_2 for 30 min (b).

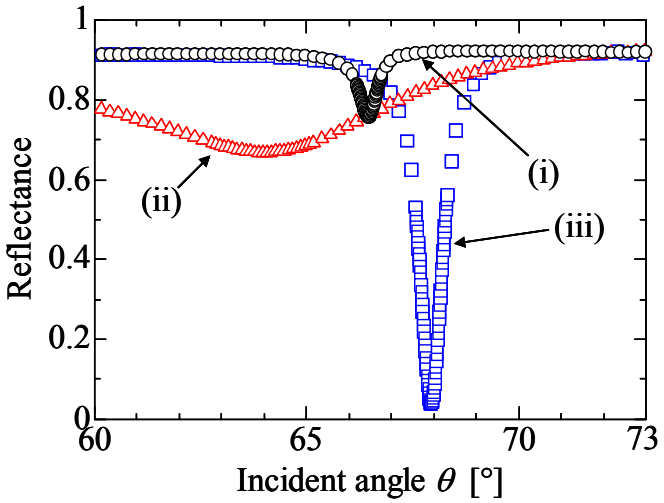

(a)

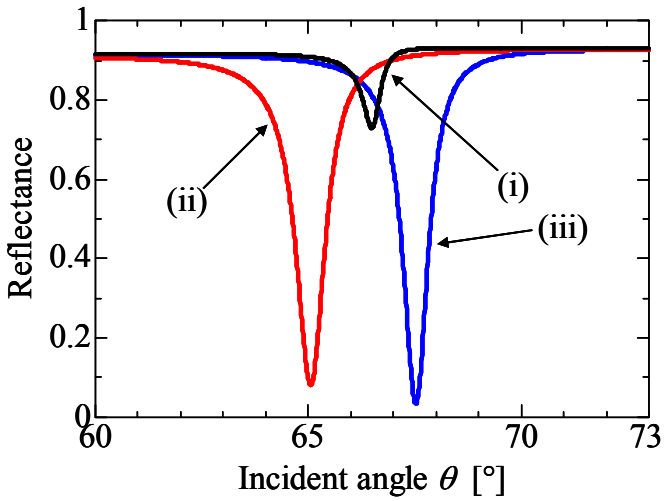

(b)

Fig. 6.4. Experimental (a) and theoretical (b) reflection spectra of the substrate in the case that the surrounding medium was air. Curves (i) to (iii) represent the spectra obtained before (i) and after the deposition of the 4.0-nm-thick Au film on the SiO_2 glass surface (ii), and after the conversion of the deposited film to NPs by the thermal treatment (iii).

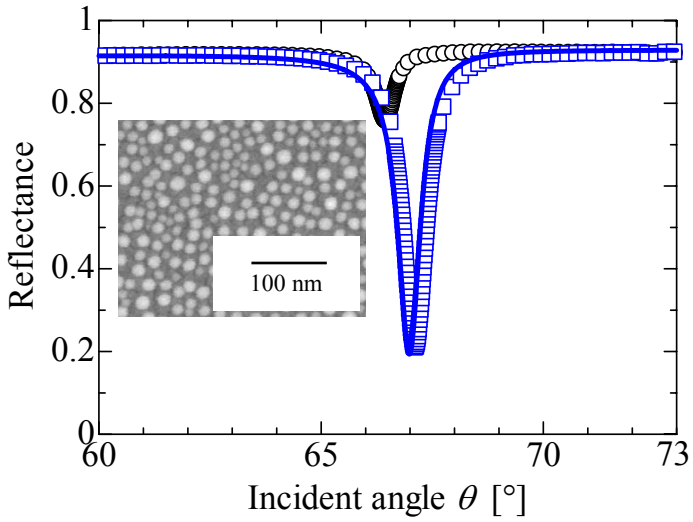

Fig. 6.5. Reflection spectrum of the substrate after the 2.0-nm-thick Au film was converted to NPs by the thermal treatment (open squares). The spectrum before the Au deposition, shown by the curve (i) in Fig. 6.4(a), is also shown as open circles. The solid curve is the theoretical spectrum after the formation of Au NPs, while the inset shows an SEM image of the SiO_2 glass surface on which the NPs were formed.

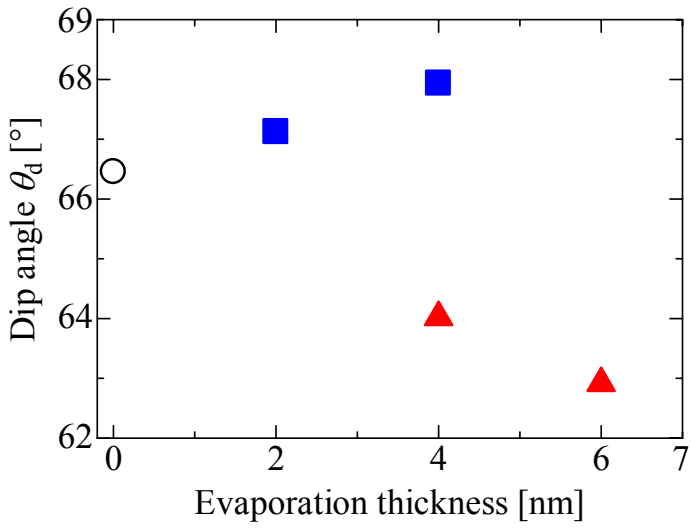

Fig. 6.6. The dip angle θ_d as a function of evaporation thickness of Au. The open circle represents θ_d obtained before the Au deposition, while solid squares and triangles represent θ_d obtained for substrates with and without the thermal treatment of Au deposited, respectively.

–Chapter 7– Summary

To conclude this doctoral thesis, important knowledge obtained in each session is summarized as follows. Future prospects of the near-field optics are also described.

Chapter 2

Structural changes induced in rutile TiO_2 single crystals by swift-heavy-ion irradiation have been investigated, and its applications to three-dimensional lithography have been described. From XRD and TEM analyses, it was found that the crystallinity became worse in the ion-irradiated region. Namely, the ion-irradiated region became amorphous and the surrounding region was distorted. It also became clear that this amorphous region, or a latent track, as well as its surrounding could be etched by hydrofluoric acid, while the nonirradiated region could not be etched. In the case of the irradiation of Ti, Cu, Br, and I ions, etching stopped at the depth where the electronic stopping power decayed to 6.2 keV/nm irrespective of the ion species and acceleration energy. However, in the case of the irradiation of Cl ions with energies higher than ~77 MeV or that of Ca ions with energies higher than ~72 MeV, the top surface remained unchanged, keeping the rutile structure, and could not be etched even if the electronic stopping power exceeded 6.2 keV/nm, while a vacant hollow was created by being etched inside the TiO_2. Calculation of the radial distribution of energy deposited on the surface by one ion, in which the ion velocity is taken into account, clearly shows that this energy distribution is the critical factor to determine whether the surface can be etched or not. Furthermore, lithography to the TiO_2 surface has been demonstrated successfully using this etching technique. It was found that the bottom surfaces and sidewalls fabricated by this method were smooth in the order of nm. These facts show that a combination of the swift-heavy-ion irradiation and etching of the ion-induced latent track is novel as micro- and nano-fabrication methods of two- and three-dimensional structures into insulators.

Chapter 3

A new plasmonic structure with a three-dimensional distribution of Au nanoparticles (NPs) in nanopores, perforated by the etching of swift-heavy-ion-induced latent tracks with hydrofluoric acid vapor, on the surface of a SiO_2 glass has been developed. First, for various ion irradiation conditions, the radius of the ion-induced melted region calculated based on the thermal spike model was compared to the average radius of nanopores perforated by immersing in hydrofluoric acid. As a result, there was a strong correlation between the melted radius and the nanopore radius. Therefore, it is confirmed that the radius of a nanopore or latent track is determined by the melted region. Next, latent tracks were formed on SiO_2 glass using 137-MeV Au ions, by which the largest pores should be obtained according to the calculation of the melted region. Then each track was etched by

hydrofluoric acid vapor, resulting in the formation of nanopores with an average diameter of ~50 nm. Furthermore, Au NPs were embedded into the nanopores using vacuum evaporation and thermal treatment. In the structure fabricated, the redshift in the localized surface plasmon (LSP) excitation wavelength of the Au NPs was seen when water, introduced into the nanopores, surrounded the NPs. This is consistent with the theoretical result estimated from the Drude equation. Thus, it is confirmed that the fabricated structure can be applied to a sensing element such as a biomolecular sensor to detect the change in refractive index around the Au NPs.

Chapter 4

In preceding chapters, it was demonstrated that LSP resonance in the near-ultraviolet region occurring in Ag NPs with a thin SiO_2-glass film can be utilized to various applications such as photocatalysts. In this chapter, the SiO_2-glass-coated Ag NPs were fabricated using a chemical synthesis in a solution, and their optical properties were investigated. From a TEM image, it became clear that extremely small plasmonic structures of Ag NPs with an average diameter of 7 nm coated with SiO_2 glass with an average thickness of 3 nm could be fabricated by this method. Furthermore, it was found that the LPS excitation wavelength of the Ag NPs shifted from 395 to 400 nm due to the coating of SiO_2 glass, which is so small that the degradation of the electric field enhancement in the near-ultraviolet region can be neglected. Furthermore, numerical simulation shows that the significant electric field enhancement by a factor of 1.8 can be obtained by the fabricated structures. Thus, it is concluded that higher performance of various optical devices used in the near-ultraviolet region can be realized using the synthesized SiO_2-glass-coated Ag NPs.

Chapter 5

In this chapter, first, the appropriate amount of 3-aminopropyltrimethoxysilane (APS) as a silane coupling agent used to couple Ag and SiO_2 glass was investigated. Through absorption measurement and numerical calculation on the area of APS attached onto Ag-NP surfaces, it was found that aggregation of Ag NPs occurred when the amount of APS exceeded the amount necessary to form the monolayer coating around the NPs. This result is consistent with the one obtained by a similar experiment on Au NPs. From these results, the appropriate amount of APS to yield Ag NPs with no aggregation was estimated successfully. Next, conditions necessary to prevent the aggregation of Ag NPs during the coating of SiO_2 glass were investigated by changing the amount of sodium silicate as well as the number of dialysis. As a result, it was found that the decrease in solution conductivity accelerated the aggregation, resulting in deterioration of the plasmonic activity of Ag NPs. This in turn indicates that the aggregation of Ag should be caused by decay of electrostatic repulsion between the NPs due to the decrease in the number of ions surrounding the NPs. Thus, it is revealed that the solution conductivity is a key factor for the synthesis of SiO_2-glass-coated Ag NPs with no

aggregation.

Chapter 6

A significant difference was found in the dip angle occurring in an optical reflection spectrum of a waveguide-mode sensor depending on the shape of nano-structured metal, and this was investigated in Chapter 6. Optical reflectance in the waveguide-mode sensor as a function of light incident angle was measured in two cases that either a continuous Au film or an ensemble of Au NPs were attached to the sensor. It was found that the dip shifts toward opposite angles depending on whether the deposited Au is in the form of a film or NPs, even if the amount of the deposited Au was the same. In order to investigate the reason why such difference in dip angle occurred, theoretical calculations using the transfer matrix method were carried out. For the case of the Au-NP attachment, the Lorentz-Lorenz effective medium expression was used. As a result, it was revealed that the difference occurred due to the fact that the average complex refractive index of the Au-containing layer significantly differed from each other. In addition, especially in the case of Au NPs, it was also clearly shown that the shape of the experimental spectrum agreed fairly well with that of the theoretical spectrum. Thus, it is confirmed that whether Au is in the form of a film or of an ensemble of NPs can be distinguished nondestructively using the waveguide-mode sensor. This in turn indicates that the sensing system is a possible method for shape estimation of nano-structured metal.

Future prospects in the near-field optics

As mentioned in each chapter, optical near-field is a new light occurring in a region much smaller than the diffraction limit. This special light has a significantly wide range of applications such as a highly sensitive biomolecular sensor, a high-performance photocatalyst and a solar cell, enhancement of Raman scattering, a plasmonic waveguide, and so on. Since such various outstanding optical devices can be realized, importance of optical near-field is increasing day by day. Although most of these applications utilizing optical near-field are presently in the phase of “research and development”, they must come into the phase of “practical use” in the near future.

As mentioned above, optical near-field is quite a small light, however, it has a large potential. I am sure that research on near-field optics makes further progress, and this special light will illuminate and brighten our future.

Acknowledgments

First, I would like to express my heartfelt gratitude to my supervisor, Prof. Yoshimichi Ohki, for advice, guidance, and encouragement throughout the course of this work. I am also grateful to Drs. Makoto Fujimaki and Koichi Awazu of the National Institute of Advanced Industrial Science and Technology (AIST), who introduced me to research on nanofabrication and near-field optics, for their advice and discussions as well as the use of experimental apparatus. I am also grateful to Profs. Yoshiji Horikoshi, Takayuki Sota, Masakazu Washio of Waseda University for their valuable advice and comments on this doctoral thesis.

Appreciation is due Dr. Tetsuro Komatsubara of the University of Tsukuba for the use of the ion accelerator. I acknowledge Dr. Nobuko Fukuda, Mr. Xiaomin Wang, Dr. Subash Chandra Bose Gopinath, Dr. Tsutomu Hirakawa, Dr. Paul Fons, and Dr. Junji Tominaga of AIST for their valuable advice and discussion. I appreciate help from Dr. Carsten Rockstuhl of Friedrich Schiller Universität Jena for advice and comments on numerical calculations. I would like to acknowledge Prof. Toshiya Watanabe and Dr. Naoya Yoshida of the University of Tokyo for their advice and comments. I would also like to express my sincere thanks to Dr. Jean-François Masson of the Université de Montréal for insightful advice and discussions regarding this research.

Appreciation is also extended to Mr. Tomoyuki Suzuki, Mr. Naoki Kato, and Mr. Hiroaki Ohki of Sony Corporation for their encouragement.

I would like to acknowledge the students of Prof. Ohki's laboratory who worked with me; Tetsuya Nakanishi, Yoshihiro Nagasawa, Shinji Fujii, Atsushi Maeda, Takafumi Kato, Kazuki Sato, Akito Izaki, and Akihiro Yoshida, for their assistance in experiments, and many other students for fruitful time in the laboratory.

Finally, I would like to express my heartfelt gratitude to my parents and friends for their encouragement and support.

List of Papers Published by the Author
研究業績

【論文】
原著論文

○1) K. Nomura, Y. Ohki, M. Fujimaki, X. Wang, K. Awazu, and T. Komatsubara, “Plasmonic activity on gold nanoparticles embedded in nanopores formed in a surface layer of silica glass by swift-heavy-ion irradiation”, Nanotechnology, Vol. 20, No. 47, pp. 475306-1-475306-7 (2009 年 10 月).

○2) K. Nomura, S. Fujii, Y. Ohki, K. Awazu, M. Fujimaki, N. Fukuda, and T. Hirakawa, “Solution Conductivity as a Key Factor for Thin Silica Coating on Colloidal Silver”, Japanese Journal of Applied Physics, Vol. 48, No. 6, pp. 06FE04-1-06FE04-4 (2009 年 6 月).

○3) K. Nomura, S. Fujii, Y. Ohki, K. Awazu, M. Fujimaki, J. Tominaga, N. Fukuda, T. Hirakawa, and C. Rockstuhl, “Fabrication of Inert Silver Nanoparticles with a Thin Silica Coating”, Japanese Journal of Applied Physics, Vol. 47, No. 11, pp. 8641-8643 (2008 年 11 月).

○4) K. Nomura, T. Nakanishi, Y. Nagasawa, Y. Ohki, K. Awazu, M. Fujimaki, N. Kobayashi, S. Ishii, and K. Shima, “Structural change induced in TiO_2 by swift heavy ions and its application to three-dimensional lithography”, Physical Review B, Vol. 68, Issue 6, pp. 064106-1-064106-8 (2003 年 8 月).

【講演】
国際会議

1) K. Nomura, K. Sato, Y. Ohki, M. Fujimaki, and K. Awazu, “Shape Estimation of Au Nanostructures using Optical Near-Fields Induced in Waveguide-Mode Sensors”, FACSS conference 2009, Louisville, KY, USA (2009 年 10 月), The Federation of Analytical Chemistry and Spectroscopy Societies, p. 192.

2) K. Nomura, S. Fujii, Y. Ohki, K. Awazu, M. Fujimaki, J. Tominaga, N. Fukuda, and T. Hirakawa, “Solution conductivity as a key factor for thin silica coating on colloidal Ag”, The 21st International Microprocesses and Nanotechnology Conference, Fukuoka, Japan (2008 年 10 月), The Japan Society of Applied Physics, pp. 238-239.

国内発表

1) 野村健一、佐藤一樹、大木義路、藤巻真、粟津浩一、「近接場光による微細金属構造の形状判別」、第 70 回応用物理学会学術講演会、講演予稿集 No. 3、p. 915 (2009 年 9 月).

2) 佐藤一樹、野村健一、大木義路、藤巻真、粟津浩一、「Au ナノ粒子吸着時の導波モー

ドセンサの光反射特性」、第 70 回応用物理学会学術講演会、講演予稿集 No. 3、p. 938 (2009 年 9 月).

3) 加藤貴史、野村健一、大木義路、藤巻真、粟津浩一、「導波モードセンサによる Au ナノ粒子標識化生体分子の高感度検出」、第 70 回応用物理学会学術講演会、講演予稿集 No. 3、p. 938 (2009 年 9 月).
4) 藤巻真、スバス C. B.ゴピナス、王暁民、粟津浩一、野村健一、佐藤一樹、加藤貴史、大木義路、「導波モードを用いた着色分子の高感度検出」、第 70 回応用物理学会学術講演会、講演予稿集 No. 3、p. 1249 (2009 年 9 月).
5) 野村健一、佐藤一樹、大木義路、藤巻真、粟津浩一、「導波モードセンサによる金属ナノ構造の光学的非破壊形状計測」、ナノオプティクス研究グループ 第 18 回研究討論会、予稿集 pp. 30-35 (2009 年 7 月).
6) 野村健一、大木義路、粟津浩一、藤巻真、富永淳二、小松原哲郎、「高速重イオン照射によるルチル単結晶の構造変化及びそのナノ加工への応用」、放電学会 2008 年年次大会、講演論文集 pp. 67-68 (2008 年 11 月).
7) 野村健一、大木義路、藤巻真、粟津浩一、富永淳二、小松原哲郎、「シリカガラス中の潜トラックエッチングによるナノ細孔への Au ナノ粒子の充填」、第 69 回応用物理学会学術講演会、講演予稿集 No. 3、p. 896 (2008 年 9 月).
8) 野村健一、藤井晋司、大木義路、粟津浩一、福田伸子、平川力、藤巻真、富永淳二、「薄膜シリカでコートされた銀ナノ粒子の作製」、第 55 回応用物理学関係連合講演会、講演予稿集 No. 3、p. 1276 (2008 年 3 月).
9) 野村健一、長澤理裕、大木義路、粟津浩一、藤巻真、小林直人、石井聡、島邦博、「高速重イオンビームによるルチル型 TiO_2 単結晶表面エッチングの横方向閾値エネルギー」、第 50 回応用物理学関係連合講演会、講演予稿集 No. 2、p. 781 (2003 年 3 月).
10) 粟津浩一、藤巻真、野村健一、中西哲也、大木義路、石井聡、島邦博、「重イオンビームを用いたセラミックスの三次元ナノ精度加工」、第 50 回応用物理学関係連合講演会、講演予稿集 No. 0、p. 113 (2003 年 3 月).
11) 野村健一、長澤理裕、中西哲也、服部雅晴、崔明秀、大木義路、粟津浩一、藤巻真、小林直人、石井聡、島邦博、「高速重イオンビーム照射およびエッチングによるルチル型 TiO_2 単結晶表面および内部への微細構造の作製」、第 63 回応用物理学会学術講演会、講演予稿集 No. 2、p. 642 (2002 年 9 月).
12) 野村健一、中西哲也、服部雅晴、崔明秀、大木義路、粟津浩一、小林直人、藤巻真、島邦博、石井聡、「高速重イオンビーム照射によるルチル型 TiO_2 単結晶の構造変化」、第 49 回応用物理学関係連合講演会、講演予稿集 No. 3、p. 1025 (2002 年 3 月).

【著書】

1) K. Awazu, K. Nomura, M. Fujimaki, and Y. Ohki, “3D Nanofabrication of Rutile TiO_2 Single

Crystals with Swift Heavy-Ions", The Nano-Micro Interface, pp. 207-223, (Wiley-VCH, Weinheim, 2005 年 1 月).

【その他】

特許

1) 藤巻真、野村健一、「検体検出センサー及び検体検出方法」、出願日: 2009 年 1 月 30 日、出願番号: 特願 2009-019296 (出願中).
2) 大木義路、中西哲也、野村健一、島邦博、石井聡、粟津浩一、藤巻真、「結晶 TiO_2 の微細加工方法及び微細加工された結晶 TiO_2 (Method of Microfabricating Crystal TiO_2 and Microfabricated Crystal TiO_2)」、出願日: 2003 年 3 月 24 日、出願番号: PCT/JP03/003499、公開日: 2003 年 10 月 2 日、国際公開番号: WO/03/080902 A1 ※内容は下記[3]と同じ.
3) 大木義路、中西哲也、野村健一、島邦博、石井聡、粟津浩一、藤巻真、「結晶 TiO_2 の微細加工方法及び微細加工された結晶 TiO_2」、出願日: 2002 年 3 月 26 日、出願番号: 特願 2002-87052、公開日: 2003 年 10 月 2 日、公開番号: 特開 2003-279766.

大学紀要論文

1) M. Fujimaki, K. Awazu, N. Kobayashi, T. Nakanishi, K. Nomura, Y. Ohki, S. Ishii, and K. Shima, "Fabrication of microstructures in rutile TiO_2 single crystal using structural change induced by swift heavy-ion bombardment", Annual Report, Tandem Accelerator Complex, University of Tsukuba, pp. 60-61 (2002 年).

【その他、本研究に直接関係しない業績】

(原著論文)

1) T. Nakanishi, M. Fujimaki, S. Tokuhiro, K. Nomura, Y. Ohki, and K. Imamura, "Ultraviolet photon-induced absorption bands and paramagnetic centers in Ge and Sn co-doped SiO_2 glass", Journal of Non-Crystalline Solids, Vol. 318, Issues 1-2, pp. 87-94 (2003 年 4 月).

(国内発表)

1) 徳廣真一郎、中西哲也、野村健一、大木義路、藤巻真、西川宏之、今村一雄、「Ge, Sn 共添加 SiO_2 ガラスにおける常磁性欠陥のブリーチ現象」、第 61 回応用物理学会学術講演会、講演予稿集 No. 2、p. 812 (2000 年 9 月).

(特許)

1) 大木義路、藤巻真、徳廣真一郎、野村健一、今村一雄、「耐熱処理装置及び耐熱処理方法並びにグレーティング」、出願日: 2000 年 8 月 31 日、出願番号: 特願 2000-264328、公開日: 2002 年 3 月 12 日、公開番号: 特開 2002-71974